On the adhesion between fine particles and nanocontacts: an atomic force microscope study

DISSERTATION

zur Erlangung des Grades eines Doktors der Naturwissenschaften

vorgelegt von

Dipl.- phys. Mahdi Farshchi Tabrizi

aus der IR.Iran

eingereicht beim Fachbereich 8

der Universität Siegen

Siegen 2007

UNIVERSITÄT SIEGEN

1. Gutachter: Prof. Dr. H.-J. Butt

2. Gutachter: Prof. Dr. A. Mews

3. Gutachter: Prof. Dr. H.-J. Deiseroth

Datum der mündlichen Prüfung: 23. 1. 2007

To all due to whom I arrived to this point

Abstract

To optimize the handling of fine powders in industrial applications, understanding the interaction forces between single powder particles is fundamental. The forces between colloidal particles dominate the behavior of a great variety of materials, including paints, paper, soil, and many industrial processes. With the invention of the atomic force microscope (AFM), the direct measurement of the interaction between single micron-sized particles became possible. The adhesional contact between a particle and a substrate is a parameter for analyzing pull-off force data generated by AFM. The aim of this study was to understand surface interactions between fine particles. I measured the adhesion forces between AFM tips or particles attached to AFM cantilevers and different solid samples. Smooth and homogeneous surfaces such as silicon wafer, mica, or highly oriented pyrolytic graphite (HOPG), and more rough and heterogeneous surfaces such as iron particles or patterns of TiO_2 nanoparticles on silicon wafer were used. First, I addressed to the well-known issue that AFM adhesion experiment results show wide distributions of adhesion forces rather than a single value. My experimental results show that variations in adhesion forces comprise fast (i.e., from one force curves to the next) random fluctuations and slower fluctuations, which occur over tens or hundreds of consecutive measurements. Slow fluctuations are not likely to be the result of variations in external factors such as lateral position, temperature, humidity, and so forth because those were kept constant. Even if two solid bodies are brought into contact under precisely the same conditions (same place, load, direction, etc.) the result of such a measurement will often not be the same as for the previous contact. The measurement itself will induce structural changes in the contact region which can change the value for the next adhesion force measurement.

In the second part I studied the influence of humidity on the adhesion of nanocontacts. Humidity was adjusted relatively fast to minimize tip wear during one experiment. For hydrophobic surfaces, no signification change of adhesion force with humidity was observed. Adhesion force-versus-humidity

curves recorded with hydrophilic surfaces either showed a maximum or continuously increased. I demonstrate that the results can be interpreted with simple continuum theory of the meniscus force. The meniscus force is calculated based on a model that includes surface roughness and takes into account different AFM tip (or particle) shapes by a two-sphere-model. Experimental and theoretical results show that the precise contact geometry has a critical influence on the humidity dependence of the adhesion force. Changes of tip geometry on the sub-10-nm length scale can completely change adhesion force-versus-humidity curves. Our model can also explain the differences between earlier AFM studies, where different dependencies of the adhesion force on humidity were observed.

Keywords: Atomic force microscopy (AFM), cantilever, spring constant, colloidal probe, surface force, force curve, hydrophilic, hydrophilic, van der Waals force, silicon, silica, iron, HOPG, roughness.

Abstract Deutsch

Um die Handhabung von feinen Pulvern in industriellen Anwendungen zu optimieren, ist ein Verständnis der Wechselwirkungen zwischen einzelnen Pulverteilchen eine fundamentale Voraussetzung. Die Kräfte zwischen kolloidalen Teilchen bestimmen das Verhalten einer Reihe von Materialien wie Farben, Papier, Erdreich und eine Vielzahl industrieller Prozesse. Mit der Erfindung des Rasterkraftmikroskops (Atomic force microscope, AFM) wurde die direkte Messung der Wechselwirkung zwischen mikrometer-großen Teilchen möglich. Der adhäsive Kontakt zwischen einem Teilchen und einer Oberfläche ist ein wesentlicher Parameter für die Analyse von Haftkraftmessungen mit dem AFM. Ziel dieser Studie war es, die Oberflächenkräfte zwischen feinen Pulverteilchen besser zu verstehen. Ich habe die Haftkraft zwischen AFM-Spitzen oder Pulverteilchen, die an AFM-Federbalken befestigt waren, und verschiedenen Festkörperoberflächen gemessen. Es wurden sowohl glatte und homogene Oberflächen wie Siliziumwafer, Glimmer, kristallinem Graphit (HOPG) als auch rauere und heterogene Oberflächen wie Eisenteilchen oder regelmäßige Anordnungen von TiO_2 Nanoteilchen auf einem Siliziumwafer verwendet. Im ersten Teil habe ich mich mit der wohlbekannten Tatsache auseinander gesetzt, dass bei Haftkraftmessungen mit dem AFM nicht ein fester Wert, sondern recht breite Verteilungen der Haftkraft beobachtet werden. Meine experimentellen Resultate zeigen, dass sich die Schwankungen der Haftkraft zusammensetzen aus schnellen, zufälligen Fluktuation, die von einem Kraftmessung zur nächsten auftreten, und langsameren Schwankungen, die über einige zehn bis hundert aufeinaderfolgenden Messungen hinweg erfolgen. Diese langsamen Fluktuationen können nicht auf Schwankungen externer Einflussgrößen wie Kontaktposition, Temperatur, Luftfeuchte etc. zurückgeführt werden, da diese konstant gehalten wurden. Selbst wenn zwei Festkörper unter genau den gleichen Bedingungen (gleiche Stelle, Andruckkraft, Richtung usw.) in Kontakt gebracht werden, ist das Resultat für aufeinander folgende Messungen oft unterschiedlich. Die Messung selbst induziert strukturelle Veränderungen im Kontaktbereich, die zu einem geänderten Wert der Haftkraft in der nächsten Messung führen.

Im zweiten Teil dieser Arbeit untersuchte ich den Einfluss der Luftfeuchte auf die Haftkraft von Nanokontakten. Die Luftfeuchte wurde möglichst schnell variiert, um Verschleiß der AFM-Spitzen während einer Messreihe zu minimieren. Für hydrophobe Oberflächen wurde keine signifikante Änderung der Haftkraft mit zunehmender Luftfeuchte beobachtet. Für hydrophile Oberflächen ergab die Auftragung von Haftkraft gegen Luftfeuchte entweder ein Maximum oder einen kontinuierlichen Anstieg mit zunehmender Luftfeuchte. Dies kann mit einem einfachen Kontinuumsmodell der Kapillarkraft erklärt werden, das Rauhigkeit der Oberflächen berücksichtigt und verschiedene AFM-Spitzengeometrien oder Teilchenformen durch Überlagerung zweier Kugeln modelliert. Experimentelle Ergebnisse und Modellrechnungen zeigen, dass die genaue Kontaktgeometrie einen entscheidenden Einfluss auf die Abhängigkeit der Haftkraft von der Luftfeuchte hat. Änderungen der Spitzengeometrie auf der sub10 nm Längenskala können zu einer vollständigen Veränderung des Zusammenhangs zwischen Haftkraft und Luftfeuchte führen. Unser Modell erklärt somit auch die großen Diskrepanzen zwischen verschiedenen früheren AFM-Studien zur Abhängigkeit der Haftkraft von der Luftfeuchte.

بسم الله الرحمن الرحیم

چکیده فارسی :

برای بهینه نمودن فرایند جابجایی پودرهای ریز دارای کاربرد در تولیدات صنعتی، شناخت و درک بهتر از نیروهای برهمکنشی بین تک تک ذرات پودر بسیار مهم واساسی می باشد. در ضمن نیروهای بین ذرات کلوئیدی نیز بر چگونگی نحوه رفتار تعداد زیادی از مواد شامل رنگها ، کاغذ، خاک، و بسیاری دیگر از فرایند های صنعتی حاکم می باشد.

با اختراع میکروسکوپ نیروی اتمی ، اندازه گیری مستقیم واکنش بین ذرات در اندازه های میکرونی و زیر میکرون امکان پذیر گردید. اطلاعات مورد نیاز برای تجزیه و تحلیل تماس چسبنده بین یک ذره-ذره و یا ذره با یک صفحه صاف بوسیله داده های گرفته شده در روش اندازه گیری نیروی کشش-قطع توسط میکروسکوپ نیروی اتمی بدست آورده می شود.

هدف اصلی این مطالعه وتحقیق، افزایش شناخت و سطح درک برهمکنش بین ذرات بوده است. نیروی چسبندگی بین حسگر و یا ذرات کلوئیدی چسبانده شده به نگهدارنده حسگر میکروسکوپ نیروی اتمی با نمونه های از سطوح جامد اندازه گیری گردید. صفحات صاف و همگن همچون ویفر سیلیکون، میکا، و گرافیت پیرولیت با ساختار جهت دهی بسیار بالا و صفحات زبر و نا متجانس همانند میکرو ذرات آهن و الگویی از نانو ذرات اکسید تیتانیم قرارگرفته بر روی ویفر سیلیکونی مورد ازمایش و اندازه گیری قرار گرفت.

ابتدا برای درک بهتر از نیروی چسبندگی می توان گفت نتایج اندازه گیری شده توسط میکروسکوپ نیروی اتمی نشان می دهد که نیروی چسبندگی بین ذرات تک مقداری نبوده بلکه دارای توزیعی از نیرو می باشد. نتایج آزمایش ها نشان می دهد: تغییر در اندازه نیروی چسبندگی بسیار سریع اتفاق می افتد (برای مثال از یک منحنی نیرو تا منحنی نیروی بعدی اندازه گیری شده) و شامل افت وخیزهای تصادفی و افت و خیز های آهسته تر از زمان اندازه گیری نیرو می باشد، که صحت آن با بیش از ده تا صد اندازه گیری متوالی تأیید می گردد. افت و خیز های آهسته تر از زمان نیرو های چسبندگی ناشی از عوامل خارجی همچون سطح تماس، درجه حرارت، و رطوبت

نبوده است بدلیل اینکه در زمان آزمایش تمامی آنها ثابت نگهداشته شده بودند. حتی اغلب نیروی اندازه گیری شده بین دو جسم جامد دقیقاً در شرایط یکسان (محل تماس، نیروی اعمال شده، جهت و زاویه اندازه گیری، و...) نیز کاملاً برابر با نیروی اندازه گیری شده در همان نقطه در مرتبه بعدی نمی باشد. اندازه گیری ها نشان می دهند که مقدار هر نیروی اندازه گیری شده با نیروی بعدی بعلت تغییر در ساختار محل تماس دو جسم در زمان اندازه گیری متفاوت می باشد.

در بخش دوم اثر نفوذ رطوبت درمقدار نیروی چسبندگی برای نانو تماس ها مورد مطالعه و بررسی قرار گرفت. رطوبت محیط اندازه گیری برای کمترین سایش در نوک حسگر در کوتاه ترین زمان تغییر داده می شد. نتایج بدست آمده نشان می دهد: نیروی چسبندگی اندازه گیری شده بر روی صفحات آبگریز تغییر قابل ملاحظه و مهمی با تغییر رطوبت نمی کند. نیروی چسبندگی اندازه گیری شده روی سطوح آبدوست نشان می دهد که اندازه این نیرو با افزایش رطوبت بطور پیوسته افزایش می یابد تا به یک مقدار بیشینه برسد. نتایج بدست آمده را میتوان بوسیله تئوری پیوستگی و نیروی ناشی از تشکیل لایه محدب آب تشکیل شده بر روی سطح صاف محاسبه نمود. نیروی غشائی را بوسیله مدلی طراحی شده براساس تماس بین دو ذره کروی با سطوح زبر یا بین حسگر میکروسکوپ نیروی اتمی و سطح زبر محاسبه نمودیم. نتایج آزمایشگاهی و محاسباتی نشان میدهد که دقیقاً هندسه محل تماس تأثیر بسزایی در اندازه نیروی غشایی و در نهایت دروابستگی نیروی چسبندگی به رطوبت دارد.

تغییرات در شکل و اندازه نوک حسگر حتی در محدوده اندازه زیر 10 نانومتر نیز اندازه نیروی چسبندگی در محیط مرطوب را تغییر می دهد. مدلی که طراحی کردیم توانایی دارد تا تفاوت های نتایج مطالعات قبلی را نیز توضیح دهد که چرا نتایج بدست آمده قبل متفاوت بوده است.

کلید واژه: میکروسکوپ نیرو اتمی، نگهدارنده حسگر، ضریب سختی فنری حسگر، حسگر کلوئیدی، نیروی سطحی، نمودار نیرو، آبدوست، آبگریز، نیروی واندر والس، سیلیکون، سیلیکا، آهن، گرافیت پیرولیت با ساختار جهت دهی بسیار بالا، زبری.

ABSTRACT **I**

INDEX **IX**

1. INTRODUCTION **1**

2. FUNDAMENTALS **6**

2.1. SURFACE FORCES **6**

2.1.1. Van der Waals Forces **6**

2.1.1.1 Van der Waals forces between two molecules **6**

2.1.1.2. Van der Waals forces between macroscopic solids **9**

2.2. HAMAKER CONSTANT **10**

2.3. CONTACT MODELS **12**

2.3.1. Hertz model **12**

2.3.2. Surface energy and contact of elastic solids **14**
***(JKR model*).**

2.3.3. Effect of contact deformations on the adhesion **16**
of particles *(DMT)*

2.3.4. The JKR-DMT transition using a Dugdale model **18**
(Maugis model)

2.4. EFFECT OF PARTICLE RADIUS ON ADHESION FORCE **19**

2.5. EFFECT OF SURFACE ROUGHNESS ON **20**
ADHESION FORCE

2.6. LIQUIDS AND LIQUID/SOLID INTERFACES **21**

2.6.1. Contact angle **23**

2.6.2. Water adsorption on hydrophilic surfaces **25**

2.6.3. Capillary condensations **27**

2.7. MENISCUS FORCE **27**

2.7.1. Calculation of meniscus force for fundamental **28**

geometries

2.7.2. Calculation of meniscus force taking surface roughness into account **33**

2.7.3. A two-sphere-model to describe the meniscus force of an AFM tip **37**

2.7.4. Alternative model: Meniscus force for conical tip with a spherical end **40**

3. MATERIALS AND METHODS **44**

3.1. ATOMIC FORCE MICROSCOPY (AFM) **44**

3.1.1. AFM Imaging **46**

a) Contact Mode (CM) **46**

b) Intermitted Contact Mode (Tapping mode) **46**

***c)* Non Contact Mode (NCM)** **47**

3.1.2. AFM Force Spectroscopy **48**

a) Anatomy of a force curve **48**

b) Force Volume Mode (FV) and Adhesion Force Maps **50**

3.2. CANTILEVER AND SPRING CONSTANT **51**

3.2.1. Cantilever calibration methods **54**

3.2.1.1. Sader method **55**

3.2.1.2. Thermal noise method **56**

3.2.1.3. Reference spring method **59**

3.2.2. Colloidal probe and tip radius **60**

3.3. SURFACE PREPARATION **62**

3.3.1. Plasma cleaning **63**

3.3.2. RCA method (wet-cleaning method) **63**

3.3.3. Cleavage of crystals **64**

3.3.4. Etching of surfaces **64**

3.4. HUMIDITY CONTROL SYSTEM 65

4. RESULTS AND DISCUSSIONS 68

4.1. ADHESION FORCE DISTRIBUTION 68

4.1.1. Adhesion on hydrophilic surfaces 68

4.1.2. Adhesion on hydrophobic surfaces 70

4.1.3. Adhesion on spherical surfaces 72

***a)* Glass particle** 72

***b)* Iron particle** 73

4.1.4. Adhesion on rough surfaces 74

***a)* Silicon wafer surface** 74

***b)* Titanium oxide particles on silicon wafer** 75

***c)* Iron particles** 78

4.2. EFFECT OF LOAD 79

4.3. FACTORS INFLUENCING THE DISTRIBUTION OF ADHESION FORCES 80

4.4. INFLUENCE OF HUMIDITY ON ADHESION 85

4.4.1. Meniscus force on hydrophilic surface 87

4.4.2. Meniscus force on hydrophobic surface 90

***a)* HOPG surface** 90

***b)* Teflon surface** 92

4.5. SIMULATION OF EXPERIMENTAL RESULTS WITH THE TWO-SPHERE-MODEL 92

4.6. TIP WEAR 95

4.7. CONCLUSIONS 96

ACKNOWLEDGEMENTS 99

NOMENCLATURE 101

REFERENCES 104

1. INTRODUCTION

The interaction force between two solid surfaces, especially for small particles, is fundamental to the understanding of many natural phenomena, and in many industrial applications. Examples are particle aggregation and dispersal of powders and colloidal dispersions, the flow properties of granular materials, wafer cleaning in the semiconductor industry, and the formation of films in paints and coatings. Granular materials are the second most handled material in industry (after water) [1], and can show a complex flow behavior that is hard to predict, since no rheological law exists. Therefore industrial processing of granular matter is largely based on empirical observations especially for so-called cohesive powders, where pronounced adhesion forces between the particles are observed. Adhesion forces between particles and surfaces, i.e. the force necessary to detach a particle from a surface is of interest in several industrial applications such as detergency [2], particle filtration [3] and petroleum production [4, 5]. For biological systems such as cells or viruses, adhesion to surfaces is important for processes like biofilm formation or infection.

Real particles, however, are never completely rigid, and on coming into contact they deform elastically under the influence of any externally applied load as well as the attractive interface forces that pull two surfaces together, this gives rise to a finite contact area even under zero external loads. Several theories describe the elastic deformation of the sample. Differences in the relations between the applied load force and the contact area or surface deformation are due to the role played by the adhesion in the considered system. These theories have been developed by Hertz that adhesion is neglected [6], Johnson-Kendal-Roberts (JKR) [7], Derjaguin-Müller-Toporov (DMT) [8-10], and Maugis [6, 7, 11, 12]. In the Hertz model the adhesion is neglected, whereas the two other theories take account of it outside (DMT) or inside (JKR) the contact area. Maugis has shown that the JKR and DMT models are limits of the same theory, describing the elastic deformations of all samples as a function of a parameter that he defined. One relation he

determined was that contact between a planar surface and sphere pressed together with normal load P occurred within circular contact area with radius a. Johnson, Kendall and Robert (JKR) motivated by experimentally measured contact areas that were larger than predicted by the Hertz theory at low loads by the observation of finite contact area at zero applied loads. The surface forces outside the contact area are neglected and elastic stresses at the edge of the contact are infinite, as in linear elastic fracture mechanics. Derjaguin, Müller, Toporov (DMT) calculate adhesion force in the contact of elastic spherical particle and flat surface. They assumed that the deformed contact profile remained the same as in the Hertz model with external load force, but with an overall higher load due to adhesion. In the DMT model, the adhesion forces are taken into account area as if adhesion forces could deform the surface. The spatial range over which surface forces act depends upon the chemistry of materials in contact, and may or may not be long range compared to the scale of elastic deformations due to these forces [13, 14].

Different techniques have been developed to measure the adhesion force between particles and particles and substrates. The centrifugal technique is an established method to study adhesion forces between particles and planar surfaces that have been used for more than 40 years [15-17]. This method has been applied to characterize the behavior of powders in pharmaceutical or food applications [18-20].

Since its invention in 1986 [21], atomic force microscopy (AFM) can measure precisely surface forces and image surfaces with high resolution. The AFM in a variety of operational modes (contact mode, non-contact mode, tapping mode) has become a widely used experimental tools in surface physics and surface chemistry laboratories.

The contact area between two particles or a particle and a planar surface depend on the particles radius [22]. The adhesional contact area between a particle (AFM probe) and a substrate is a fundamental parameter for analyzing atomic force microscopy pull-off force data in terms of the work of adhesion, or solid surface energy [23]. In the real world, particles are not perfect spheres and surfaces of both particles and substrates are almost always rough at either a micro- or nano- scale or both [24]. Heterogeneity in chemical composition or molecular structure at different length scales can

cause a different energy of adhesion and thus can cause a variation in the effective adhesion force depending on the precise location of contact. The subject of surface heterogeneity is thoroughly discussed for wetting phenomena [25, 26].

One issue addressed here is concerned with the well-known fact that all adhesion experiments showed wide distributions of adhesion forces rather than a single value. Naively, one would expect that adhesion forces between similarly prepared particles of equal size should always be the same. This is, however, not the case. Wide distributions of adhesion forces are typically observed and adhesion forces vary by typically a factor of two to ten even within relatively monodisperse powders [17, 19, 22, 27-30].

As a cause of this variation surface roughness and surface heterogeneity have been suggested [31-37]. The decrease of adhesion with surface roughness can influence particle adhesion. The effect of the asperity is to avoid a closer contact between particle and surface, thus reducing the adhesion force [34]. Surface roughness can reduce the meniscus force [38]. To describe this mathematically roughness was modeled by a single spherical asperity [39-42].

To help understanding this variation I measured adhesion forces with an atomic force microscope and a sample in air at different humidity. The atomic force microscope (AFM) has emerged as a useful tool for studying surface interaction by mean of surface forces. A great deal of work has been performed on both its theoretical and experimental aspects. The heart of the AFM is a cantilever with a microfabricated tip that deflects when interacting with the sample surface [43]. Adhesion between different probes (microfabricated silicon or silicon nitride tip, spherical particle) and various sample surfaces was studied. Underlying questions were: Which factors influence the width of the distribution measured? What is the system with the lowest possible variation in the adhesion force? Here, a “system” is a particular combination of AFM probe and sample at a given humidity. Once this system with low variation was identified the next question was: What causes the higher variation in all the other systems? In this way, additional sources of variation can be identified and their relevance can be estimated.

The second issue addressed in this thesis is the influence of humidity on adhesion. It is well known that humidity influences the cohesion in powders and the adhesion of particles to surfaces [44-48]. One reason is certainly the meniscus force. Water condenses into the gap at the contact region between hydrophilic particles. In AFM measurements, capillary forces have been the focus of many studies due to their dominance in effective applied load between probe and surface in a humid environment [49, 50]. The capillary neck is formed between two surfaces due to the self-association of water and the strong adhesive properties of water towards between the surfaces. This formation has been extensively studied on different scales. The molecular self association in unfrozen bulk water, also referred to as structured water, forms a three dimensional hydrogen-bonded network that is very important in biological systems and processes. The equilibrium radius of the capillary bridge meniscus has long been described by the Kelvin equation [51, 52], which relates the relative vapor pressure to the curvature of the condensed liquid surface. The reduced Laplace pressure in the meniscus and the surface tension of the liquid cause an attractive force [53]. Many experiments showed a significant dependency of the adhesion force on the vapor pressure [52, 54-57].

To study the influence of humidity on the adhesion force a special setup was constructed, which allowed changing humidity relatively fast. This was important because I noticed significant tip wear, in particular at high humidity. Adhesion force-versus-humidity curves were measured for several combinations of AFM tips and surface materials. The experimental results were compared to results of calculations. Meniscus forces have been calculated for different geometries. To our knowledge meniscus forces were, however, not calculated as a function of humidity (exception ref. 35).

Results of other studies showed that due to the strong capillary condensation (on hydrophilic surfaces), the adhesion force between silicon nitride or silicon AFM tip and different clean and fresh surfaces such as mica and silicon wafer was observed to first increase and then decrease with an increase in humidity [42, 58, 59]. S. Rozhok *et al.* showed that adhesion force on NaCl substrate is a function of relative humidity too [60].

Magnitude of adhesion forces and their change with humidity depend on the surface chemistry and on the pressure of the water in the meniscus between particles or particle and sample surface. An increase in the relative humidity can produce substantial change in the processing powder characteristics of powders. It can even lead to a loss of process control [38]. A theoretical explanation for the absence of capillary force at low humidity was first given by Coelho and Harnby [61], where the meniscus associated with the powder particles consists of adsorbed water vapor. The experimental results showed that the value of humidity where the maximum of the capillary force was observed was determined by the equilibrium between the thin liquid film at the surface, the meniscus, and atmospheric humidity. Some results of our experiment showed that the magnitude of the adhesion forces changes on mica and quartz surfaces and observed that maximum of adhesion forces at relative humilities around 20% or less 45%. Results of other studies showed that meniscus force between silica particles [62, 63], a silica particle and a silicon wafer [64], between a silicon nitride tip and molybdenum trioxide [65], or pharmaceutical substances [66], and between silicon wafer and silicon nitride tip was at relative humidity around 70% [67]. In other cases adhesion force-versus-humidity curves showed a maximum [42, 58, 68], or a step-like increase [69]. On clean, freshly and cleaved mica a decrease of the adhesion force with increasing humidity was observed [70]; because the adhesion force measured above relative humilities 30-40%. At low humidity asperity of surface reduces the meniscus force by effectively reducing the radius of the interacting particles. In this study first, I measured value of adhesion force between AFM tip and fine particle and hydrophobic and hydrophilic planar surfaces. Second, I measured meniscus force between fine particles and planar surface in different humidity.

2. FUNDAMENTALS

2.1. SURFACE FORCES

Surface forces are the force acting between two surfaces in close proximity, and have their origin in the interatomic forces acting between all of the atoms of those bodies, as well as the atoms of any intervening medium. Many applications of colloid science come down to controlling force between colloidal particles, between particles, or particles and surface. For two bodies coming into contact, we have to consider the balance between attractive surface forces and repulsion due to elastic deformation within the contact region. In this chapter, I will first give an introduction into surface forces and then describe the fundamental theories about contact mechanics.

2.1.1. Van der Waals force

Among the many contributions to the interaction between surfaces and particles, there is one type of interaction which is always present, the van der Waals interaction. This ubiquitous interaction may be of varying importance depending on the system but is usually the dominating contribution to particle adhesion apart from meniscus forces. In 1873 the van der Waals noted the non-ideality of gases and attributed it to the existence of molecular or atomic interactions. In fact these interactions were correctly thought to be due to interacting dipoles but incorrectly assumed to be solely due to static dipole moments. A full understanding of the van der Waals force became possible only after the development of quantum theory, that allowed to describe the charge fluctuation present in atoms and molecules.

2.1.1.1. Van der Waals force between molecules

Since the van der Waals force stems from molecular interactions, it is instructive to start out with the description of the interaction between atoms and molecules. All objects experience an attraction due to gravitation force;

however, it is much too weak to play a significant role for inter molecular interactions.

The van der Waals force actually consists of three components Keesom, Debye, and dispersion forces [71] (Fig.2.1).

The Keesom force is the intermolecular force resulting from the angle-averaged dipole-dipole interaction between two atoms or molecules with permanent dipoles that are allowed to rotate freely (Willem Hendrik Keesom 1921). The Keesom force depends on physical characteristics such as dipole moments of interacting molecules, distance, dielectric permittivity of vacuum and interaction media between both dipoles [72].

The Debye force is the interaction between one permanent dipole and one induced dipole in or in other words, between a dipolar molecule and a polarizable molecule. The energy of interaction between these two dipoles is simply the energy of an induced dipole in the electric field of the first permanent dipole [72]. The microscopic electric polarizability of an atom refers to its ability to respond to an external electric field by shifting its charges so as to create a dipole oriented favorably in the external field. For an isolated atom this may occur by biasing the time-average distribution of electrons among ground and excited state to favor polar states. If excitation is easy, polarizability is high. For molecules in the gas or liquid state skeletal vibrational states and rotational states may also contribute to the polarizability. Molecules that bend easily to produce a dipolar configuration have high polarizability.

The London or dispersion force (London, 1936) is the interaction between two induced dipoles due to quantum mechanical fluctuations of the charge distribution. For two molecules A and B sufficiently close to each other, the fluctuation in charge distribution of molecule A propagate a complex electromagnetic field into the surrounding space, the frequencies of which are those of the fundamental intermolecular motion. The field travels through space until it reaches molecule B which is then polarized. The induced dipole of molecule B moves in phase with the original dipole and re-radiates an electromagnetic filed which is propagated back to A [73]. This leads to an attractive force between A and B.

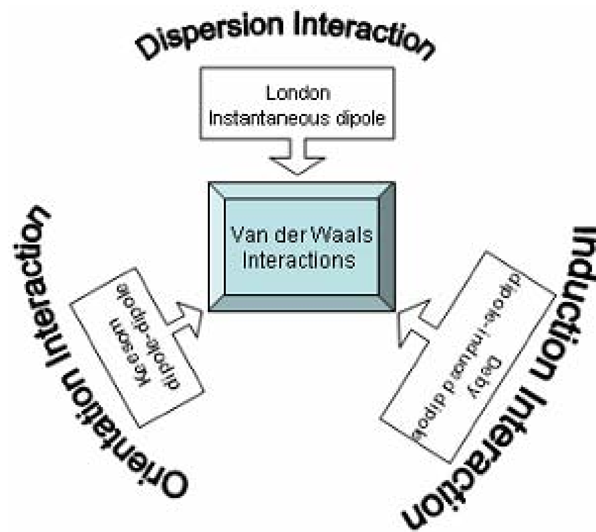

Fig.2.1 Contribution to the van der Waals interaction

The van der Waals force is the sum of these three forces. Since all three interaction potentials are proportional to r^{-6} the van der Waals interaction energy at a distance r can be written as [74].

$$w(r) = -\frac{C_{AB}}{r^6} \tag{2- 1}$$

The minus (-) sign resembles the fact that the van der Waals force is usually attractive. C_{AB} is a constant that depends on the properties of the interacting objects and the medium in between[75]. The van der Waals force is short-range force and, depending on the situation, can be effective from long-range distances of ~10 nm down to interatomic spacing (about 0.2 nm) [51].

Quantum theory shows that treatment of the interaction energy, which can be represented by a summation of Coulomb interaction between the electrons and nuclei of the molecules [73]. When the dipoles are separated by more than ~10 nm, the time taken for the electric field of the first dipole to reach the second and return can become comparable with the period of the fluctuating dipole itself. When this happens the field returns to find that the direction of the instantaneous dipole is now different from original and less favorably disposed to an attractive interaction. Thus, with increasing separation the dispersion energy between two atoms begins to decay even faster than $-\frac{1}{r^6}$,

approaching a $-\frac{1}{r^7}$ dependence at r > 100 nm. This is called the retardation effect, and therefore one speaks about retarded van der Waals forces for larger separations.

2.1.1.2. Van der Waals force between macroscopic solids

In order to calculate the forces between macroscopic bodies, we can sum up the forces between the singles atoms or molecules within the bodies. This includes the assumption of pair wise additivity, i. e. the assumption that the interaction between two molecules is not changed by the presence of a third. The first step is the calculation of the force between a single molecule and a planar surface.

Now we want calculate van der Waals force between a molecule that is a small distance from an infinite flat plane (fig.2.2).

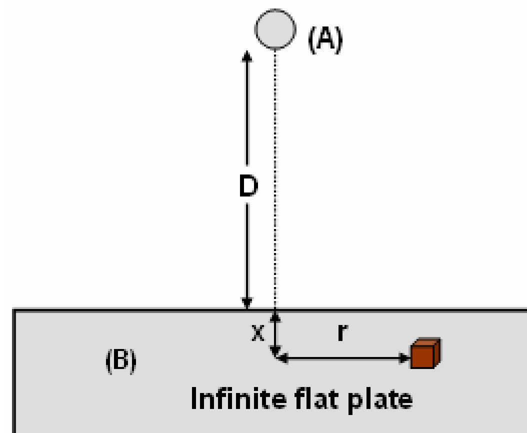

Fig.2.2 Calculating the van der Waals force between a molecule and a planar surface

To calculate the interaction energy between a molecule A and an infinitely flat planar substrate made of molecules B we use Eq.2.1 and integrate the van der Waals energy between one molecule A and all molecules B [75]

$$W_{Mol/Plane} = -C_{AB} \cdot \iiint \frac{\rho_B}{D^{r^6}} dV = -C_{AB\rho_B} \cdot \int_0^\infty \int_0^\infty \frac{2\pi r dr dx}{((D+x)^2 + r^2)^3} \qquad (2\text{- }2)$$

If we use cylindrical coordinates and assume that the density of molecules B in the solid is constant, this can be written as:

$$W_{Mol/Plane} = -\pi\rho_B C_{AB} \cdot \int_0^\infty \int_0^\infty \frac{d(r^2)}{((D+x)^2 + r^2)^3} dx \qquad (2\text{- }3)$$

$$W_{Mol/Planne} = -\frac{\pi\rho_B C_{AB}}{6D^3} \qquad (2\text{- }4)$$

Here we note that in this case interaction energy between one molecule and infinite plane is proportional to D^{-3}. As the next step, we calculate the interaction energy between two infinite planar surfaces that are at distance *D*. This can be achieved by using Eq.(2.4) and integrating over all molecules in the solid A:

$$W = -\frac{\pi C_{AB\rho_B}}{6} \iiint \frac{\rho_A}{(D+x)^3} dV = -\frac{\pi C_{AB\rho_B}}{6} \int_0^\infty \int_{-\infty}^\infty \int_{-\infty}^\infty \frac{\rho_A dzdydx}{(D+x)^3} \qquad (2\text{- }5)$$

Here, y and z are the coordinates parallel to the gap.

This integral would diverge due to the infinite area of the surfaces. Therefore we calculate the energy per unit area:

$$w = \frac{W}{A} = -\frac{\pi\rho_A\rho_B C_{AB}}{12D^2} \qquad (2\text{- }6)$$

If we define the Hamaker constant as

$$A_H = \pi^2 \rho_A \rho_B C_{AB} \qquad (2\text{- }7)$$

then

$$w = -\frac{A_H}{12\pi D^2} \qquad (2\text{- }8)$$

The force per unit area is equal to the negative derivation of w versus distance:

$$f = \frac{A_H}{6\pi D^3} \qquad (2\text{-}9)$$

2.2. HAMAKER CONSTANT

As seen in Eq.2-8, there is a direct proportionality between the magnitude of the van der Waals interaction and the Hamaker constant. The Hamaker constant is a material constant that depends on the properties of two materials (e.g. dielectric permittivity, charge density, mass density) and the

intervening media. The distance dependence of the van der Waals energy depends essentially on the geometry of the two interacting bodies being proportional to D^{-2} for parallel plates and scale to D^{-1} for two spherical particles at short separation distances where retardation can be ignored. In allows calculating the Hamaker constant for the interaction of two media 1 and 2 across a third medium 3 (Fig.2.2) according to (Israelachivili, 1992, p.181):

$$A_H = \frac{3}{2} kT \sum_{n=0,1,',,,}^{\infty} \left[\frac{\varepsilon_1(i\nu_n) - \varepsilon_3(i\nu_n)}{\varepsilon_1(i\nu_n) + \varepsilon_3(i\nu_n)} \right] \left[\frac{\varepsilon_2(i\nu_n) - \varepsilon_3(i\nu_n)}{\varepsilon_2(i\nu_n) + \varepsilon_3(i\nu_n)} \right] \quad (2\text{- }10)$$

After replacing the sum by an integral we can write

$$A_H \approx \frac{3}{4} kT (\frac{\varepsilon_1 - \varepsilon_3}{\varepsilon_1 + \varepsilon_3})(\frac{\varepsilon_2 - \varepsilon_3}{\varepsilon_2 + \varepsilon_3}) + \frac{3h}{4\pi} \int_{\nu_1}^{\infty} (\frac{\varepsilon_1(i\nu) - \varepsilon_3(i\nu)}{\varepsilon_1(i\nu) + \varepsilon_3(i\nu)})(\frac{\varepsilon_2(i\nu) - \varepsilon_3(i\nu)}{\varepsilon_2(i\nu) + \varepsilon_3(i\nu)}) d\nu \quad (2\text{- }11)$$

here, h is Planck's constant. The indices 1, 2, 3 denote the dielectric constant of substrate 1, substrate 2 and the medium in between, respectively. The integration is carried out over all frequencies ranging from

$$\nu_1 = \frac{2\pi k_B T}{h} \quad (2\text{- }12)$$

to infinity.

The dielectric constant varies with frequency. For a dielectric medium it can be approximated by

$$\varepsilon(i\nu) = 1 + \frac{n^2 - 1}{1 + \left(\frac{\nu}{\nu_e} \right)^2} \,. \quad (2\text{- }13)$$

Table 1

	Particle material/ Sample	$A_H\ (\times 10^{-19} J)$	Ref.
1	TiO2 /TiO2	6.6 ± 0.2	[76]
2	Si3N4/Mica	0.06	[77]
3	Si3N4/Si3N4	0.32	[78]

Table 1: Hamaker constants (A_H) for several materials assuming that the intervening medium is water

2.3. CONTACT MODELS

To understand the contact forces between bodies, one has to take into account deformation of the contact. This deformation may be due to external load, but even in absence of external force, the surface forces will lead to a contact deformation. In the following I will shortly review the four most common mechanical contact mechanics models.

2.3.1. Hertz model

In 1881 Hertz described his contact theory between a sphere and a planar surface [6]. The sphere with radius *R* is assumed smooth and elastic, while the planar surface is assumed to be rigid. Since the Hertz theory does not take into account surface forces, the radius of contact area between particle and planar surface in the absence of an external load is zero and no deformation is observed (Fig.2.3 A). Consequently, there is also no adhesion force between particle and surface. When a load *F* is applied to press the particle onto the planar surface (Fig.2.3 B), the deformation leads to a contact radius a_0 that is given by [43]:

$$a = \sqrt[3]{\frac{RF}{K}} \qquad (2-14)$$

and the overlap δ between the particle and surface is given by:

$$\delta = \frac{a^2}{R} = \frac{F}{Ka} \qquad (2-15)$$

in these equations, *K* is the so-called reduced Young's modulus which is given by:

$$\frac{1}{K} = \frac{3}{4}\left(\frac{1-v^2}{E} + \frac{1-v_i^2}{E_i}\right) \qquad (2-16)$$

In Eq.2-16 v and v_i are the Poisson ratios, E, E_i are Young's moduli of spherical particle and planar surface. With the definition of $X = \frac{y}{a}$, where y is the distance between the center of the sphere and the contact point, the pressure is given by:

$$P(x) = \frac{3Ka\sqrt{1-X^2}}{2\pi R} = \frac{3F\sqrt{1-X^2}}{2\pi a^2} \tag{2- 17}$$

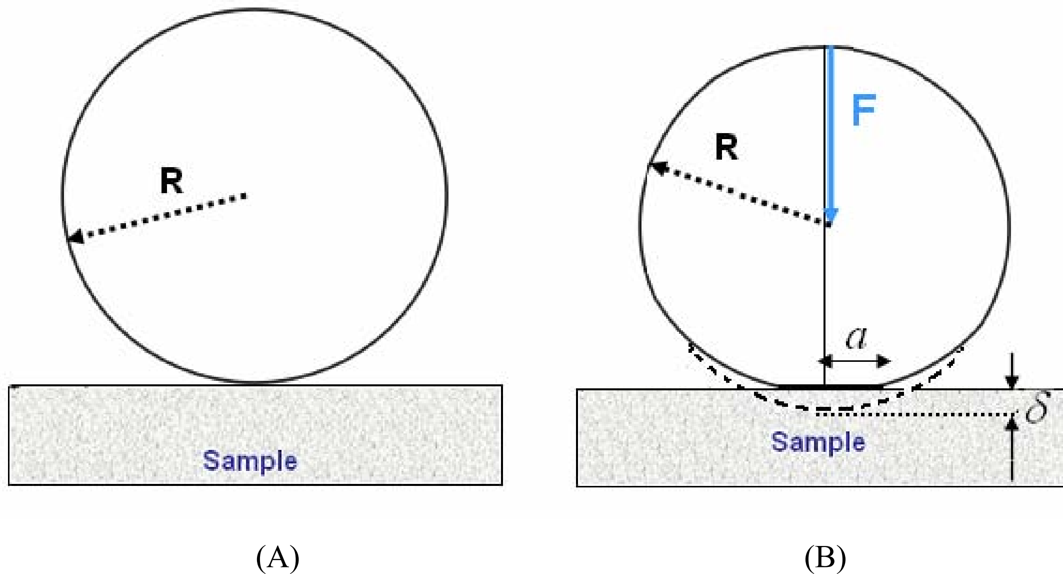

(A) (B)

Fig.2.3 An elastic deformation of spherical particle on surface sample following Hertz theory: (A) without loading force, (B) with loading force F

In1896 Hertz also calculated the elastic force between two spheres and used optical microscopy to measure the contact area between them (Fig.2.4).

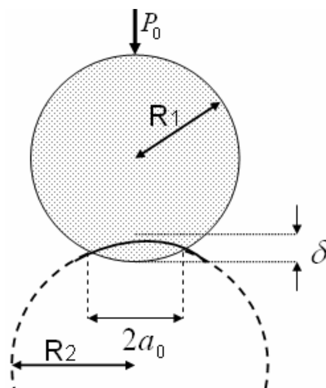

Fig.2.4 Two spherical particles in contact

For two spheres of radius R_1 and R_2 pressed together under a load F the radius a_0 of the circle of contact is given by:

$$a_0 = \frac{3}{4}\pi(k_1 + k_2)\frac{R_1 R_2}{R_1 + R_2}F \tag{2- 18}$$

where k_1 and k_2 are the elastic constants of the material of the spheres:

$$k_1 = \frac{1 - \nu_1^2}{\pi E_1} \tag{2- 19}$$

$$k_2 = \frac{1 - \nu_2^2}{\pi E_2} \tag{2- 20}$$

where ν is the Poisson ratio and E the Young's modulus of each material.

Resulting from local compression in the contact region, the two spheres overlap approaches each other by a distance δ which is given by:

$$\delta^3 = \frac{9}{16}\pi^2 (k_1 + k_2)^2 \frac{R_1 + R_2}{R_1 R_2} F^2 \ . \tag{2- 21}$$

2.3.2. Surface energy and contact of elastic solids (JKR model)

The theory of K. L. Johnson, K. Kendall, and A. D. Roberts [7] was the first to determine the agreement relationship for the contact of elastic spheres taking interaction of the surfaces into account. They considered only the change in energy that arises from the formation of a contact surface between the bodies. This interaction energy is then simply equal to the surface energy of the interfaces times the contact area. Interaction outside the contact area is neglected. The primary impetus for their work was to determine the 'pull-off' force between contacting spheres. The 'pull-off' force is defined as the external negative load at which the system becomes unstable i.e. the force at which abrupt separation occurs.

Robert's (1968) using smooth rubber spheres and Kendal (1969) using glass spheres noted that at low load contact areas between these objects were considerably larger than those predicted by Hertz and tended towards a finite value as load was reduced to zero [7]. Strong adhesion was observed if the surfaces were clean and dry. At high loads the agreed to the Hertz theory. These observations strongly suggested that attractive surface forces were operating between the solids and although these 'additional' contact forces were of little significance at high loads they became increasingly important as the load was reduced towards zero.

Consider two elastic spheres in contact under zero external loading force. If attractive forces are acting between the surfaces, they will lead to a

deformation and the formation of a finite contact radius a (Fig.2.4). The formation of the finite contact area is connected to a change in surface energy. Eventually a balance will be established between stored elastic energy and lost surface energy. The loss in surface energy is given by:

$$U_s = -\pi a^2 \gamma \tag{2- 22}$$

where γ is the surface energy per unit contact area. Force due to this energy change is:

$$F_s = -\frac{dU_s}{dx} \tag{2- 23}$$

where x is the relative displacement of the bodies and is a approximately the same as δ given by the Hertz equations (Eqs.2-18, 2-21) but can not be worked out exactly from these because the attractive surfaces disturb the stress distributions in the bodies. Thus one may only write that

$$x \approx \frac{a^2(R_1 + R_2)}{R_1 R_2} \tag{2- 24}$$

A combination of equations (2-23) and (2-24) gives

$$F_s \approx \pi\gamma \frac{R_1 R_2}{(R_1 + R_2)} \tag{2- 25}$$

This force acts in addition to the ordinary load P_0 between surfaces and the simple analysis shows that it may be related to the geometry and energy of the contacting surfaces. Further, the surface force will strongly influence the contact size when

$$P_0 \approx \pi\gamma \frac{R_1 R_2}{(R_1 + R_2)} \tag{2- 26}$$

When no surface forces act, the contact radius a_0 is given by the generalized Hertz equation:

$$a_0^3 = \frac{RP_0}{K} \tag{2- 27}$$

where

$$R = \frac{R_1 R_2}{(R_1 + R_2)} \text{ and } K = \frac{4}{3\pi(k_1 + k_2)}. \tag{2- 28}$$

The movement δ of the applied load is given by:

$$\delta = \frac{a^2}{R} \tag{2- 29}$$

Now if attractive forces act between the surfaces the contact radius in equilibrium will be a_1, which is greater than a_0. Although the applied load remains at P_0, an apparent Hertz load P_1 corresponding to the contact radius a_1 may be defined such that ($a_1 \succ a_0$), then:

$$a_1^3 = \frac{RP_1}{K} \tag{2- 30}$$

The load-displacement relation is then given by:

$$\delta = \frac{2}{3}\frac{F_{Ad}}{Ka_1}. \tag{2- 31}$$

The surface energy U_s is given by

$$U_s = -\gamma\pi a_1^2 = -\gamma\pi(\frac{RP_1}{K})^{\frac{2}{3}} \tag{2- 32}$$

where γ is the energy of adhesion of both surface.

Therefore at equilibrium, separation of the sphere will just occur when

$$F_{ad} = -\frac{3}{2}\gamma\pi R \tag{2- 33}$$

which they note is independent of the elastic modulus.

2.3.3. Effect of contact deformations on the adhesion of particles (DMT model)

When surface forces are short range in comparison to the elastic deformation of the contact (i.e. compliant particle and/or surface, strong adhesion forces, large particles), the JKR model gives a good approximation of the contact mechanics. But for stiff materials, weak adhesion forces and small particles one can not neglect the surface forces acting outside the contact area. Derjaguin-Müller-Toporov (DMT) [8] took also the forces acting between to bodies outside the contact area into account (Fig.2.5). These forces alone produce a finite area of contact. This leads to an area of contact that is bigger than predicted by the Hertz model. If the external loading force is negative, the contact area decreases until it reaches zero. At this point the pulling force reaches its maximum value.

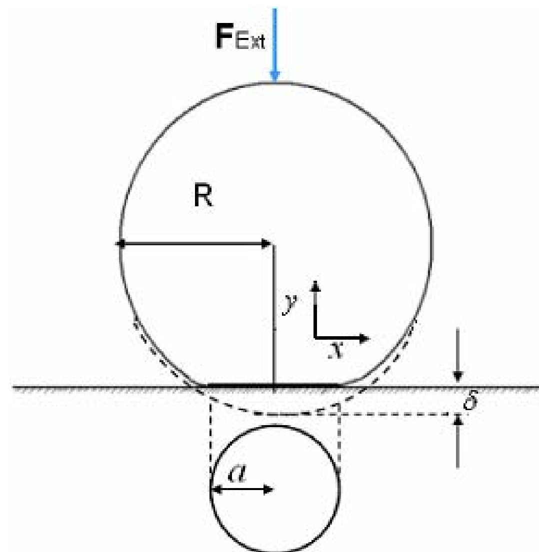

Fig.2.5 Deformation of particle on surface with external force (DMT)

They calculated adhesion force and contact area. The corresponding expressions are found by minimizing the integrated elastic and the surface energy. For the adhesion force, they found a similar expression as for the JKR theory for a sphere of radius *R* pressed onto a flat surface with a external force *F.* The adhesion or pulling force F_{ad}, the contact radius a, the contact radius at zero load a_0, the deformation δ of the spherical particle, and the pressure *P* are given by:

$$F_{Ad} = 2\pi RW \qquad (2\text{-}34)$$

$$a_0 = \sqrt{\frac{2\pi W}{K} R^2} \qquad (2\text{-}35)$$

$$a = \sqrt{(F_{Ad} + 2\pi RW)\frac{R}{K}} \qquad (2\text{-}36)$$

$$\delta = \frac{a^2}{R} \qquad (2\text{-}37)$$

$$P(X) = \frac{3Ka\sqrt{1-X^2}}{2\pi R} = \frac{3F\sqrt{1-X^2}}{2\pi a^2} \qquad (2\text{-}38)$$

in which $X = \frac{y}{a}$, is the distance from the center of the contact circle.

DMT theory is applicable for systems with low adhesion and small particles (e.g. AFM probes with small radii made of stiff materials).

2.3.4. The JKR-DMT transition using a Dugdale model (Maugis model)

In 1992, Maugis [79] elegantly showed that the JKR and DMT were actually limiting cases of a more general theory that can be applied for the entire range of material parameters. He describes attractive forces between two contacting spheres with a Dugdale potential (Fig.2.6).

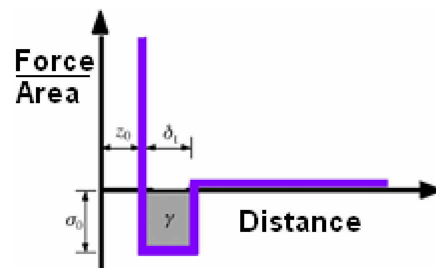

Fig.2.6 The force-distance relation for the Dugdale model by Maugis [80].

A constant adhesive stress (force per unit area) σ_0 acts between the surfaces over a range δ_t. At greater separations, the attractive force is zero. The work of adhesion is thus $\gamma = \sigma_0 \delta_t$ [13] .

Thus, the work of adhesion is:

$$\gamma = \sigma_0 \times \delta_t . \qquad (2\text{- }39)$$

The so-called Maugis parameter is defined as

$$\lambda = 2\sigma_0 \left(\frac{R}{\pi \gamma K^2}\right)^{\frac{1}{3}} \qquad (2\text{- }40)$$

or

$$\lambda = \frac{2.06}{Z_0}\sqrt{\frac{RW^2}{\pi K_2}}, \qquad (2\text{- }41)$$

in which Z_0 is again a typical atomic dimension.

Maugis showed that when λ increases from zero to infinity there is a continuous transition from the DMT approximation to the JKR approximation. If $\lambda \succ 5$, the JKR model applies and if $\lambda \prec 0.1$, the DMT model applies. Values

between 0.1 and 5 correspond to the 'transition regime' between JKR and DMT models (Fig.2.7).

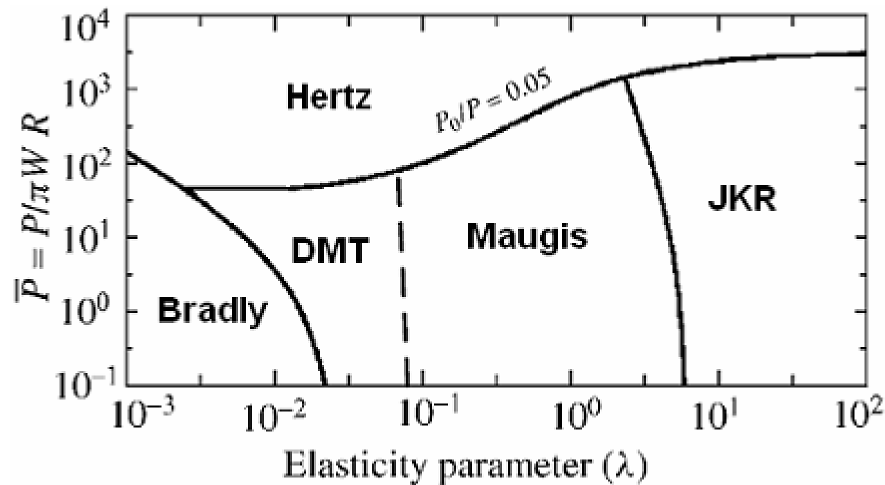

Fig.2.7 Map of behavior of bodies in different contact models [43]

2.4. EFFECT OF PARTICLE RADIUS ON ADHESION FORCE

The surface forces between particles and between a planar surface and a particle depend on the radius of particle. For two rigid incompressible spheres with radii R_1 and R_2 the adhesion force between them related to the work of adhesion by Derjaguin's approximation in DMT model:

$$F = 2\pi\gamma\left(\frac{R_1 R_2}{R_1 + R_2}\right). \quad (2\text{-}42)$$

If we assume that the spheres are made of the same material, this simplifies to:

$F = 2\pi R\gamma_{SL}$ two spheres in liquid (2- 43)

$F = 2\pi R\gamma_{SG}$ two spheres in vapor (2- 44)

$F = 4\pi R\gamma_{SL}$ sphere and plate in liquid (2- 45)

$F = 4\pi R\gamma_{SG}$ sphere and plate in vapor. (2- 46)

here γ_{SL}, and γ_{SG} are surface tension between of the solid-liquid and solid-gas interface respectively. Eqs.(2-43)-(2-46) show that adhesion forces depend on radius of silica particles (Fig.2.8). Fig.2.8 shows that adhesion forces versus reduced particle radii, the adhesion force increases linearly by increasing reduced radius *R*.

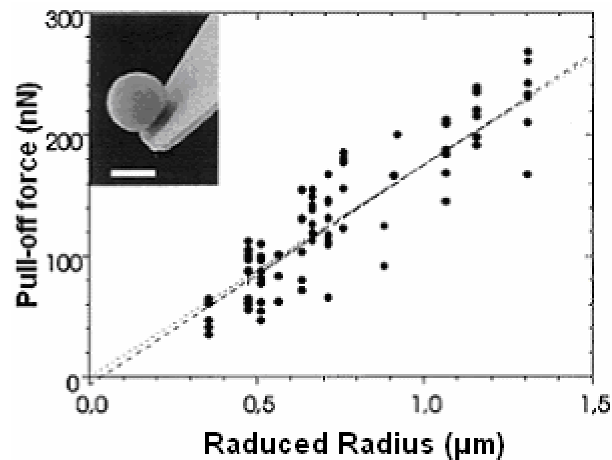

Fig.2.8 Pull-off force versus reduced particle radius obtained from direct force measurements between silica microspheres [22]. Each data point (solid circles) is an average value from seven adhesion measurements obtained with one pair of microspheres. The dashed line represents the best linear regression fit and gives a pull-off force of -6 nN at vanishing particle radius. The best linear fit to the data points through the origin of the diagram has a slope of 0.176 N/m (dotted line). The inset shows a SEM image of a silica microsphere glued to the end of an AFM cantilever. The scale bar indicates 3μm [22].

2.5. EFFECT OF SURFACE ROUGHNESS ON ADHESION FORCE

It is known from powder technology that the flowabilty can be improved by coating particles with second fraction of much smaller ones, thereby increasing the surface roughness and decreasing the contact area between particles [81]. The decrease of adhesion with surface roughness can influence particle adhesion. Results of some early measurements showed that adhesion forces between particles and surface determined with the colloidal probe technique were much lower than expected for a simple sphere-plate geometry and this was attributed mainly to the roughness of the contacting surfaces [82, 83]. The most popular models for smooth particle interacting with a smooth substrate were derived by JKR, DMT, and Maugis models [32]. Contact between rough surfaces has been studied for decades. Some other contact models have been based on the superposition of contact made by surface asperities. Roughness or asperities of surface significantly reduce the area of intimate contact of two particles or particle and planar surface because roughness surfaces can not come closer together [84] and strength

adhesion force dependent directly upon the area of contact then precisely changes adhesion force.

A theoretical model can describe the influence of surface roughness on adhesion force [85, 86]. Earlier models assumed perfect elasticity, spherical shape, and a constant radius of curvature for the asperities [87]. It is well know from colloid science that van der Waals interactions strongly depend on the geometry of the particle and surface. Geometrical aspects of van der Waals interactions are well treated in the Hamaker approach [88]. Hamaker approach area is widely used to model interaction of rough particles [31, 40].The modeling of adhesive contact between rough surfaces is more difficult because of variation in the heights and size of asperities and interaction between asperities. Fuller and Tabor [84] studied the effect of roughness on adhesion by experiments and made a numerical analysis based on JKR theory [89]. Cheng *et al*. studied the effect of sub micrometer-to-nanometer scale roughness on adhesion by assuming that surface roughness is random and homogeneous. Rabinovich *et al.* considered the adhesion between a smooth particle and a rough surface [34, 35]. Rabinovich models roughness as a distribution of closely packed hemispheres with equal radius (the asperity radius) r having their origin below the average surface, each protruding from this surface to a maximum peak height. On the smooth surface, however, that exhibited very regular surface features on the length scale of the particle; the adhesion was highest, probably due to high particle adhesion in valleys. Zhou *et al.* [90] showed that the adhesion between different particles of irregular shape and substrates of defined roughness can be minimized by tailoring the roughness of the contacting materials. In this study I take surface roughness into consideration and show that surface roughness can explain the typical curves (adhesion force on different humidity) observed experimentally. I introduced more realistic asperities, such as conical asperities or spherical asperities on the planar surface which our results coincide with spherical asperities simulation model.

2.6. LIQUIDS AND LIQUID/SOLID INTERFACES

Experimental studies of the liquid-solid interface are complicated because

the interface is embedded and involves only a small number of atoms relative to the bulk liquid and solid. In macroscopic terms, the boundary between a liquid in contact with a solid surface is described by a surface energy that determines how the liquid wets or spreads out on the surface. When surface energy is high (hydrophilic surface), wetting is limited; and the surface energy is low like mica (hydrophobic surface), there is nearly complete wetting; in between; one talks about partial wetting. On a microscopic level, the interface is a two-dimensional surface with macroscopic dimensions along the contact surface, while perpendicular to the surface, it is often considered as a discontinuity with infinitesimal thickness.

The surface tension of liquids has been understood and measured since the time of Young's and Laplace[91]. In 1884 van der Waals proposed a deep and elegant theory of the surface tension of liquids, which has since been rediscovered, and give important extensions, by Cahn and Hilliard [92].

A thought experiment can help us to understand that effect of intermolecular interaction and surface tension [75]. A relatively thin liquid film is spanned over a frame, which has a mobile slider (Fig.2.9).

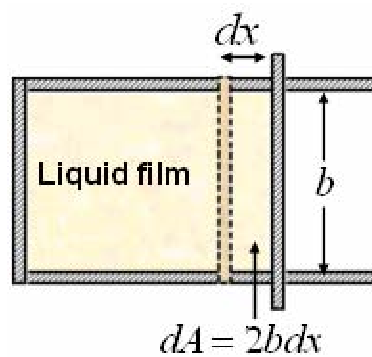

Fig.2.9 Thought experiment on surface tension [75].

If we move the slider a small distance dx to right side to increase the thin film area by dA, we have to do the work:

$$dw = \gamma \cdot dA \tag{2- 47}$$

where γ is proportionality constant and

$$dA = 2bdx\,. \tag{2- 48}$$

The surface tensional force pulling on the slider is given by:

$$F = -\frac{dw}{dx} = -2b\gamma \, . \qquad (2\text{-}49)$$

The proportionality constant γ depends on the composition of the liquid and the vapour, temperature, and pressure, but it is independent of the area.

2.6.1. Contact angle

When we put a drop of liquid on a solid surface the edge usually forms a defined angle which depends only on the liquid and the solid surface properties (Fig.2.10). This is the contact angle. In 1805 Young has recognized a relation between contact angle and surface tensions. Young's equation (Eq.2-50) is the basic for a quantitative description of wetting phenomena. If a drop of liquid is placed on solid surface there are two possibilities: the liquid spreads on the surface completely (contact angle $\Theta = 0°$) or a finite contact angle is established. In the latter case a three-phase contact line (also called wetting line) is formed. At this line three phases are in contact: the solid, the liquid, and the vapor (Fig.2.10).

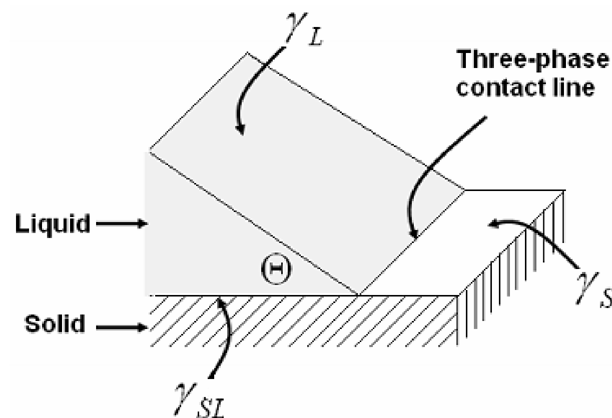

Fig.2.10 Rim of a liquid drop with a contact angle Θ on a solid surface.

Young's equation relates the contact angle to the interfacial tensions γ_S, γ_L, and γ_{SL}, [93],[94]:

$$\gamma_{LV}\cos\Theta = \gamma_{SV} - \gamma_{SL} \quad \text{or} \quad \cos\Theta = \frac{\gamma_{SV} - \gamma_{SL}}{\gamma_{LV}} \qquad (2\text{-}50)$$

where γ_S and γ_L are surface tension of Solid and Liquid, and γ_{SL}, γ_{SV}, γ_{LV} are surface tension between solid-liquid, solid-vapor, and liquid-vapor, and Θ is contact angle. If interfacial tension of the bare solid surface is higher than

that of the solid-liquid interface ($\gamma_S \succ \gamma_{SL}$), the right hand side of Young's equation is positive. The $\cos\Theta$ has to be positive and the contact angle is smaller than 90°; then liquid partially wets the solid. If the solid-liquid interface is energetically less favorable than the bare surface ($\gamma_S \prec \gamma_{SL}$), the contact angle will exceed 90° because $\cos\Theta$ has to be negative.

The contact angle is specific for any given system and is determined by the interaction across the three interfaces. Most often the concept is illustrated with a small liquid droplet resting on a flat horizontal solid surface. The droplet should be as small as possible because the force of gravity can actually change the above-mentioned angle. The shape of the droplet is determined by the Young-Laplace equation.

To understand the wetting behavior of liquid on a solid surface one first must know the physical and chemical properties of liquid and surface. In wide range of pure and applied science it is important to determine of solid-vapor (γ_{SV}) and solid-liquid (γ_{SL}) interfacial tensions [95]. Because of the difficulties involved in measuring directly the surface tension involving a solid phase, indirect approaches are called for: several independent approaches have been used to estimate solid surface tensions and contact angles [96-99]; including direct force measurements [7, 82, 100-106]. The direct measuring of interfacial is difficult that applied in Lifshitz theory of van der Waals forces [107-109].

Contact angle measurement is easily performed by establishing the angle of a liquid drop with a solid surface at the base. The attractiveness of using contact angles Θ to estimate the solid-vapor and solid-liquid interfacial tensions is due to the relative ease with which contact angles can be measured on suitably prepared solid surfaces[80]. The contact angle of a liquid drop on a solid surface is defined by mechanical equilibrium of the drop under the action of three interfacial tensions (Fig.2.11).

Young's equation (Eq.2-50) contains only two measurable quantities, the contact angle Θ and the liquid-vapor surface tension, γ_{LV}. In order to determine γ_{sv} and γ_{sl}, an additional relation relating these quantities must be sought. On rough solid surfaces, contact angles are meaningless in terms of

Young's equation. On very rough surfaces, contact angles are larger than on chemically identical, smooth surfaces [110]. On smooth, but chemically heterogeneous solid surface, contact angle is not necessarily equal to the thermodynamic equilibrium angle. This has been illustrated using a model of a vertical surface consisting of heterogeneous and smooth strips [95]. The wetting behavior of small particles is important in many industrial application and natural phenomena (e.g. paint industry and mineral processing), a property usually characterized in terms of the solid-liquid contact angle [111]. The contact angle of powders is usually measured with the capillary rise technique [112-115].

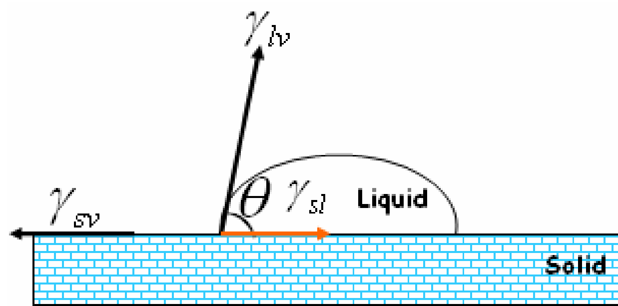

Fig.2.11 Liquid drop with circular contact area on a flat surface

2.6.2. Water adsorption on hydrophilic surfaces

For discussing the effect of humidity and meniscus force let us start this section with a brief comment about the bare silicon wafer surface. After the cleaning with RCA method (see section 3.3.2), the surface is fairly hydrophilic, bearing hydrophilic silanol groups and hydrophobic siloxane bridges. As water molecules are brought into contact with the surface at the end of the cleaning [116, 117]. I expect each silanol to be engaged in a hydrogen bond with a water molecule. This molecule can in turn be linked to other water molecules. However, water begins to attack the siloxane (Si-O-Si) bonds forming silanol (Si-OH) groups (Fig.2.12).

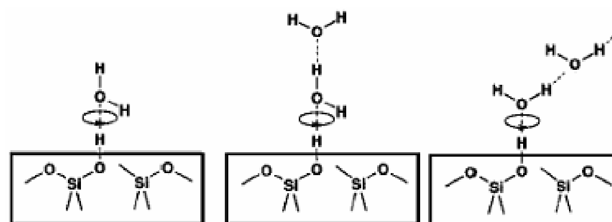

Fig.2.12 Water molecules adsorb on clean silicon wafer surface

Changing RH changes the number of these secondary linked molecules. But even at the lowest RH, the first water molecule will not be the removed under our experimental conditions (atmospheric pressure and ambient temperature).

The adhesion between particles in powder bodies increased as a result of the capillary condensation of water from a humid atmosphere. The important of this capillary condensation to processes such as a dust suppression or the contamination of `clean` surfaces is obvious. In a humid atmosphere, any capillary condensation between particles will result in an increased attractive interaction. Depending on the geometry of interaction, the relative humidity and the strength of the surface forces, the interaction pull-off force between the two surfaces can be predicted (Fig.2.13). The capillary forces between two rigid spheres arise from the axial component of the surface tension and the capillary pressure.

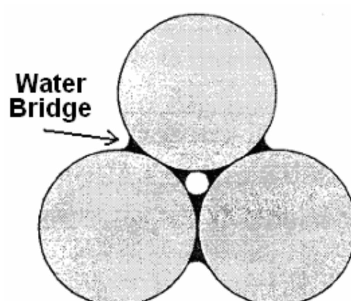

Fig.2.13 Water bridges between particles due to capillary condensation in a humid atmosphere

In presence of humidity surfaces of tip and sample absorb water molecules and become wet, if tip and sample are clean and hydrophilic. This can lead to the formation of a water bridge between them (Fig.2.14).

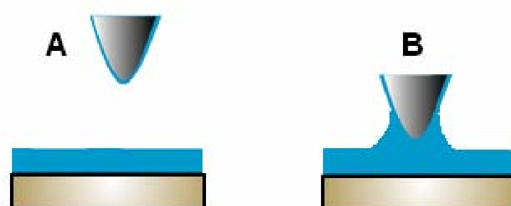

Fig.2.14 Schematic picture of formation of a water bridge during approach of hydrophilic sphere or AFM tip and a hydrophilic plane in high humidity, A) AFM probe and planar surface are still far away from each other and both surfaces are wet, B) Water bridge from between the two objects.

2.6.3. Capillary condensation

When two solid bodies are brought in sufficiently close contact to each other in ambient pressure below saturation, a phenomenon of spontaneous capillary condensation occurs followed by a liquid bridge formation around the contact area. A liquid bridge coexists in stable equilibrium with the surrounding vapor and is separated from the vapor by a concave meniscus of mean curvature defined by the Kelvin equation (Eq.2-51) [118-123] .

Capillary condensation between two solid bodies or a solid and liquid surface is of importance in many fields of science and engineering such as adhesion of particulate materials, estimation of the wetted area of packed columns, handling of fine cohesive powder materials and spreading of ink on paper, coating and paints. Also capillary condensation can be important in the adhesion of dust and powders to surfaces in semiconductor industry. Under ambient conditions such as high humidity, reduction of adhesion forces is limited by the existence of the meniscus force that arises from capillary condensation between two surfaces such as a particle and a planar surface [124]. The fundamental equation for capillary condensation is the Kelvin equation. It describes the dependence of vapor pressure of a liquid on the curvature of the liquid:

$$R_G T \ln\frac{P}{P_0} = \gamma V_m \left[\frac{1}{R_1} + \frac{1}{R_2}\right] \quad (2\text{- }51)$$

where R_G is the gas constant, T the temperature, V_m is the molar volume of the liquid, P_0 is the vapor pressure of the planar liquid, P is the vapor pressure of the liquid with the curved surface, γ is the surface tension of the liquid, R_1 and R_2 are the principal radii of curvature. A consequence of the dependence of vapor pressure on curvature is the phenomenon of capillary condensation between two objects [80].

2.7. MENISCUS FORCE

The dependence of adhesion force on relative humidity can be explained by the presence of a meniscus force, which depends on the exact geometry of the tip. Slight changes of the tip or sample shape and size can change the

meniscus force significantly. To support this hypothesis we calculated the meniscus force-versus-humidity for different geometries. We use continuum theory, although for low vapor pressures the curvatures are of atomic dimensions. As it turns out, even with this simple approach the observed phenomena can be explained. The shape of the liquid menisci (also called pendular ring liquid) is calculated with Kelvin's equation, assuming that perfect equilibrium is established between the vapor phase and the condensed liquid. This assumption is in line with an estimation of Ljunggren and Eriksson [125] and it is supported by experiments with the surface forces apparatus [126]. It is, however, contrary to what Bocquet *et al.* [127] and Riedo *et al.* [128] assumed to describe the influence of humidity on friction. Their time scale for formation and breakage of nanocontacts is, however, much faster. Typically the asperities in a friction process they study are in contact for less than 10-0.1 ms. In an AFM force experiment the contact time is typically 0.1-1 s.

I use the Kelvin equation in its most simple form, which neglects the direct effect of surface forces and assumes a constant surface tension. This is certainly a severe assumption because the relevant separations are on a 1-10 nm scale. At that scale confinement of a liquid or even the presence of a solid surface may change the effective surface tension of the liquid. For a discussion see for example refs. [129].

I proceed in four steps. First, the meniscus force for different fundamental geometries is calculated. Second, surface roughness is taken into account. As an example it is estimated for the interaction of spherical particles in a powder but in the same way it can be applied for the interaction of an AFM tip with a surface. Third, to describe the meniscus force of an AFM tip I propose a two-sphere-model and demonstrate its characteristic properties. As an alternative model I present a conical tip with a spherical end.

2.7.1. Calculation of meniscus force for fundamental geometries

In the first step we calculated the meniscus force for a sphere, a cone, and a flat cylinder in contact with a planar surface (Fig.2.15). In general the meniscus force is the sum of a capillary pressure force caused by the reduced pressure inside the meniscus and the surface tension component, which is a

direct result of the surface tension of the liquid. For a rotational symmetric geometry the meniscus force is [120] (for an overview see refs. [130], [131])

$$F_M = l^2 \pi \Delta P + 2l\pi\gamma \quad (2\text{-}52)$$

Here, l is the radial distance of the liquid meniscus (Fig.2.15) and γ = 0.072 N/m is the surface tension of water. The pressure inside the liquid is reduced with respect to the outer pressure by the Laplace pressure ΔP. To describe the shape of the meniscus I apply the toroidal (sometimes also called "circular") approximation [120],[132]. In the toroidal approximation the liquid meniscus is described by two circles, as indicated in Fig.2.15.

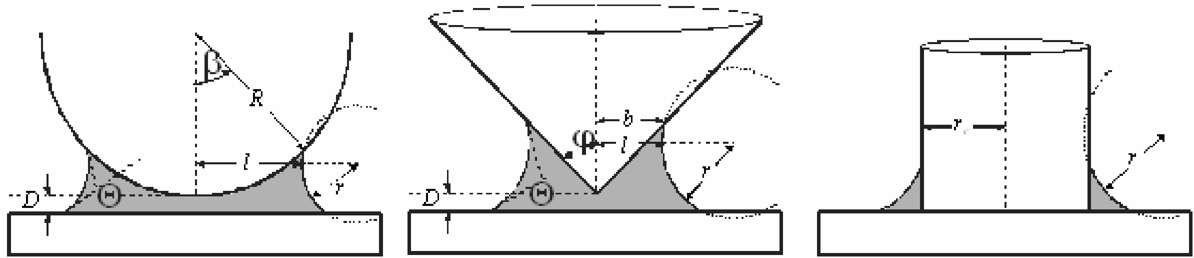

Fig.2.15 Three basic contact geometries for which the meniscus force versus humidity.

In one direction this is certainly correct because the geometry is rotational symmetric. The shape in the plane of the paper, however, is not precisely a circle but a nodoid [133]. For small menisci, where the effect of gravity can be neglected and if $1/r >> 1/l$, the toroidal approximation is applicable and deviations between forces calculated numerically with the precise shape agree with results of the toroidal approximation [134-139]. Applying the toroidal approximation the Laplace pressure is given by

$$\Delta P = \gamma\left(\frac{1}{r} - \frac{1}{l}\right) \quad (2\text{-}53)$$

where r and l describe are two principal radii of curvature. The minus sign indicates that the curvatures are opposite to each other.

The meniscus force between two spheres has been calculated numerically [136, 140-142] and with the toroidal approximation [120, 143, 144]. For a sphere of radius R which is a distance D away from a planar surface the meniscus forces is [145]

$$F_M = 2\pi\gamma R \sin\beta\left[\sin(\beta + \Theta) + \frac{R}{2}\sin\beta \cdot \left(\frac{1}{r} - \frac{1}{l}\right)\right] \quad (2\text{-}54)$$

with the two principal radii of curvature,

$$r = \frac{R \cdot (1 - \cos\beta) + D}{\cos(\beta + \Theta) + \cos\Theta} \tag{2- 55}$$

and

$$l = R\sin\beta + r[\sin(\beta + \Theta) - 1] \tag{2- 56}$$

Here, Θ is the contact angle of the liquid on the sphere and plane, which for simplicity were assumed to be equal. The angle β describes the position of the contact line of the liquid on the sphere. Practically, the parameter β was varied. For each β the values for *r, l,* F_M, and the overall curvature $(\frac{1}{r} - \frac{1}{l})$ were calculated. Using this curvature the relative vapor pressure $\frac{P}{P_0}$, with *P* being the actual vapor pressure and P_0 as the saturation vapor pressure of a reference planar liquid surface, was calculated using the Kelvin equation:

$$\frac{P}{P_0} = \exp\left[-\frac{\gamma V_m}{R_G T}\left(\frac{1}{r} - \frac{1}{l}\right)\right] \tag{2- 57}$$

R_G is the gas constant, T = 298 *K* is the temperature, and V_m = 18×10^{-6} m^3/mol is the molar volume of water. Finally F_M was plotted versus $\frac{P}{P_0}$ (Fig.2.16).

In addition to the meniscus force, other long-range forces [146], such as the van der Waals force contribute to the interaction. The van der Waals force was calculated with Derjaguin's approximation [53]. As the gap fills with condensing water the van der Waals attraction is reduced. The Hamaker constant for the interaction of a solid interacting across vacuum (or a gas) with another solid A_H^g is typically 5-10 times higher than the Hamaker constant for the interaction across liquid water A_H^l. Therefore, as water condenses into the gap the van der Waals attraction is gradually reduced [147]. For a sphere interacting with a planar surface the van der Waals attraction decreases from (e.g. ref. [74])

$$F_{vdw} = \frac{A_H^g R}{6(D + D_0)^2} \quad \text{to} \quad F_{vdw} = \frac{A_H^l R}{6(D + D_0)^2} \tag{2- 58}$$

Here, D_0 is the distance of closest approach, which is of the order of a typical

interatomic spacing. Using Derjaguin's approximation the van der Waals force for different menisci can be calculated

$$F_{vdW} = -\frac{\left(A_H^l - A_H^g\right)}{6R}\frac{d'+1-2\cos\beta}{\left(d'+1-\cos\beta\right)^2} + \frac{A_H^l}{6R}\frac{d'-1}{d'^2} - \frac{A_H^g}{6R}\frac{1}{d'+1} \tag{2- 59}$$

Here,

$$d' = (D_0 + D)/R\ . \tag{2- 60}$$

If not otherwise mentioned we used $A_H^g = 6.5\times10^{-20}$ J in air (vacuum) and $A_H^l = 10^{-20}$ J in water, which are the values for silicon oxide (ref. [75] and references therein). The interatomic spacing was set to D_0 = 0.17 nm. This value is often used in the literature [74] and it leads to a reasonable estimation of the surface energy of silicon oxide of (ref. [75], p. 92)

$$\gamma_S = \frac{A_H^g}{\left(24\pi D_0^2\right)} = 0.046\ \text{Nm}^{-1}. \tag{2- 61}$$

For a cone of half opening angle φ interacting with a smooth plane the meniscus force was calculated with [148]

$$F_M = 2b\pi\gamma\left[\cos(\varphi-\Theta) + \frac{b}{2}\cdot\left(\frac{1}{r}-\frac{1}{l}\right)\right] \tag{2- 62}$$

and the principal radii of curvature

$$r = \frac{\dfrac{b}{\tan\varphi} + D}{\sin(\varphi-\Theta)+\cos\Theta} \tag{2- 63}$$

and

$$l = b + r\left[\cos(\varphi-\Theta) - 1\right] \tag{2- 64}$$

Instead of the angle β in this case it is more convenient to use the radius of the contact line b as a parameter (Fig.2.16 middle). Practically, the parameter b was varied and for each b the values for *r, l,* F_M and $(\frac{1}{r}-\frac{1}{l})$ were calculated. In addition, the contribution of the van der Waals force was calculated according to

$$F_{vdW} = \frac{\tan^2\varphi\left(A_H^l - A_H^g\right)}{6\left(D_0+D\right)}\frac{1+\dfrac{2b}{\left(D_0+D\right)\cdot\tan\varphi}}{\left[1+\dfrac{b}{\left(D_0+D\right)\cdot\tan\varphi}\right]^2} - \frac{A_H^l\tan^2\varphi}{6\left(D_0+D\right)} \tag{2- 65}$$

For a cylinder of radius r_c with a flat end the meniscus force can directly be expressed as

$$F_M = 2r_c \pi\gamma\cos\Theta - r_c^2 \pi \frac{R_G T}{V_m}\ln\left(\frac{P}{P_0}\right) \quad (2\text{- }66)$$

and the van der Waals force is simply given by

$$F_{vdW} = \frac{r_c^2 A_H^l}{6D_0^3} \quad (2\text{- }67)$$

Here, we only consider the case of contact ($D = 0$).

AFM tips are often described as being spherical at their ends. Therefore, we start by calculating the interaction between a sphere of radius *R* = 30 nm and a planar surface (Fig.2.16Left). The meniscus force for hydrophilic surfaces is close to the limiting value given by

$$F_M \approx 4\pi\gamma R\cos\Theta\,. \quad (2\text{- }68)$$

Only at very high vapor pressures the meniscus force decreases. The vapor pressure, where the meniscus force decreases significantly is high for large radii and decreases with decreasing radius of the sphere. At a radius of 30 nm (Fig.2.16Left) this leads to a significant decrease above $\frac{P}{P_0} \approx 0.9$. The meniscus force decreases with increasing contact angle. This decrease is, however, only significant above contact angles of Θ≥ 30°.

For $\frac{P}{P_0} \to 0$, the meniscus force converges to $4\pi R\gamma\cos\Theta$. In this case, however, the results of continuum theory are not likely to describe the meniscus realistically. In case where molecular dimensions are reached, continuum theory is certainly going to fail because it predicts a condensation into gaps that are narrower than the diameter of a molecule. Assuming a molecular radius of 0.15 nm, this limit can be estimated with the Kelvin equation to be at

$\frac{P}{P_0} = \exp\left(-\gamma V_m / 0.15\text{nm} R_G T\right) = 0.03$.

At very low humidity – that is in the “dry” case - the adhesion is expected to drop to the adhesion given by the van der Waals force alone. The van der Waals force in the dry case ($\frac{P}{P_0} \to 0$) is 11.2 nN. In general, the van der

Waals force amplifies the tendency of the adhesion force to decrease with increasing humidity, assuming that the total force is the sum of both contributions.

For a cone interacting with a plane the meniscus force increases with humidity (Fig.2.16middle). The shape of the curves and the strength of the meniscus force increases drastically for flat cones with a high opening angle. For sharp cones with $\varphi \leq 40°$ the meniscus force is small. Also the van der Waals force is low. For a flat cylinder the meniscus force decreases strongly with humidity. Thus, depending on the geometry, the meniscus force increases (for a cone), decreases (for a cylinder), or is relatively constant (for a sphere).

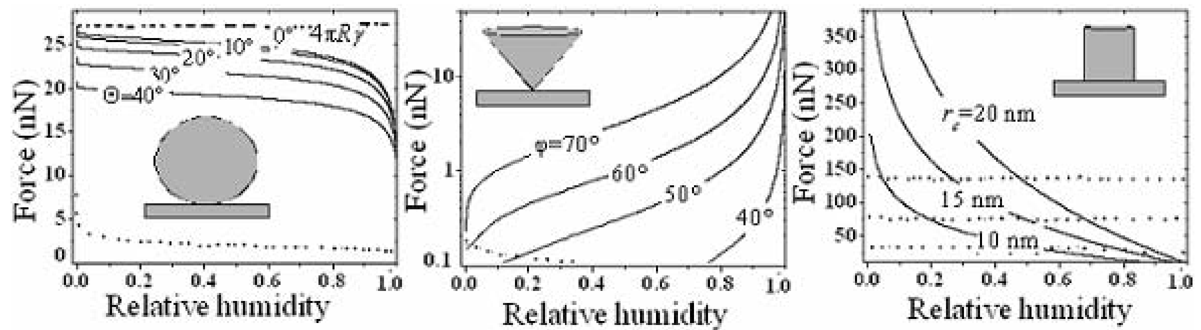

Fig.2.16 Left: meniscus force between a sphere of radius R= 30 nm and a planar surface versus humidity for different contact angle Θ (continuous lines). Meniscus force calculated with Eqs.[(2-53)-(2-57)]. The van der Waals force (dashed) was calculated with Eq. (2-59) with Hamaker constant $A_H^g = 6.5 \times 10^{-20}$ J and $A_H^l = 10^{-20}$ J. The total force was assumed to be the sum of both. Middle: meniscus force between a cone and a planar surface versus humidity for half opening angles φ of the cone 40°,50°, 60° and 70° calculated with Eqs. [(2-62)-(2-64)]. The contact angle was set to $\Theta = 10^\circ$. The van der Waals attraction was calculated with Eq. (2-65). To be able to see the whole range of force a logarithmic scale was chosen. (Right): Meniscus force-versus-humidity for a flat cylinder of radius $r_c = 10$, 15, and 20 nm in contact with a planar surface (Eq.2-66). For comparison the van der Waals attraction is shown as dashed line (Eq.2-67). In all cases the distance D was set to zero.

2.7.2. Calculation of meniscus force taking surface roughness into account

None of these basic smooth geometries showed the typical experimentally

observed dependency of the adhesion force with humidity. Therefore we take surface roughness into consideration and we show that surface roughness can explain the often observed increase of adhesion with humidity. We use the interaction of a particle with an overall spherical shape (R = 2 µm radius) with a planar surface as an example.
A first and simple way of taking surface roughness into account is to introduce an effective distance of closest approach (Fig.2.17A).

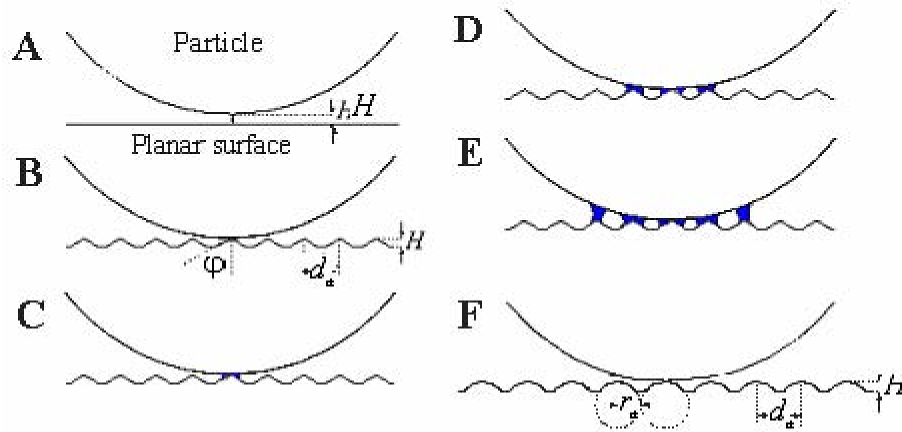

Fig.2.17 Roughness was modeled (A) by an asperity limiting the distance of closest approach to D = H; (B-E) by cones arranged in a hexagonal array with a distance of d_a, a height H and a half opening angle φ, and (F) by an array of closed-packed spheres of radius r_a sticking out a distance H of an otherwise planar surface . For the conical asperities different stages of capillary condensation are shown.

Asperities on the surface or confined adsorbed hydrophobic molecules, for example contamination, could prevent the particle to get in close contact so that asperities effectively create a gap between the plane and the particle. We denote the height of the asperity by *H*. The asperity effectively adds a certain distance $D = H$ in Eq. (2-55). This changes the meniscus force-versus-humidity curve drastically (Fig.2.18). It is zero at low humidity. From a certain critical vapor pressure on it increases, reaches a maximum, and decreases again at very high humidity. The critical vapor pressure is given by the Kelvin equation [149]

$$\left(\frac{P}{P_0}\right)_C \approx \exp\left(-\frac{2\gamma V_m \cos\Theta}{R_G T H}\right) \qquad \text{(2- 69)}$$

where *H* is the distance of closest approach. In Eq. (2-69) I assumed that

$r = \frac{H}{(2\cos\Theta)} \prec\prec l$. For H = 0.5, 1.0, 1.5, and 2.0 nm the critical relative vapor pressures are 0.128, 0.357, 0.503 and 0.597, respectively. For a smooth particle and a smooth planar surface the meniscus force and the van der Waals attraction are displayed for comparison. The van der Waals force (dashed line) is only important at low humidity. In the limit $\frac{P}{P_0} \to 0$ the van der Waals attraction reaches 715 nN. In a second step, we introduced more realistic asperities, such as conical (Fig.2.17B) or spherical asperities (Fig.2.17F) on the planar surface. Whether roughness is introduced on the planar surface or the particle surface does not change anything. The asperities were distributed in a hexagonal pattern with a spacing d_a, and a height *H*.

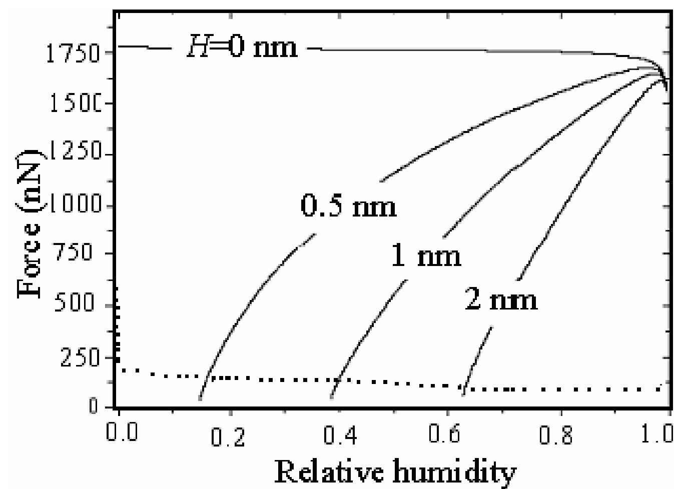

Fig.2.18 Meniscus force between a sphere of radius R = 2 μm and a planar surface versus humidity for different H of closest approach (continuous lines). Meniscus forces were calculated with Eqs. [(2-54)-(2-56)], setting D = H. The van der Waals force (dashed line) was calculated with Eq. (2-59) for D_0 = 0.17 nm and without an additional asperity. The contact angle was set to $\Theta = 10^\circ$.

The particle is approaching directly on one asperity. Conical asperities are further characterized by the half opening angle φ, spherical asperities by their radius r_a. The effect of surface roughness as simulated by surface asperities is to cause a more gradual increase of the meniscus force at low humidity. As an example, I calculated the case of a spherical particle interacting with a

planar surface which is covered by conical asperities of H = 2 nm height, a spacing of $d_a = 20nm$ and an opening angle of φ = 70° (Fig.2.19).

At low humidity the meniscus force is given by the contact of the central asperity with the particle (Fig.2.17C). Once the humidity reaches a value of $\frac{P}{P_0}$ = 0.0837 the closest ring of six asperities starts to contribute (Fig.2.17D). The second ring of six asperities contributes from $\frac{P}{P_0}$ = 0.4374 on (Fig.2.17E), the third ring of asperities starts at $\frac{P}{P_0}$ = 0.5379. At $\frac{P}{P_0}$ = 0.6248 the whole gap fills with condensed water and the meniscus force is now similar to the meniscus force of a sphere of 2 µm radius at a distance of 2 nm.
Qualitatively the same behavior is observed when spherical rather than conical asperities were considered. In the example (Fig.2.19) the spacing was kept at $d_a = 20nm$ and the radius of the asperities was set to r_a = *10 nm*. For spherical asperities five rings contribute before the whole gap is filled. The first, second, third etc. ring start to contribute at a relative humidity of $\frac{P}{P_0}$ = 0.0003, 0.0985, 0.1928, 0.3873, and 0.5547, respectively.

In the two above calculations the asperities were assumed to be infinitely hard. In reality, the attractive meniscus force, the van der Waals force, and the applied load lead to a deformation. To estimate the effect of deformation we used a surface roughness modeled by spherical asperities. The Hertz theory can be used to calculate the deformation induced by the attractive forces. We proceeded as follows. First, the meniscus force and the van der Waals force were calculated for the inner asperity assuming it is infinitely hard. Then the indentation of the inner asperity expected at a load given by the meniscus force was calculated using Hertz theory according to [6]

$$\delta = \frac{1}{4}\left[\frac{9F^2\left(1-\nu^2\right)^2}{r_a E^2}\right]^{1/3} \qquad (2\text{- }70)$$

Here, F is the meniscus force plus the van der Waals force. We used a Young's modulus of E = 73 *GPa* and a Poisson ratio of ν = 0.17 for silica. Indentation increases the meniscus force. This was taken into account by

introducing a negative distance $D=-\delta$ into Eq. (2-55). With this value a new meniscus force was calculated, inserted into Eqs.[(2-54)-(2-56)], and so on. It turns out that the indentation causes also the first ring of six asperities to come into contact at $\frac{P}{P_0}\rightarrow 0$. For this reason we repeated the cycle taking also the first ring of asperities into account. Finally it turned out that for $\frac{P}{P_0}\rightarrow 0$ the indentation of the inner asperity is 0.23 nm. The second, third, fourth and fifth ring start to be filled with condensing water at $\frac{P}{P_0}$ = 0.00012, 0.0136, 0.1928, and 0.4233, respectively.

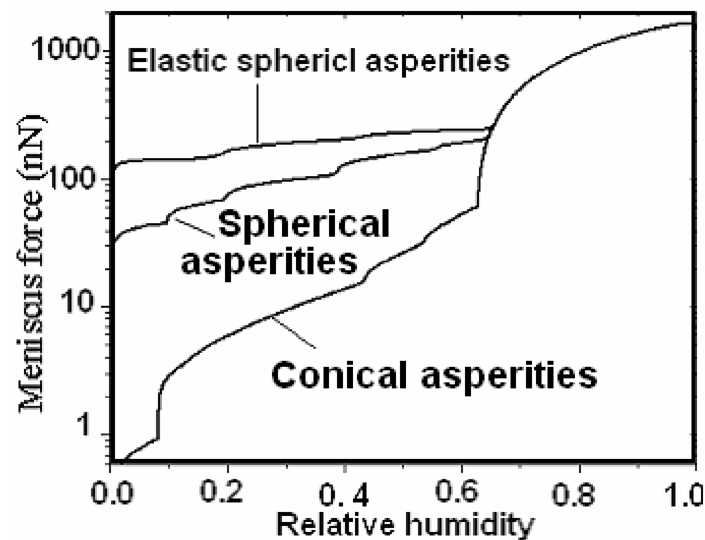

Fig.2.19 Meniscus force between a smooth sphere of R = 2 μm radius with a surface covered with 2 nm high asperities. The asperities were arranged in a hexagonal two-dimensional array with a spacing $a = 20nm$. Three cases were considered: Conical asperities with a half opening angle of $\varphi = 70^\circ$, spherical caps with a radius $r_a = 10nm$, and spherical caps which are elastically compressed according to Hertz theory Eq. (2-70). The particle is positioned directly on top of a “central” asperity. The contact angle of all surfaces was set to $\Theta = 10^\circ$.

2.7.3. A two-sphere-model to describe the meniscus force of an AFM tip

Most SEM image of AFM tips indicate that the end of the tip can be described by a two-sphere-model (Fig.2.20). In this model the tip consists of two spheres, sphere 1 and sphere 2, of radius R_1 and R_2. Sphere 1 describes

the very end of the tip. For “blunt” tips with a high aspect ratio $R_1 > R_2$. “Sharp” tips are described by $R_1 < R_2$. To take roughness in the nano- and subnanometer scale into account an asperity of height *H* is assumed to limit the distance of closest approach. To describe the humidity dependence of the meniscus we distinguish three regimes (Fig.2.21).

Fig.2.20 Schematic of two-sphere-model for the tip shape, Roughness is taken into account by introducing an asperity.

For low humidity the meniscus is identical to that of a sphere of radius R_1 at a distance *H*. It can be calculated with Eqs. [(2-54)-(2-56)] and the appropriate parameter to describe the meniscus is the angle β. It ranges from zero to α_1 ($0 \le \beta \le \alpha_1$). Equations [(2-54)-(2-56)] are valid until the meniscus has reached the contact line of the two spheres. This is the case when $\beta = \alpha_1$ and the meniscus assumes a radius $a = R_1 \sin\alpha_1$.

Fig.2.21 Schematic of one half of blunt tip represented by the two-sphere-model, showing the increase of the meniscus with increasing humidity

For high humidity, the meniscus force is determined by sphere 2, and, again, Eqs. [(2-54)-(2-56)] can be used with R_2 as the radius. The minimal value of

the parameter β is given by $a = R_1 \sin\alpha_1 = R_2 \sin\alpha_2$, and it starts at $\beta = \alpha_2 = \arcsin(\frac{R_1 \sin\alpha_1}{R_2})$.

For blunt tips ($R_1 > R_2$) I have to consider an intermediate range in which the meniscus is pinned at the edge. This implies that l remains constant at $l = a$ and that r increases from

$$r = \frac{R_1(1-\cos\alpha_1)+H}{\cos(\alpha_1+\Theta)+\cos\Theta} \tag{2- 71}$$

to

$$r = \frac{R_2(1-\cos\alpha_2)+H-R_1(1-\cos\alpha_1)}{\cos(\alpha_2+\Theta)+\cos\Theta} \tag{2-72}$$

The meniscus force in this regime can directly be calculated from

$$F_M = 2\pi a\gamma + 2\pi r\gamma - \pi a^2 \frac{RT}{V_m}\ln\left(\frac{P}{P_0}\right) \tag{2- 73}$$

It decreases with increasing vapor pressure because the Laplace pressure in the meniscus decreases while the circumference remains constant.
The van der Waals force is approximately determined by sphere 1:

$$F_{vdW} = \frac{\left(A_H^g - A_H^l\right)}{6R_1}\frac{d'+1-2\cos\beta}{\left(d'+1-\cos\beta\right)^2} + \frac{A_H^l}{6R_1}\frac{d'-1}{d'^2} - \frac{A_H^g}{6R_1}\frac{d'+1-2\cos\alpha_1}{\left(d'+1-\cos\alpha_1\right)^2} \tag{2- 74}$$

For most practical cases $D_0 + H + R_1(1-\cos\alpha_1)$ is several nanometers, so that the contribution of sphere 2 is usually small and can be neglected.

Using the two-sphere-model, characteristic features of the meniscus force versus humidity can be reproduced. The initial increase in the meniscus force is caused by sphere 1 and taking roughness into account. In Fig.2.22, I calculated the meniscus force for R_1 = 100 nm and H = 0.17 nm. At a radius of a = 12 nm (and 20 nm) sphere 2 starts to describe the tip shape. The meniscus has reached this radius at a relative humidity of 0.325 (0.64). Depending on R_2, the meniscus force continuous to increase with humidity or it starts to decrease. If sphere 1 is larger than sphere 2, the meniscus force decreases at high humidity and a maximum is observed. If sphere 1 is smaller than sphere 2, the meniscus force increases at high humidity. This can lead to a continuous increase of the meniscus force till very high humidity.

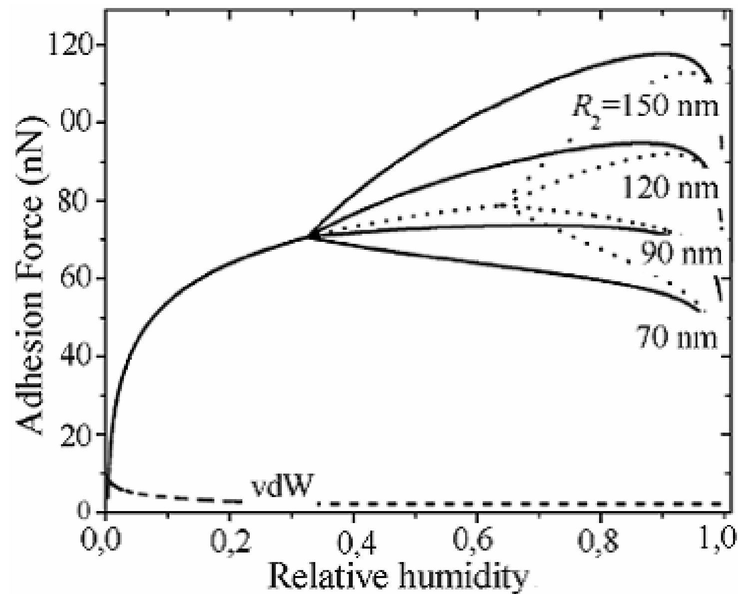

Fig.2.22 Meniscus force-versus-humidity calculated with the two-sphere-model. R_1 = 100 nm was kept constant while R_2 was varied between 70 and 150 nm. Continuous lines were calculated with $a = 12nm$, dotted line were obtained with $a = 20nm$. Surface roughness was considered by introducing the distance of closest approach to be H = 0.17 nm. All surfaces were assumed to be completely wetting ($\Theta = 0$). The van der Waals force (dashed) was calculated with Eq. (2-62) with $A_H^g = 6.5 \times 10^{-20}$ J, $A_H^l = 10^{-20}$ J, $D_0 = 0.17nm$, and $D = H = 0.17nm$.

2.7.4. Alternative model: Meniscus force for conical tip with a spherical end

As an alternative, I calculated the expected meniscus and van der Waals forces for a cone with a spherical end (Fig.2.23). Sharp tips are described by a small radius of curvature *R*, a smooth transition between spherical and conical part ($90° - \alpha = \varphi$), and a small opening angle φ. Blunt tips are described by a large radius of curvature and usually a sharp transition between spherical and conical part ($90° - \alpha > \varphi$). To take roughness into account an asperity of height *H* was assumed to limit the distance of closest approach. To describe the humidity dependence of the meniscus we distinguish three regimes:

For low humidity the meniscus is identical to that of a sphere at a distance *H*. It can be calculated with Eqs. [(2-54)-(2-56)] and the appropriate parameter to describe the meniscus is the angle β. Equations [(2-54)-(2-56)] are valid

until the meniscus has reached the edge of the spherical part. This is the case when $\beta = \alpha$ and the meniscus assumes a radius $a = R\sin\alpha$. The van der Waals force in this regime is given by

$$F_{vdW} = \frac{\left(A_H^g - A_H^l\right)}{6R}\frac{d'+1-2\cos\beta}{\left(d'+1-\cos\beta\right)^2} + \frac{A_H^l}{6R}\frac{d'-1}{d'^2} - \frac{A_H^g}{6R}\frac{d'+1-2\cos\alpha}{\left(d'+1-\cos\alpha\right)^2} + \frac{A_H^g \tan^2\varphi}{6\left(D_0 + H + R(1-\cos\alpha)\right)}\left[1 + \frac{a}{\left(D_0 + H + R(1-\cos\alpha)\right)\tan\varphi}\right]. \quad (2\text{- }75)$$

For most practical cases $D_0 + H + R(1-\cos\alpha)$ is several nanometers so that the contribution of the conical part is usually small. It can be neglected by ignoring the last term in Eq. (2-75).

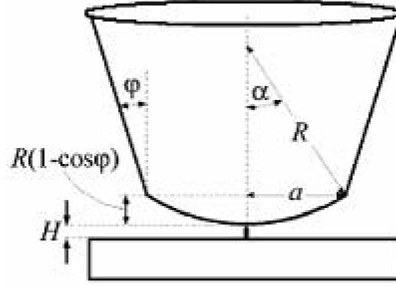

Fig.2.23 Schematic of a cone with a spherical end. This geometry was used model the shape of AFM tips.

When, at intermediate humidity, the meniscus reaches the end of the spherical part, I have to distinguish between a smooth transition ($90° - \alpha = \varphi$) and a sharp transition ($90° - \alpha > \varphi$). For a smooth transition, immediately the third regime, that of the conical part, is entered. For a sharp transition the meniscus is pinned at the edge. This implies that *l* remains constant at $l = a$ and that *r* increases from

$$r = \frac{R(1-\cos\alpha) + H}{\cos(\alpha + \Theta) + \cos\Theta} \quad (2\text{- }76)$$

to

$$H + R(1-\cos\varphi) = r\left[\cos\Theta + \sin(\varphi - \Theta)\right] \Rightarrow r = \frac{R(1-\cos\varphi) + H}{\sin(\varphi - \Theta) + \cos\Theta} \quad (2\text{- }77)$$

The meniscus force in this regime can directly be calculated from Eq. (2-73). It decreases with increasing vapor pressure because the Laplace pressure in the meniscus decreases while the circumference remains constant. The van der Waals force in the intermediate regime remains constant.

For high humidity the meniscus force is determined by the conical part of the tip. I can use Eqs.(2-62)-(2-64) with the effective distance $D = H + R(1-\cos\alpha) - a/\tan\varphi$. Please note that this distance can be negative for bunt tips. The parameter describing the size of the meniscus is *b*, with $b \geq a$. For the van der Waals force we used the expression

$$F_{vdW} = \frac{A_H^l}{6R}\frac{d'-1}{d'^2} - \frac{A_H^l}{6R}\frac{d'+1-2\cos\alpha}{(d'+1-\cos\alpha)^2} + \frac{A_H^g \tan^2\varphi}{6(D_0 + H + R(1-\cos\alpha))} \times \left[1 + \frac{a}{(D_0 + H + R(1-\cos\alpha))\tan\varphi}\right] \quad \text{(2- 78)}$$

thus neglecting the explicit dependence of the change in van der Waals force, when the meniscus reaches the conical part. Practically this contribution is small.

Like the two-sphere model the conical tip with a spherical end showed an increasing meniscus force with increasing humidity (Fig.2.24). We first consider tips with a smooth transition between the spherical and conical part. As an example, meniscus force-versus-humidity-curves are shown for a tip with *R* = 40 nm. Up to a relatively high humidity the spherical part dominates the adhesion force. The conical part is only important at very high humidity. The transition depends on the opening angle and is at a relative humidity of 0.70, 0.86, 0.93, and 0.96 for φ = 70°, 60°, 50°, and 40°, respectively.

As an example for a blunt tip we calculated the meniscus force versus humidity for *R*=100 nm, a = 15 nm and φ = 50°. The spherical part with the surface roughness considered by H = 0.17 nm dominates up to a humidity of 0.47. Then the three-phase contact line is pinned on the tip surface. In this intermediate regime the meniscus force decreases. This is indicated by arrows in Fig.2.24. At humidity above 0.51 the conical part determines the meniscus force. In contrast to the previous example (Fig.2.16middle) the meniscus force continues to decrease because effectively we deal with a truncated cone. Only at very high humidity ($\frac{P}{P_0} \geq 0.94$) does the meniscus force increases as expected for a conical tip.

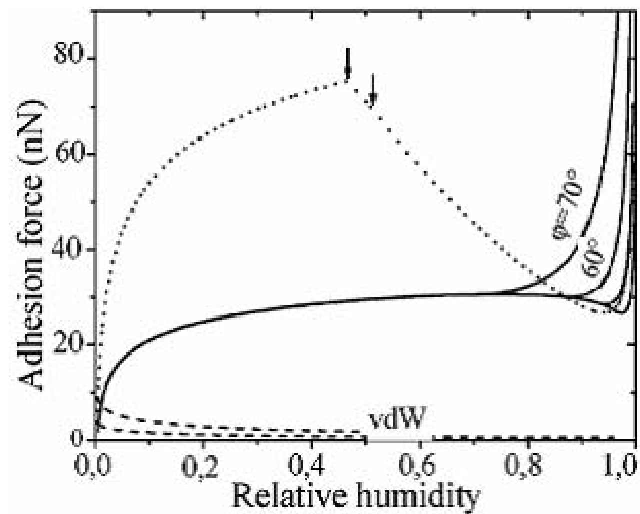

Fig.2.24 Meniscus force versus humidity calculated for a cone with a spherical end. Continuous lines were calculated for R =40 nm and a smooth transition between the spherical and conical part. From left to right the curve correspond to a half opening angle φ of 70°, 60°, 50°, and 40°. For a blunt tip with R = 100 nm, $a = 15nm$, and $\varphi = 50°$ the results are shown as a dotted line. The arrows indicate the transition between the spherical, intermediate, and conical parts. Roughness was taken into account by setting the distance of closest approach to H = 0.17 nm. All surfaces were assumed to be completely wetting ($\Theta = 0$). For comparison also the van der Waals attraction is shown for the sharp tip bottom dashed curve (R = 40 nm) and the blunt tip (top dashed curve, R = 100 nm).

3. MATERIAL AND METHODS

3.1. ATOMIC FORCE MICROSCOPY

In 1980/81 G. Binnig, H. Rohrer, and coworkers from the IBM Zurich Research Laboratories invented a new type of microscope [150], [21, 151] (Binnig *et al*., 1982) which they called the Scanning Tunneling Microscope (STM). The instrument, which proved capable of imaging solid surfaces with atomic resolution, has revolutionized microscopy and surface analysis in an unprecedented way over 20 years. When looking back it is evident that the outstanding success of STM is not only due to the ultrahigh resolution which can be achieved by this technique. Equally important, if not more, is that STM stimulated the development of a whole family of Scanning Probe Microscopy (SPM) which is all based on instrumental principles very similar to that of the STM. The most popular off spring is Atomic Force Microscopy [21] (AFM). STM and AFM today represent a set of microcopies which can be applied in many different and highly dedicated modes of operation, such that a variety of physical and chemical properties of a material becomes accessible. This versatility of SPM in general is, apart from the inherent high resolution, a major strength.

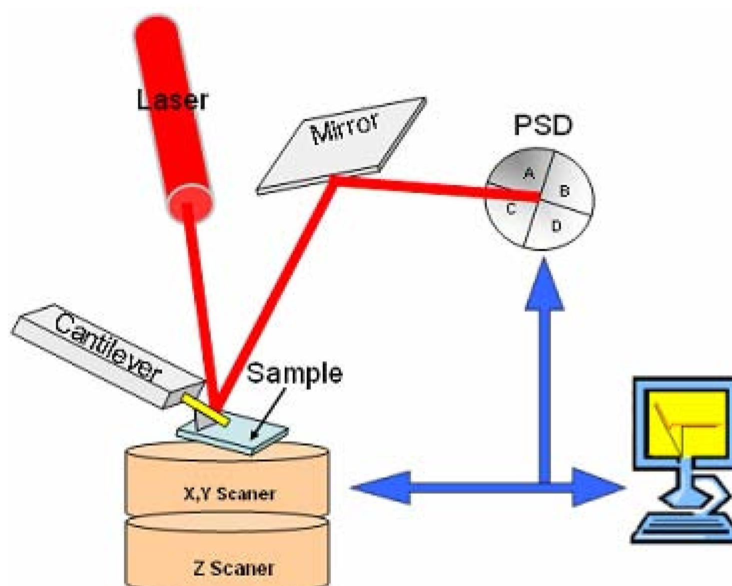

Fig.3.1 AFM schematic

Often AFMs use piezotubes sectioned into four quadrants for the movement of the sample. The piezoelectric material of the tube expands preferentially

with the application of a potential bias between the appropriate electrodes and ground: one volt potential gives ~ 10 A° displacement for the usual ceramics. The piezotube can move in the X or Y direction by exciting opposing quadrants to accomplish scanning of an area while a feedback loop controls piezo extension in the Z direction to regulate tip-sample separation.

The AFM probe consists of a base part that simply serves as a handle and a small microfabricated cantilever with a very sharp tip on its end (Fig.3.2). The magnitudes of probe mass and dimension are small enough that the weak surface interactions become dominant and, therefore, accessible for scrutiny. Typical radii of curvature for AFM tips are 10-100 nm. The tips have a high aspect ratios (tip height typically 1-3 µm). The force sensitivity of the cantilever of 10^{-7} to 10^{-11} N allow the measurement of a single, chemical bond-breaking force.

Surface topography or forces acting between tip and surface can be deduced from the cantilever deflection, which is detected by reflecting a laser beam from the backside of the cantilever onto a split photo-diode which acts as detector. When the cantilever deflects the laser spot moves on the detector and leads to a change in the detector output signal. In some cases the backside of the cantilever is coated with a metal layer like gold or aluminum to increase the reflectivity.

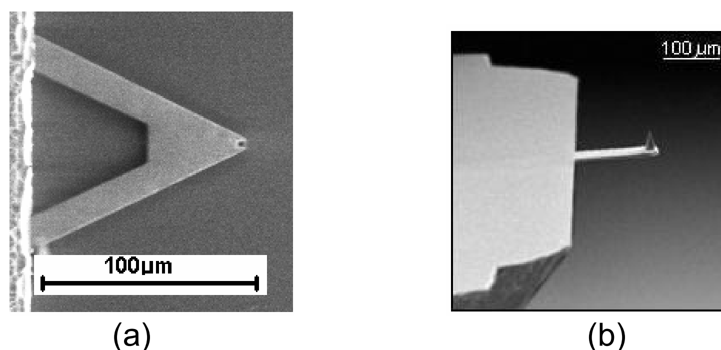

Fig.3.2 Examples of AFM cantilevers, (a) triangular and (b) rectangular

In this study surface forces were measured with two commercial AFMs, Nanowizard (JPK) Germany, and Multimode III, Veeco, Santa Barbara, USA. To measure adhesion force on flat surfaces (silicon wafer, mica) and spherical surfaces (Iron and glass particle), I used the JPK and to measure adhesion force for different humidity I used the Multimode III.

3.1.1. AFM Imaging

The three main imaging operating modes of the AFM are distinguished depending on the interaction between tip and sample surface.

a) Contact Mode (CM)

The contact mode where the tip scans the sample in close contact with the surface is the most common mode used in AFM. The repulsive contact force between tip and surface is typically set to a mean value of 10^{-9} N. This force is set by pushing the cantilever up to a deflection against the sample surface with the piezotranslator. In contact mode AFM the deflection of the cantilever is sensed and compared in a DC feedback amplifier to some desired value of deflection. The voltage that the feedback amplifier applies to the piezotranslator is a measure of the height of features on the sample surface. It is displayed as a function of the lateral position of the sample.

Advantages:

I) High scan speed.

II) Rough samples with extreme change in topography can sometimes be scanned more easily.

Disadvantage:

The high lateral (shear) and normal forces can damage soft samples (i.e. polymers or biological samples).

b) Intermittent Contact Mode (Tapping Mode)

Tapping mode is a key advance in AFM. This potent technique allows high resolution topographic imaging of sample surfaces that are easily damaged, loosely hold to their substrate, or difficult to image by other AFM techniques. Tapping mode overcomes problems associated with friction, adhesion, electrostatic forces, and other difficulties that an plague conventional AFM scanning methods.

Tapping mode imaging is implemented by oscillating the cantilever at or slightly below its resonance frequency (50 kHz to 500 kHz) using a small piezoelectric crystal. The piezo motion causes the cantilever to oscillate with an amplitude of typically 20 to 100 nm when the tip is not in contact with

surface. The oscillating tip is then moved towards the surface until it begins to lightly touch, or tap the surface. As the oscillating cantilever begins to intermittently contact the surface, the cantilever oscillation is necessarily reduced due to energy loss caused by the tip contacting the surface. The reduction in oscillation amplitude is used to identify and measure surface features. During tapping mode operation, the cantilever oscillation amplitude is maintained constant by a feedback loop.

Advantages:

I) High lateral resolution (less than 1 nm)

II) Imaging condition more stable than in NonContact Mode (NCM).

Disadvantage:

I) Lower scan speed than contact mode.

II) Higher normal forces than NCM (see below).

C) Non Contact Mode (NCM)

Similar to the intermittent contact mode the cantilever is oscillated slightly above its resonance frequency with small oscillation amplitude (< 10 nm). The tip is approached to the surface very slowly. As soon as the tip is close enough to feel attractive surface forces like the van der Waals force, this will lead to an increase in effective spring constant (sum of cantilever spring constant and gradient of attractive potential) and thus to an increase of the resonant frequency. Therefore, the oscillation amplitude induced by the excitation slightly above the resonant frequency will increase. Again a feedback loop is used to keep the average tip-sample distance at a value that leads to a stable oscillation amplitude.

Advantages:

I) Lower lateral resolution (1 to 5 nm)

II) Lower lateral and normal forces and less damage to soft samples.

Disadvantage

I) Lower scan speed than contact mode.

II) Quite instable imaging conditions.

3.1.2. AFM Force Spectroscopy

The AFM can also be used to measure force-versus-distance curves. Force-versus-distance curves provide valuable information on local material properties such as the elasticity, the Hamaker constant, adhesion, surface charge densities, the stability of molecularly thin films, etc. Another application is the analysis of surface force per se. Force measurements on single molecules involving the rupture of single chemical bonds and stretching of polymer chains has almost become routine. Furthermore, AFM is of great importance for the study comparatives of surface interaction between particles from theoretical point of view and apply view. The AFM can be fitted with liquid cell under ambient or purged atmospheres (i.e. N_2 or Ar) for solid/ liquid, liquid/liquid, or liquid/gas operations [124]. The AFM is not the only device to measure forces between solid surfaces. During the last decades several AFM techniques such as colloidal probe and devices have been developed [152-154] same SFA and so on.

Information about sample is available from measuring the changes reflect of laser point on photodiode while the separation from the surface of sample is varied at a single point, rather than by scanning the lateral position of the tip. In force spectroscopy the base of the cantilever or sample is moved in the vertical direction towards the surface using the piezo translator and then retracted again. During the motion, the deflection of the cantilever can be measured. The AFM tip is able to probe an extremely small interaction area because tip radius is between 10 to 100 nm, and this gives it is very small forces. The data from an experiment is often displayed as a simple X-Y plot (Fig. 3.3.a).

a) Anatomy of a force curve

A typical force curve is characterized by a zero line and a contact line (Fig.3.3b). In the approaching region, when tip and sample are still far away from each other, the cantilever is at the equilibrium position and the detected force is zero (zero line).

A) The cantilever starts to get close to the surface but is still not touching. In this region, the cantilever will start to deflect due to surface forces either

towards the surface (attractive forces) or away from the surface (repulsive forces.

B) As the probe tip is brought very close to the surface, often the gradient of attractive force between tip and surface becomes larger than the spring constant then. This leads to an instability and the tip will jump into contact with the surface (snap-in).

C) Once the tip is in contact with the surface, cantilever deflection will increase as the fixed end of the cantilever is brought closer to the sample. If the cantilever is sufficiently stiff, the probe tip may indent into the surface at this point. In this case, the slope or shape of the contact part of the force curve can provide information about the elasticity or plasticity of the sample surface.

D) After loading the cantilever to a desired maximum force value, the movement is reversed. As the cantilever is withdrawn, adhesion or bonds formed during contact with the surface may cause the cantilever to adhere to the sample some distance past the initial contact point of the approach curve (b).

E) A key measurement of the AFM force curve is the point at which the adhesion is broken and the cantilever comes free from the surface. This can be used to measure the rupture or adhesion force required to break the bond or adhesion (snap-out).

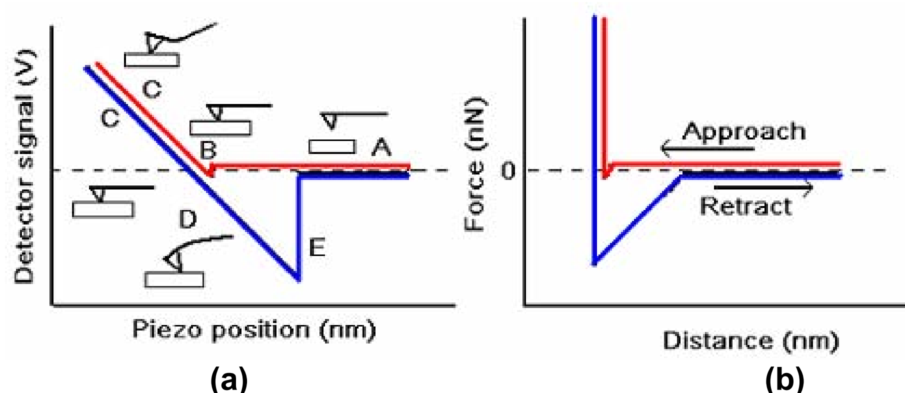

Fig.3.3 a) Cantilever deflection versus Piezo position curve (b) Force-versus-distance curve.

The result of such a measurement is a curve, which shows the cantilever deflection versus the height position of the piezo (Fig.3.3a). From this, a force-versus-distance curve (Fig.3.3b), briefly called “force curves“, is calculated by

multiplying the cantilever deflection from the height position to obtain the distance.

b) Force Volume Mode (FV) and Adhesion Force Maps

In the so-called Force Volume (FV) mode, force curves with a defined load are taken automatically within a square grid of 32×32 or 64×64 points and stored within one file. I usually took AFM images of the measurement area of typically 500 nm $\times$ 500 nm before and after the force measurement, to check whether the surface roughness changed during the force volume measurement. Force curves were typically taken with a frequency of 1.0-3.5 Hz.

A home-made analysis program was used to evaluate the huge number of force curves (typically 1024 or 4096) efficiently and extract the adhesion force. Adhesion forces were determined in the following way:

(1) From the non-contact part the force-versus-piezo position curve (force curve), the zero force line is derived by fitting it with a straight line.

(2) The contact part of the force curves is also fitted by a straight line.

(3) The position of the jump-out of contact is determined. The difference in force of the contact and non-contact straight lines at the jump-out point is taken as the adhesion force.

Adhesion forces were plotted in histogram. The mean adhesion force $\overline{F}$ and the "relative width" $\frac{\Delta F}{\overline{F}}$ was determined, where the variance ΔF is

$$\sqrt{\frac{1}{N} \cdot \sum_{i=1}^{N} (F_i - \overline{F})^2} \quad , \qquad (3\text{-}1)$$

with N being the number of force curves taken and F_i are the individual adhesion forces. Typically number of force curves was 1024 or 4096.

A simple force curve records the force felt by the tip as it approaches and retracts from a point on the sample surface. A force volume (FV mode) contains array of force curves over the entire sample area and is generated by ramping the Z piezo as the tip scans across the area. Each force curves is measured at a unique *X-Y* position in the area, and force curves from an array of *X-Y* points are combined into a three-dimensional array, or "volume," on

force data (Fig.3.4). When the tip comes into contact with the surface during a force curve, the point of contact provides the topography of the sample at that *X*-*Y* position. The Force Volume mode allows investigation of the spatial distribution of any force between tip and sample that varies with the distance between the two. Since force is the derivative of energy with respect to distance, the Force Volume data can be used to infer the potential energy between surfaces.

Adhesion maps can be used to investigate the distribution of hydrophilic and hydrophobic regions on a surface which would differ in amount of hydration and therefore, adhesion.

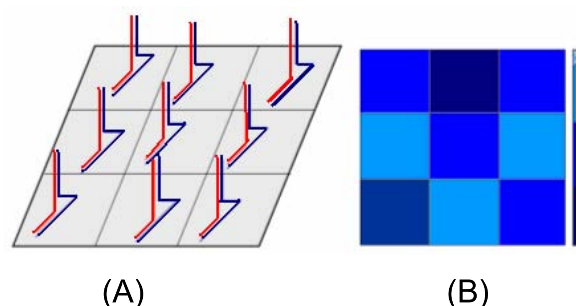

(A) (B)

Fig.3.4 A: A force volume data set- an array of regular spaced force curves yields three-dimensional-information. B: Adhesion force map of surface (A).

To investigate the mechanical, chemical, and physical properties of the surface at various locations, FV imagines consisting of array of 32 × 32 or 64 × 64 force curves were recorded in parallel with topographic images on different samples [155-158]. For each force curve, the maximum vertical displacement, *Z*, was controlled to obtain the same maximum vertical deflection, and thus the same maximum applied force for all force curves.

3.2. CANTILEVER AND SPRING CONSTANT

The AFM has the potential to give quantitative information about local interactions. Imaging and force measurements taken by an AFM depend greatly on the properties of cantilever and tip used to probe the samples surface. The quality of such measurements depends upon knowledge of the physical properties of the spring constant and tip that probe the forces. Fig.3.2 shows that two shapes of cantilever. Fig.3.5 shows schematic of a cantilever.

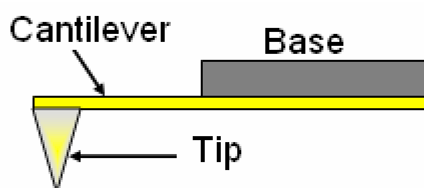

Fig.3.5 Schematic of a cantilever

The cantilever itself is usually either rectangular or triangular in shape, such as in Fig.3.6. The tip is typically be shaped like a pyramid or a cone shaped.

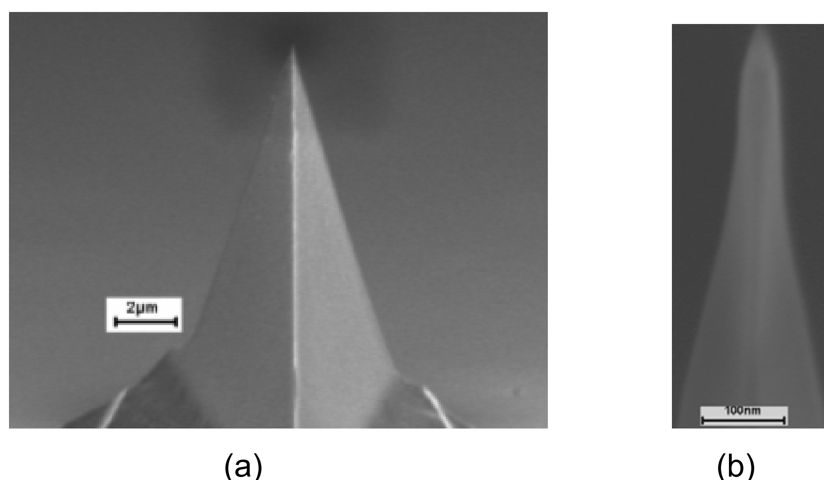

Fig.3.6 SEM images of tips. (a) Pyramid (cantilever No. 2) and (b) sharp tip (cantilever No. 5).

Many types of cantilevers and tips are available commercially. The selection of the cantilever will depend on the imaging modes. In contact mode, the deflection of the cantilever is controlled as the tip is scanned over the surface. A softer cantilever means that a lower force can be used to give the same amount of deflection. Often lower forces give better imaging, so the softest cantilevers are generally used for contact mode imaging. For this purpose, cantilevers are available with spring constant below 0.5 N/m.

The resonant frequency of the cantilever depends on its mass and spring constant, stiffer cantilevers have higher resonant frequencies. Stiffer cantilevers are usually used for intermittent contact mode, particularly in air. These generally have a resonant frequency above 100 kHz, and spring constant of more than 10 $\frac{N}{m}$. As there can be very low average deflection values during careful imaging, the stiffer cantilevers do not necessarily damage the surface. For intermittent contact mode in liquid, the capillary force is not a problem, and softer cantilevers are often used.

During this study different cantilever types were used (Table 2): (1) V-shaped silicon nitride ($Si_3 N_4$) with an integrated that was ultrasharp and tip radius of $R \leq 10$ nm from MTD Ltd. Russia; (2) rectangular silicon cantilevers with an integrated tip of $R \leq 20$ nm curvature from CONT-W, Nanoworld, Switzerland; (3) a nanocontact rectangular cantilever tipless from NSC12, MicroMash, Tallin, Estonia; (4) a V-shaped silicon nitride ($Si_3 N_4$) cantilevers tipless from Veeco, Santa Barbara, USA; (5) V-shaped with an integrated tip of $R \approx 50$ nm radius of curvature from Veeco, Santa Barbara, USA; (6) rectangular tapping mode silicon cantilevers with an integrated tip of $R \leq 20$ nm radius of tip curvature from OMCLAC 240 TN, Olympus, Japan. For cantilevers (4) and (2) the spring constant for each individual spring was experimentally determined by the thermal noise method (see 3.2.1.2).

Table 2

Type		L (μm)	w (μm)	t_c (μm)	k_c (N/m)	R (nm)
1	Si_3N_4, int. tip MTD	110	40	1.0	2.4-4.4	≤ 10
2	Silicon int. tip CONT-W	450	50	2.0	0.14-0.20	≤ 20
3	Silicon without tip, NCS12	90	35	2.3	19.0-27.0	-
4	Si_3N_4 without tip, Veeco	115	20	0.6	0.23-0.41	-
5	Si_3N_4 int. tip	115	17	0.6	0.19-0.35	≈ 50
6	Silicon int. tip Olympus	240	30	2.7	1.4-2.0	≤ 10

Table 2: Six types of cantilevers I used. Spring constants were calculated according to $k_c = Ewt_c^3 / (4L^3)$ for rectangular cantilevers (2, 3) with a Young's modulus of E= 130-185 GPa (silicon). Here, L is the length, w the width, and t_c is the thickness. For V-shaped silicon nitride cantilevers the spring constant was calculated from $k_c = Ewt_c^3 / (2L^3)$, where w is the width of one arm and E=160-290 GPa (silicon nitride). For the Young's module ranges are

given due to unknown crystallographic orientations or, in the case of silicon nitride, unknown composition (e.g. ref.[159]).

Before each measurement the cantilever with tips or particles were cleaned with a plasma cleaner. I took scanning electron microscopy images of cantilever tips before and after measurement. The scanning electron microscopy (SEM) images were obtained with field emission SEM (LEO 1530 Gemini) under 3 kV accelerating voltage. Due to the low voltage it was not necessary to coat the sample with a conducting layer.

3. 2.1. Cantilever calibration methods

Determination of the spring constant of atomic force microscopy cantilever is fundamental importance to user of the AFM. Most users of AFM didn't measure spring constant of cantilever because the spring constant of a cantilever can be estimated from its geometry and the properties of the material it is made from. There are currently many methods available for the determination of the spring constant of AFM cantilever. The mechanical properties and characterizes of cantilever are very important, because we can calculate spring constant of cantilever with Eq.3.2 (rectangular cross section) [160-163]

$$K = \frac{EWt^3}{4L^3} \quad . \tag{3-2}$$

Here, E is elastic modulus, w is width, t is thickness, and L is length in Fig.3.7. The cantilevers are available in a range of force constants, their small size leads to high resonant frequencies, they are relatively easy to use, and the tips are relatively sharp and durable. On the other hand, their small size makes it difficult to make direct measurements of mechanical properties. Furthermore, determinations of the cantilever density or mass are of greater difficulty. Several methods have been proposed for experimentally calibrating cantilever normal force constants. In the following I will describe three experimental methods for calibration of cantilever spring constant that are commonly used.

3.2.1.1. Sader method

J. Sader and L. R. White in 1995 described a new method for calibrating the spring constant of cantilevers [164]. The mass of the cantilever is required and this is typically obtained from the density, thickness, and plan view dimensions of the cantilever. In particular, for the case of a rectangular cantilever [165], the spring constant is given by:

$$k = M_e \rho_c wtL\omega_{Vac}^2 \qquad (3\text{-}3)$$

Where ω_{vac} in the fundamental resonant frequency of the cantilever in vacuum, t, w, and L are the thickness, width, and length of the cantilever, respectively, ρ_c is the density of the cantilever, and M_e is the normalized effective mass which takes the value $M_e = 0.2427$ for $\frac{L}{w} \succ 5$ (Fig.3.7).

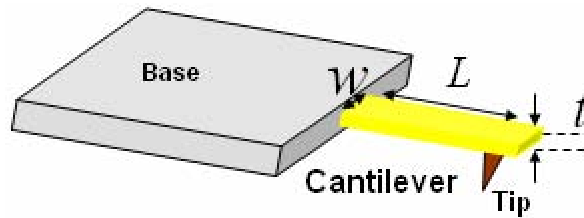

Fig.3.7 Rectangular AFM cantilever showing dimensions and tip position

Although simple in appearance, application of Eq. (3-3) has limitations for several practical reasons that we shall now discuss. In contrast to the plan view dimensions of a cantilever that are easy to measure thickness and width of cantilever with optical or electron microscope. The measurements of the frequency response of the AFM cantilever are commonly performed in air or a liquid medium. We note that the surrounding medium can significantly shift resonant frequency from its value in vaccum. The quality factor Q_f of the fundamental mode of the cantilever in fluid greatly exceeds 1. The vacuum resonant frequency ω_{vac} is related to the resonant frequency in fluid ω_f by:

$$\omega_{Vac} = \omega_f \left[1 + \frac{\pi \rho_f w}{4 \rho_c t_c} \Gamma_r(\omega_f) \right]^{\frac{1}{2}} \qquad (3\text{-}4)$$

where the a real mass density $\rho_c t_c$ is given by:

$$\rho_c t_c = \frac{\pi \rho_f w}{4}\left[Q_f \Gamma_i(\omega_f) - \Gamma_r(\omega_f)\right] , \quad (3\text{-}5)$$

where ρ_f is the density of the fluid, Γ_f and Γ_i are respectively, the real and imaginary components of the hydrodynamic function Γ. We note that $\Gamma(\omega)$ only depends on the Reynolds number

$$R_e = \frac{\rho_f \omega w^2}{4\eta} , \quad (3\text{-}6)$$

where η is the viscosity of the surrounding fluid, and is independent of the cantilever thickness and density. Sader *et al.* obtain the required result

$$k = 0.1906 \rho_f w^2 L Q_f \Gamma_i(\omega_f)\omega^2 . \quad (3\text{-}7)$$

Equation 3-7 relates the spring constant k directly to the plan view dimensions of the cantilever, the fundamental mode resonant frequency ω_f, and the quality factor Q_f in the surrounding fluid. This expression is valid provided the quality factor $Q_f \succ\succ 1$, which is typically satisfied when the cantilevers are placed in air.

3.2.1.2. Thermal noise method

Thermal vibrations of the cantilever are one fundamental source of noise in atomic force microscopy. Thermal noise has been calculated using the equipartition theorem. In thermal equilibrium each system has total mean value of energy given by:

$$W = \frac{1}{2} k_B T . \quad (3\text{-}8)$$

Where k_B is Boltzmann constant, T is the absolute temperature. When bending the cantilever by a small amount Z its potential energy is

$$V = \frac{1}{2} k z^2 \quad (3\text{-}9)$$

where k is spring constant. If the cantilever is shaped like a bar with rectangular cross section (Fig.3.7), the spring constant is given by:

$$k = \frac{0.25 E W t^3}{L^3} \quad (3\text{-}10)$$

where is L the length, w the width, E the elasticity modulus and t the thickness. Putting equation Eq.3-8 to Eq. 3-10, we obtain:

$$\frac{1}{2}k_B T = \frac{1}{2}k\hat{Z}^2 \tag{3-11}$$

where $\hat{Z}^2$ represents the mean square deflection of the cantilever caused by thermal vibrations.

$$\sqrt{\hat{Z}^2} = \sqrt{\frac{k_B T}{k}} = \frac{0.64\,\mathring{A}}{\sqrt{k}} \tag{3-12}$$

Numbers in Eq.3-12 are valid at a temperature of 22°C.

The measurable amplitude of thermal noise depends on the temperature and cantilever deflection. In many AFMs cantilever deflection is measured with the optical lever technique. With the optical lever technique the inclination at the end of the cantilever $dz(L)dx$ is measured rather than the deflection $z(L)$ itself. In equilibrium, the deflection is related to the inclination by:

$$Z(L) = \frac{2L}{3}\frac{dZ(L)}{dx} \tag{3-13}$$

For calibration of the cantilever a certain deflection $z(L)$ can thus be related to an equivalent change of inclination $\frac{dz(L)}{dx}$ by the factor $\frac{2L}{3}$. Hence, when the optical lever technique is applied one is interested in thermal noise of $\frac{dz(L)}{dx}$ rather than thermal noise in $z(L)$. Then thermal noise should be zero since the end of the cantilever, supported by hard substrate, does not move in the z z direction. Still, thermal fluctuations cause noise in $\frac{dz(L)}{dx}$.

Butt *et al.* calculated thermal noise considering explicitly all possible vibration modes of the cantilever [166]. They used a partial differential equation which describes transversal vibrations of the cantilever. In thermal equilibrium each vibration mode has a mean thermal energy of $\frac{1}{2}k_B T$. Transversal vibrations of a bar in the z direction are described by the partial differential equation

$$\frac{d^2 Z}{dt^2} + \frac{Et}{12\rho}\frac{d^4 Z}{dX^4} = 0. \tag{3-14}$$

ρ is the cantilever density. In addition to Eq.3-14, boundary conditions determine the behavior of the cantilever. For a bar fixed at one end (at $x = 0$) and free at the other (at $x = L$), we can calculate results of the last equation. Fig.3.8 shows the first four vibration modes of a cantilever with a free and a supported end.

They have the final result that when cantilever deflection is measured with the optical lever technique thermal fluctuations of the cantilever cause a virtual mean deflection (the square root of the mean square cantilever deflection) of

$$\sqrt{\hat{Z}^{*2}} = \sqrt{\frac{4k_B T}{3k}} . \quad (3\text{-}15)$$

At 22°C it is

$$\sqrt{\hat{Z}^{*2}} = \frac{0.37 A^{\circ}}{\sqrt{k}} \quad (3\text{-}16)$$

with the spring constant in Nm^{-1}.

The thermal noise method is only valid under several assumptions. First, the wavelength of a variation mode of cantilever needs to be longer than the thickness of the cantilever. Also it assumes that the inclination of the cantilever is much smaller than unity. An important limitation is the shape of the cantilever, which was supposed to be a bar with rectangular cross section. Often cantilever are `V` shaped with triangular end. The spring constant of `V` shaped cantilevers are usually calculated by adding the spring constants of both arms [160, 161].This might lead to errors of up to %25 [164].

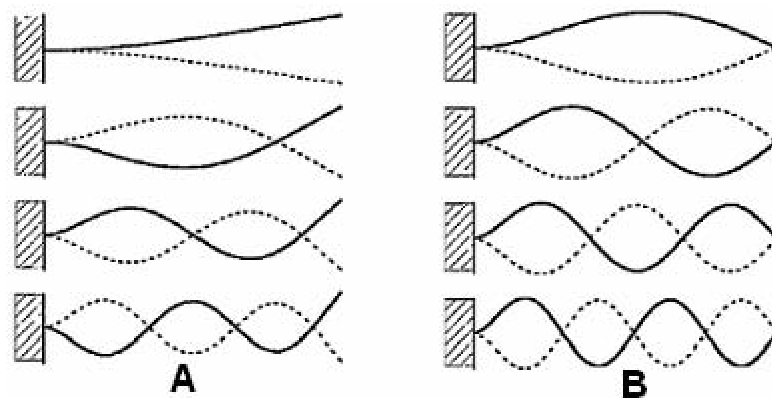

Fig.3.8 Shape of the first four vibration modes of a free (A) and a supported (B) cantilever. Figure taken from ref. [166]

3.2.1.3. Reference spring method

In this method the spring constant of an AFM cantilever is determined by pressing it against a reference cantilever (Fig.3.9) whose spring constant has been determinate before by another method. One possible way is to use a large-scale cantilever for which the spring constant can be calculated using Eq.3-2, as the reference cantilever (A. Torii *et al.* 1996) [167]. The deflection of the AFM cantilever to be calibrated and the force applied by the reference cantilever allow to calculate the spring constant using Hooke's law.
As the force acting on the cantilevers are equal,

$$k_{Ls}\delta_{LS} = k_{Test}\delta_{Test}, \qquad (3\text{-}17)$$

where k_{LS} and δ_{LS} are spring constant and displacement of the reference cantilever and k_{Test} and δ_{Test} are spring constant and deflection of the AFM cantilever. Hence, we can calculate relation between spring constant of reference and AFM cantilevers:

$$k_{Test} = k_{LS}\frac{1-C}{C} \qquad (3\text{-}18)$$

$$C = \frac{d\delta_{Test}}{dz_{LS}}. \qquad (3\text{-}19)$$

The differential term $\frac{d\delta_{Test}}{dz_{LS}}$ is the slope of a force curve after the AFM cantilever comes into contact with the reference cantilever. In the proposed method, it is not necessary to measure the accurate dimensions of the AFM cantilever.

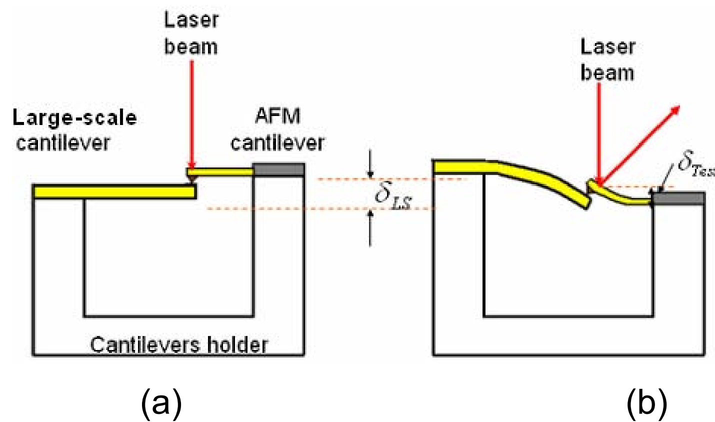

Fig.3.9 Schematic setup for spring constant calibration using a reference cantilever, (a)

before approach and (b) during contact [167].

Only the applied force and the AFM cantilever deflection are required in order to obtain the spring constant of AFM cantilever. The proposed method is so simple that users can calibrate an AFM cantilever when they want to measure an accurate magnitude of the force acting between an AFM cantilever and a surface. But often AFM laboratory has other tools for measurement exactly spring constant of AFM cantilevers.

3.2.2. Colloidal probe and tip radius

Various methods have been used to quantify the adhesive force between particles. Direct methods that investigate many individual particles include adhesive force measurement methods that use image processing or statistical processing, such as the centrifugal. The centrifugal method determines mean adhesive force by applying a constant force on a group of particles, finding the particle size and calculating the adhesive force [168]. Adhesion force between particles and planar surface have been studied and measured with the centrifugal method since more than 40 years. This technique has been used to characterize the behavior of industrial powders in pharmaceutical and food applications, paints, soil, clays and cells [169-173]. The study interaction between two particles and particle-planar surface, the colloidal method is better than centrifugal method, because we can use same particle or just two micro size particles with same roughness and other physical or mechanical properties in a series of experiment but in centrifuge technique we have to use about thousand or more particles in one measurement. Ducker *et al.* [174] and Butt *et al.* [175] used the colloidal probe method for measuring the force distance relationship between a colloidal particle and a macroscopic planar surface with sub-nanometer separation and sub-nanonewton force resolution. In other hands when we want study about interaction between more than two particle or thousands particles or particles with diameter over than 50 μm centrifugal technique is better than colloidal probe technique. We can glue particles to rectangular of triangular tipless cantilever [153]. The diameter range of particles usually is in the range 1μm to 50 μm [153]. For particle with diameter $D > 50$ μm, we have to choose stiffer cantilever. In this method we

can use any kind of material to glue on cantilever with thin layer of epoxy glue or resin. Attachment of colloidal particles is usually done by use of a micromanipulator under the control of an optical microscope. Basically, a thin layer of glue (~ 10^{-9} mm^3) is placed onto the very end of the cantilever and then the cantilever is brought in contact with the top of the micron-size particle [153]. This is accomplished either by keeping the cantilever fixed and using fine wires to move the glue and particles, or to pick up the glue and particle by moving carefully the cantilever. The particles were glued onto tipless cantilevers using a small amount of epoxy resin (Epikote 1004, Shell) by means of a micromanipulator (Narishige, MMo203, Japan) under an optical microscope. Therefore, particles were deposited on a glass slide on top of a heating stage. A small amount of resin was placed near the particles. After heating the stage above the melting temperature of the resin, a tiny amount of glue was taken up by touching the molten resin with the end of a tipless AFM cantilever. The selected particle could be picked up with the resin-coated end of the cantilever by gently touching it from above. As particles I used spherical borosilicate glass beads (roughly 4 µm diameter from Duke Scientific Corp., USA), silica microspheres with 3.5 µm (Bangs Laboratories, Inc, USA) and iron particles of 800 nm to 1.9 µm diameter (Carbonyl-Iron powder, BASF, Ludwigshafen, Germany).

Before attaching glass particles onto cantilevers, particles were washed and sonicated in an ultrasonic bath with ethanol, pure water from a Millipore water system. The Fig.(3.10) shows a SEM image of colloidal particle that has been attached on cantilever.

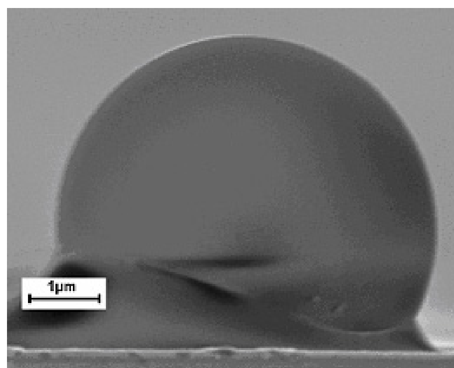

Fig.3.10 SEM images of a micron-sized silica sphere (silica microsphere with 3.5 µm in diameter from Bangs Laboratories, Inc, USA) glued to the end of a tipless cantilever.

In this study I used different cantilevers such as SiO_2, Si_3N_4, and colloidal particles with different radius and roughness (Fig.3.11). The tip radii of silicon oxide AFM tips were 5 nm < R < 50 nm and colloidal particle radii were 0.8 μm < R < 5 μm.

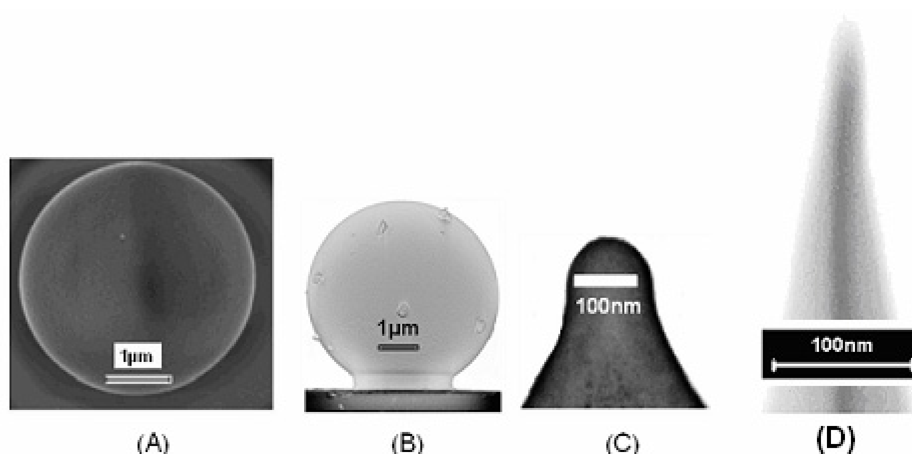

Fig.3.11 SEM images of four AFM probes. (A, B): colloid probes (silica and borosilicate particles), (C): Silicon nitride tip, and (D): SiO_2 cantilever

3.3. SURFACE PREPARATION

For the study of surface forces, it is important to use clean sample surfaces with a well defined surface chemistry. Since the measurements were carried out under ambient conditions, cleaning of the surfaces directly before the measurements is necessary to minimize contamination.

TiO_2 nanoparticles with average diameter of 20 nm were distributed homogeneously on the silicon wafer were prepared as described in detail before [176]. An asymmetric diblock copolymer of poly(methylmethacrylate) and poly (ethylene oxide) (PMMA-b-PEO) was synthesize via ATRP. The number average molecular weight is 57.7 kDa for PMMA and 17.9 kDa for PEO respectively. 0.0401 g PMMA-b-PRO, 3.011 g toluene and 0.992 g isopropanol and were mixed, followed by the addition of 0.0214 g 37% concentrated HCl solution and 0.0644 g titanium tetraisopropoxide (TTIP). All of the components are added within 4 minutes. After complete addition the common solution was stirred for 72 minutes. Films were prepared on Si (100) substrate by spin coating using a SÜss MicroTec Delta 80 spin coater at a rotation speed of 2000 rpm for 30.0 s. Calcinations of the films was carried out at 400°C for 4 hours in air with a heating rate of 6°C/min from room

temperature. Prof. Gutmann and coworker in polymer physics group of Max Planck Institute made this maple. Scanning electron microscopy (SEM) images were obtained on a field emission SEM (LEO 1530 Gemini) under 1 kV accelerative voltage. Due to the low voltage it was not necessary to coat the sample with a conducting layer.
Adhesion force measured on cleaned Teflon (Goodgfollow, Friedberg, Germany) on different humidity was used. The Teflon sample cleaned with ethanol in an ultrasonic bath for 3 minutes and rinse with pure water 3 times.

3.3.1. Plasma cleaning

This procedure removes thick (micron level) films of various organic materials. An oxygen (O_2) or argon (Ar) plasma is suitable for most organic films. Plasma cleaning has been shown by AFM to cause some roughening of evaporated and sputter-deposited gold surfaces [177], [178].
I used plasma cleaner for cleaning iron, silicate, glass, borosilicate, and titanium oxide particles, and silicon oxide and silicon nitride AFM cantilevers. Before each measurement cantilever with tip or particle was in a plasma cleaner (PDC-001, Harrick Scintific Corporation, USA) with Ar for 30 seconds.

3.3.2. RCA method (wet-cleaning)

After exposure to air the bare Si surface is usually covered with a thin native oxide layer and various impurities, such as particulates, organic residues, metals and ionic species. For silicon surfaces a variety of different cleaning procedures has been established to remove these impurities. The most common technique for silicon surface is the so-calls RCA method [179, 180]. It was developed in 1965 and still forms the basis for the preparation of clean hydrophilic silicon surfaces [179]. The RCA method removes particles (dust), metal, and organic contamination from the surface and a thin chemical oxide is grown on it [179].
First one mixes 50 ml ammonium hydroxide (30%), 50 ml Hydrogen peroxide (35%), and 250 ml water (Millipore grade) in a quarts beaker, resulting in a concentration ratio for the mixture of 1:1:5 [NH_4OH:H_2O_2:H_2O] (vol. Ratio 1:1:5). The substrates are fixed in a Teflon holder and immersed into the

mixture and the beaker is heated up to 80°C in a water bath and kept at this temperature. The temperature must not exceed 85°C. After 10 minutes the beaker is allowed to cool down. When the temperature reaches about 50°C one adds Millipore water into the beaker to the upper rim of the beaker. Then it is emptied half taking care not to expose the substrates to the atmosphere. The solution is again half diluted in the same way. This step is repeated eight times. Then the beaker is emptied completely and filled with water again twice. The beaker is again half filled with Millipore water and put into an ultrasonic bath for 10 minutes. Afterwards the substrates are rinsed with water again. Samples must be kept under water until they are used.

3.3.3 Cleavage of crystals

For the case of mica and highly oriented pyrolytic graphite (HOPG), preparation of clean and flat surfaces can be achieved by cleavage along preferred crystal orientations. Both materials have a layered structure where within the cleavage planes, atoms are bound covalently whereas the layers adhere only by van der Waals forces. Cleavage of these materials can be done by simply using adhesive tape that is pressed onto the material and pulled off, thereby stripping off layers of the material. In the case of mica one obtains a very hydrophilic surface, whereas HOPG is highly hydrophobic. As samples freshly cleaved mica from muscovite (Plano, Wetzlar, Germany) and freshly cleaved HOPG (SPi SUPPLIES, West Chester, USA) were used.

3.3.4. Etching of surfaces

In most of experiments we used very smooth surfaces as silicon wafers or mica. I want study the influence of roughness on adhesion force. Therefore I used silicon wafer etched with KOH solution. Anisotropic etching with KOH has become a standard and important processing step in the fabrication of bulk micro-machined semiconductor devices [181]. The quality of vertical roughness produced by the etching of Si in aqueous KOH has been studied by varying several experimental parameters such a molarities of KOH, time of etching, temperature, and stirring [181]. All our etching experiments were carried out in 0.25 M KOH that was heated to 70°C. The samples were kept in

KOH for 10 to 120 seconds. Before etching, all of the silicon samples were cleaned with RCA method or by rinsing with ethanol. After etching silicon surface with KOH, an increased roughness due to formation pyramids was observed (Fig.3.12). If silicon wafer etched on (100) direction, usually pyramids grow on surface. The height of pyramids on depended on etching time.

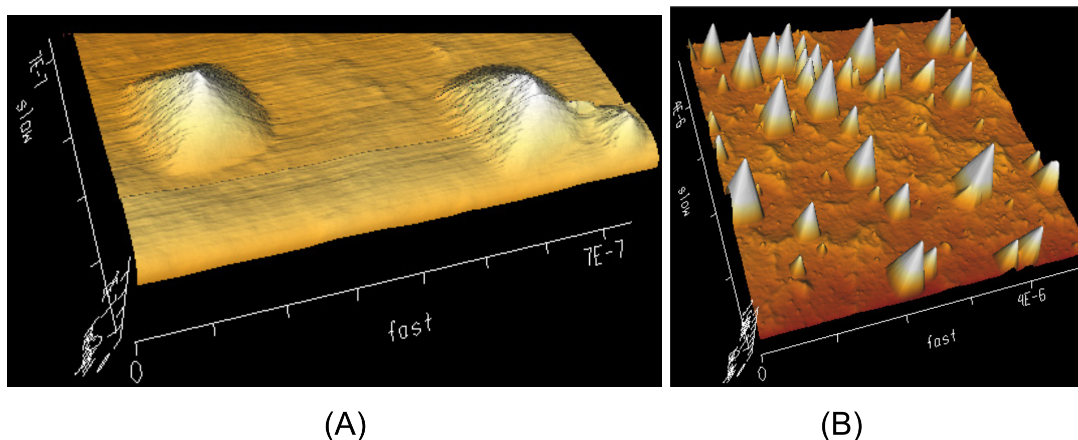

(A) (B)

Fig.3.12 AFM images of silicon wafer etched with KOH. (A): X = Y=Z= 700 nm after 30 s, (B): X=Y= 500 nm and Z of image were 350 nm after 90 s.

3.4. HUMIDITY CONTROL SYSTEM

One aim of this study is measuring surface forces (adhesion and capillary forces) for different relative humidity of the surrounding gas. First I used a glove box to enclose the whole AFM into its chamber. However, due to the large volume of the chamber it took very long time to change humidity and reach a new equilibrium value throughout the glove box. In a second attempt, I used a special AFM (E-Scope from Veeco, New York, USA) in which sample and scanning unit are enclosed by a chamber of approximately $12\times12\times12$ cm^3. Result of first preliminary experiments showed that the shape of adhesion force-versus-humidity curves often changed from experiment to experiment. Within one experiment adhesion forces change with time and often different results were obtained when increasing and decreasing humidity (hysteresis). For this reason, I used a special setup, which allowed a fast change of the humidity to minimize time effects and hysteresis; it consisted of

a combination of a standard AFM liquid cell and a device for defined mixing of two air streams. Volume of AFM liquid cell was about 0.6 µl.

To adjustment the relative humidity of water or other liquid a stream of nitrogen was split into a stream of pure nitrogen and one stream of saturated vapour (Fig.3.13). To saturate humidity with vapour, second stream of nitrogen was bubbled through a porous membrane into the liquid. The flow of both streams was controlled by digital mass flow controllers (Aalborg, New York USA). Then both gas streams were mixed and led into the liquid cell of the AFM which is sealed with an O-ring except for one outlet. The system is especially designed to allow for a relatively fast change of the vapour pressure. Relative humidity was in the chamber was measured using a humidity sensor (SHT 15 Sensirion, Switzerland) that was placed either at the inlet or outlet of the liquid cell. No significant difference of the humidity at inlet or outlet was observed indicating that the sensor output reflects in fact the humidity inside the liquid cell.

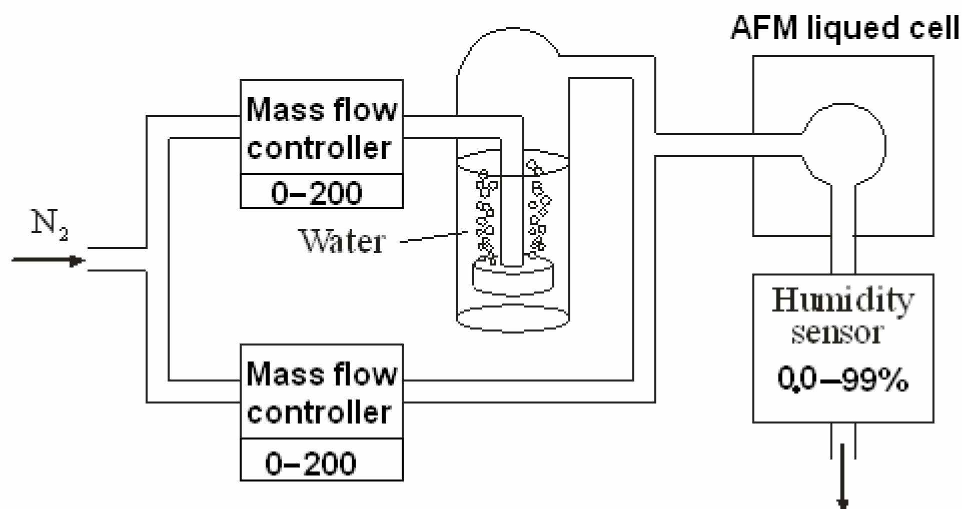

Fig.3.13 Schematic of the setup used to adjust the relative humidity

A whole experiment starting at low humidity to high humidity and reducing again to low humidity lasted typically 15 minutes (Fig.3.14). This was important because for more prolonged measurement times I noticed significant tip wear particularly at high humidity, and changes of the chemical properties of surface.

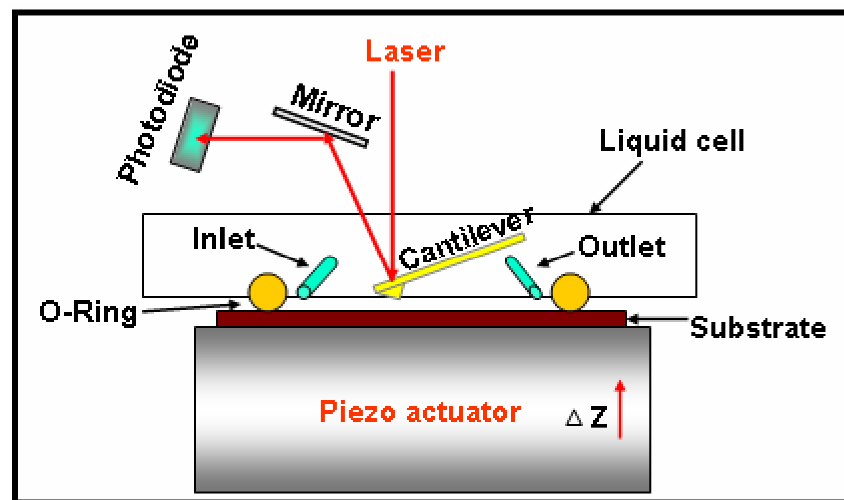

Fig.3.14 Schematic of the AFM liquid cell

4. RESULTS AND DISCUSSION

4.1. ADHESION FORCE DISTRIUBUTIONS

In this study I measured the adhesion forces between AFM tips or particles attached to AFM cantilevers and different solid samples. Smooth and homogeneous surfaces such as mica, silicon wafers, or highly oriented pyrolytic graphite (HOPG) and more rough and heterogeneous surfaces such as iron particles or patterns of TiO_2 nanoparticles on silicon were used. In the following I will show results of absolute values and distributions of adhesion forces on hydrophilic and hydrophobic surfaces.

4.1.1. Adhesion force on hydrophilic surfaces

First I studied distribution of adhesion forces on mica and silicon wafer surfaces. In this series of measurements, I used the JPK Nanowizard AFM in the so-called force volume mode (FV mode). The measurements of adhesion forces were carried out at a load force of roughly 30 nN. Each force curve was taken in 1.0 s with an interval of 1.1s between subsequent force curves. Fig.4.1 shows typical curves of cantilever deflection versus piezo position and adhesion force versus distance. Before each measurement the cantilevers were cleaned using a plasma cleaner in Ar gas atmosphere for 30 s.

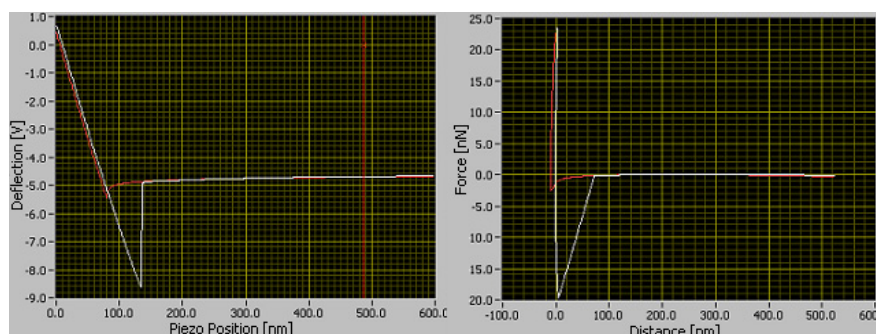

Fig.4.1 Left: Typical example of a detector voltage versus piezo position curve. Right: Adhesion force versus distance curve obtained from the raw data using linear fits of the zero force and constant compliance regions and the known spring constant of the AFM cantilever

The adhesion forces were measured on clean and fresh mica surface (RMS of 2- nm on area of 500 nm$\times$500nm) and probes were made of silicon (type 2)

and silicon nitride (type 1). Adhesion was measured in an array 32×32 points within an area 500 nm×500 nm. Histogram and adhesion force versus time of this measurement are shown in Figs (4.2- and 4.3).

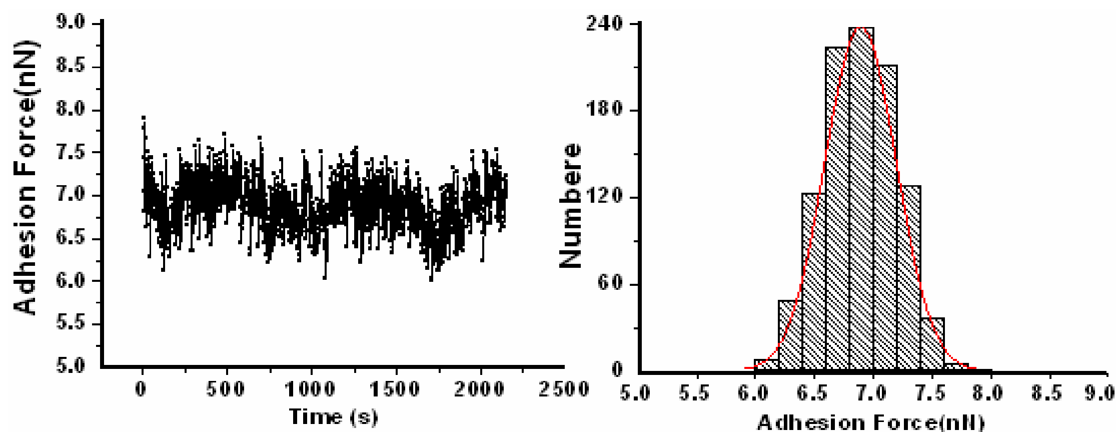

Fig.4.2 Left: Adhesion force measured versus time between mica surface and silicon tip. Right: Histogram of the distribution adhesion forces with Gaussian curves fit on. The mean value of adhesion force and relative width were 6.8 nN and 4.4%. The inset shows a typical deflection-versus-piezo curves measured.

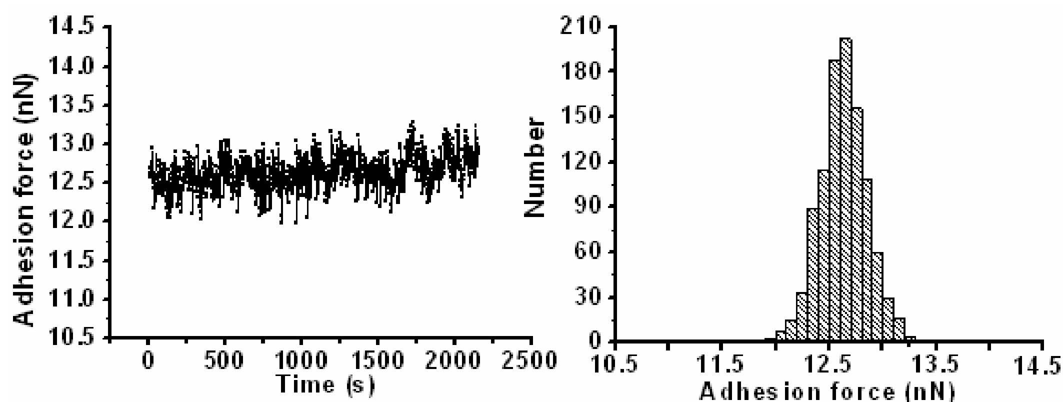

Fig.4.3 Left: Adhesion force measured versus time between a freshly cleaved mica surface and silicon nitride tip. Right: Typical histogram adhesion forces.

In another series of experiments, adhesion forces were measured on a silicon wafer (RMS of 1.6 nm on an area of 500 nm×500) surface. Before each measurement, silicon wafers were cleaned with the RCA method. The AFM probe was a silicon nitride tip (type 1).

The results show that distribution of adhesion forces can be fitted by a narrow Gaussian curve. The average adhesion force on silicon wafers is higher than

on the mica surface and the adhesion force distribution for mica is wider than for silicon.

The adhesion force versus time plot shows that one can distinguish at least two kinds of variations: First, there is a random noise, and second, there are fluctuations on a slower time scale. The same kinds of fluctuations were observed in all experiments. The origin of these phenomena is discussed below (In section 4.2).

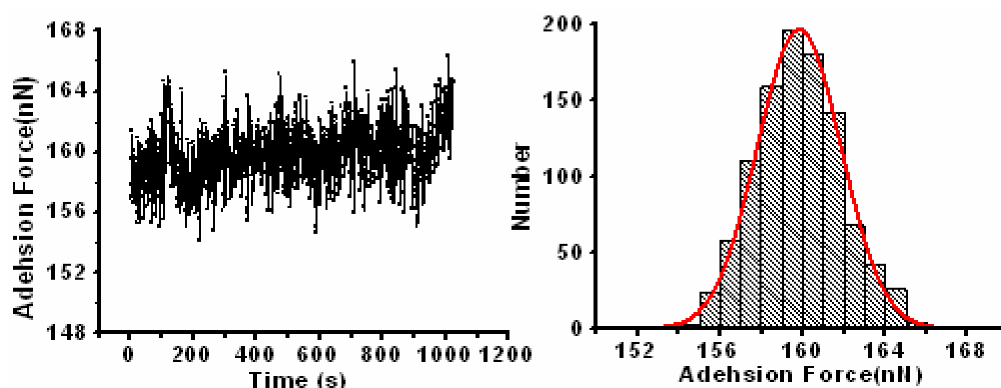

Fig.4. 4 Left: Adhesion force measured versus time between a fresh silicon wafer surface and silicon nitride tip. Right: Typical histogram of adhesion force. The mean value of adhesion force and relative width were 159.6 nN and 0.03%.

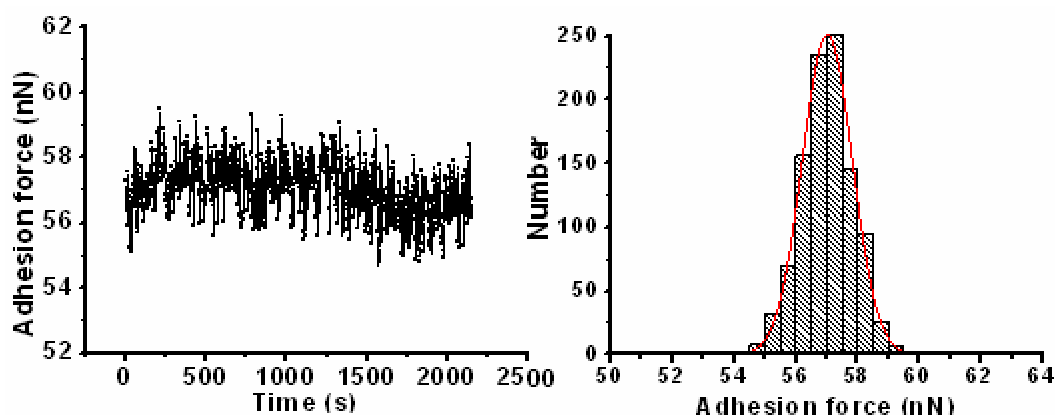

Fig. 4.5 Left: Adhesion force measured versus time between silicon wafer surface and silicon tip. Right: Histogram distribution of adhesion force.

4.1.2. Adhesion force on hydrophobic surfaces

Highly Oriented Pyrolytic Graphite (HOPG) provides an atomically smooth, homogeneous, and hydrophobic surface. Also it is electrically conducting as well as chemically inert; this makes it an ideal substrate for performing surface force measurements.

The adhesion forces were measured in an array of 64×64 or 32×32 points within an area of 500 nm×500 nm on HOPG. In each experiment I imaged the surface with the AFM before and after the force measurements. The results of adhesion force versus time for this measurement are shown in Fig.4.6A and Fig.4.6B.

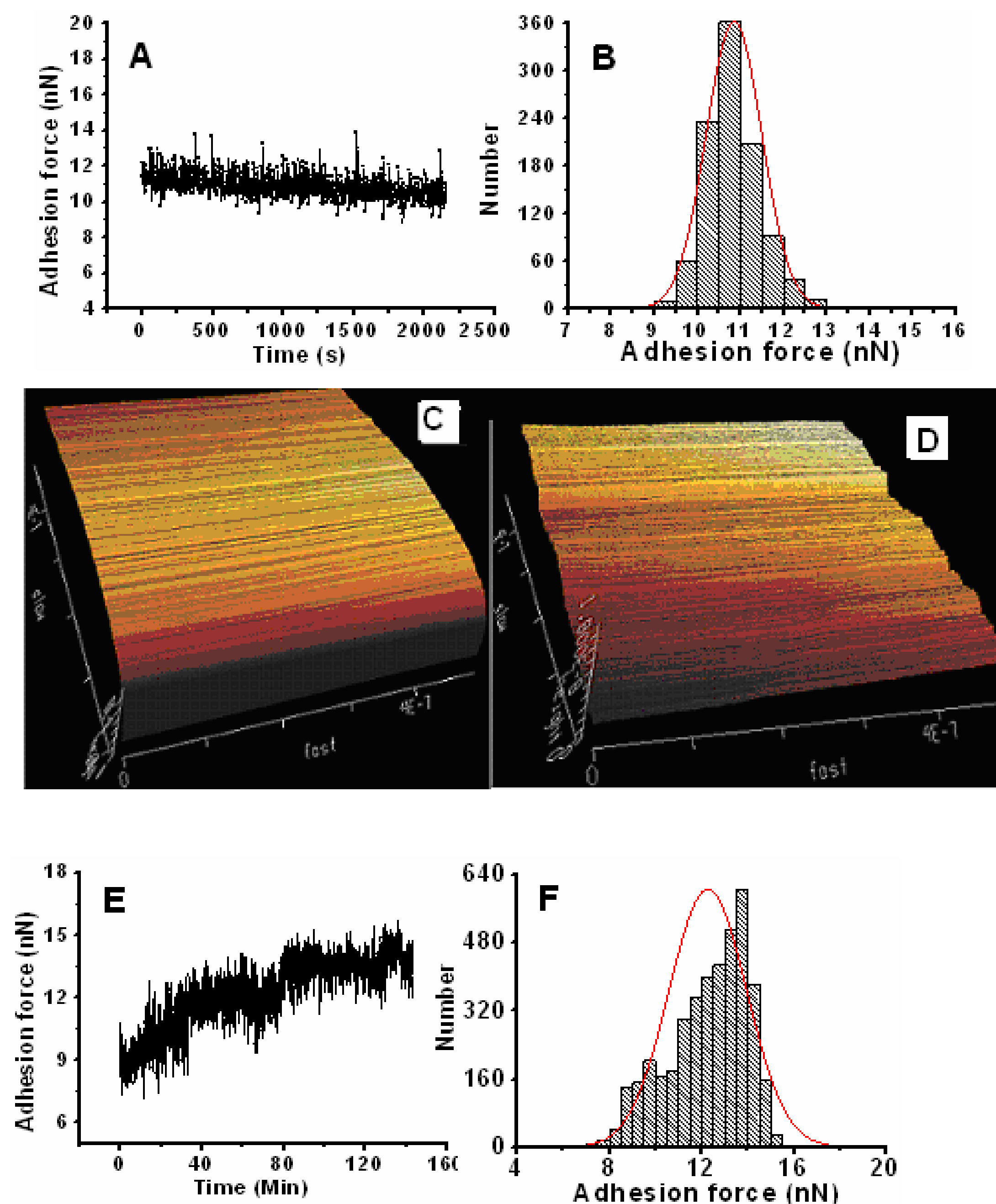

Fig.4.6 A and B: Typical histogram of adhesion force and adhesion force measured versus time between a HOPG surface and a silicon nitride tip. C and D: The images of HOPG before and after measured FV that show surface was damage during measured. F and F: Adhesion force measured versus and histogram distribution of adhesion force between HOPG surface and silicon nitride tip with damage surface.

The histogram shows a peak at mean value of $\overline{F} = 65.7$ nN and a relative width of 4.4%. The width of the distribution for HOPG was larger for the silicon and mica surfaces. The images revealed that during the experiments on mica and silicon wafer no damage of the surfaces occurred (expect for two experiments on silicon), but for the HOPG surface often surface damage was observed (Fig. 4.6C and Fig.4.6D). Furthermore, SEM images of AFM tips taken after measurements showed that sometimes the tip was contaminated presumably with HOPG flakes. The results of adhesion force versus time for this measurement are shown in Fig.4.6E and Fig.4.6F.

4.1.3. Adhesion force on particle surfaces

a) Glass particle

For measurement of adhesion force on a particle surface I glued a glass particle (R = 3 μm) on glass substrate with a thin layer of epoxy resin. The cantilever and tip used was type 2. Before measurement of adhesion force I took images on the top of glass particle (Fig.4.7) then measured adhesion force with FV mode (64 $\times$ 64 points and on a 500 nm$\times$500 nm area).

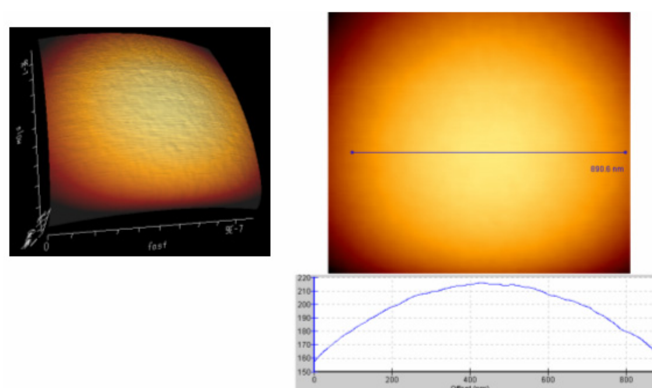

Fig.4.7 Left: Array of adhesion force measurement that was top of glass particle (3D). Right: Surface image of glass particle (2D).

Fig.4.8 shows results from such an experiment. Distribution of adhesion force was Gaussian but was wider than for a planar surface such as mica or silicon wafer.

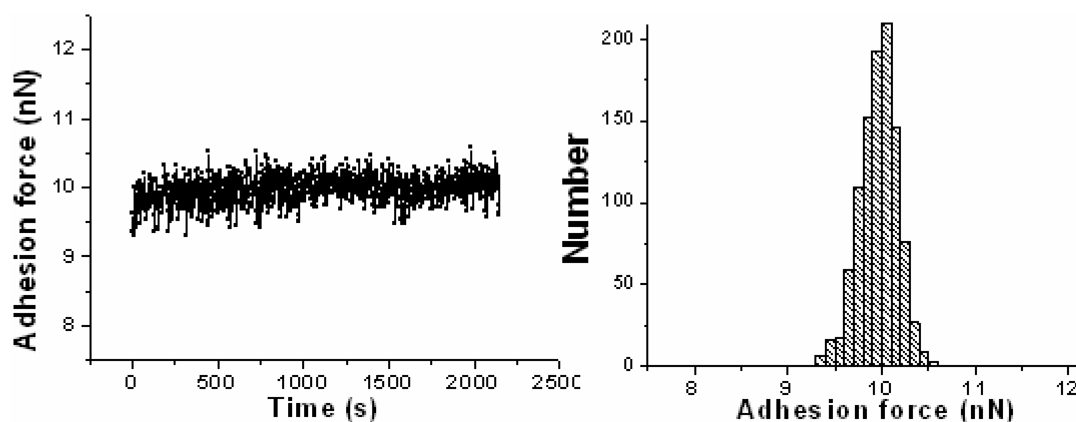

Fig.4.8 (Right): Adhesion force measured versus time on Glass particle R = 3 µm surface measured with a Si tip (type 2). Left: Histogram of adhesion forces.

For my experiments I chose spherical glass particles with particle radii 3 and 5 µm. To measure the adhesion force between two solid particles, glass microspheres were glued with epoxy heat resin (Epikote 1004, Shell) to a microscopy slid and to the ends of AFM cantilever (type 3). I measured adhesion force with FV mode (64×64 points on a 500 nm×500 nm area in 147 minutes). Results show that distribution was 10 time wider than for the other experiments (Fig.4.9). The histogram show that may be colloidal probe slid on spherical substrate during force measurement.

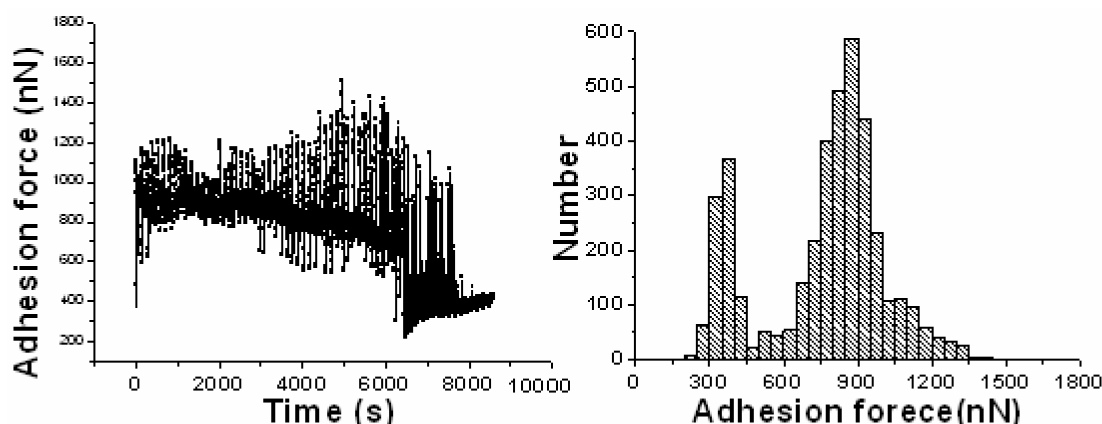

Fig.4.9 Adhesion force versus time (left) and distribution of adhesion forces (right) measured between two glass particles (R = 3 µm and 5 µm).

b) Carbonyl Iron Powder particle

Iron particles used in this study were from carbonyl iron powder (CIP). Fig.4.10 is a AFM image of CIP surface. It shows a pronounced surface roughness of the iron particle. The iron particles were glued on glass slid with

epoxy resin. Before experiment, I cleaned surface of iron particle and cantilever tip with plasma cleaner. The adhesion forces were measured in an array of 64$\times$64 or 32$\times$32 points within an area of 500 nm$\times$500 nm (RMS of 19 nm on 500 nm$\times$500 nm). Histogram shows that a mean value of $\overline{F} = 6.9$ nN and a relative width of 14.702% (Fig.4.10 Left and Right).

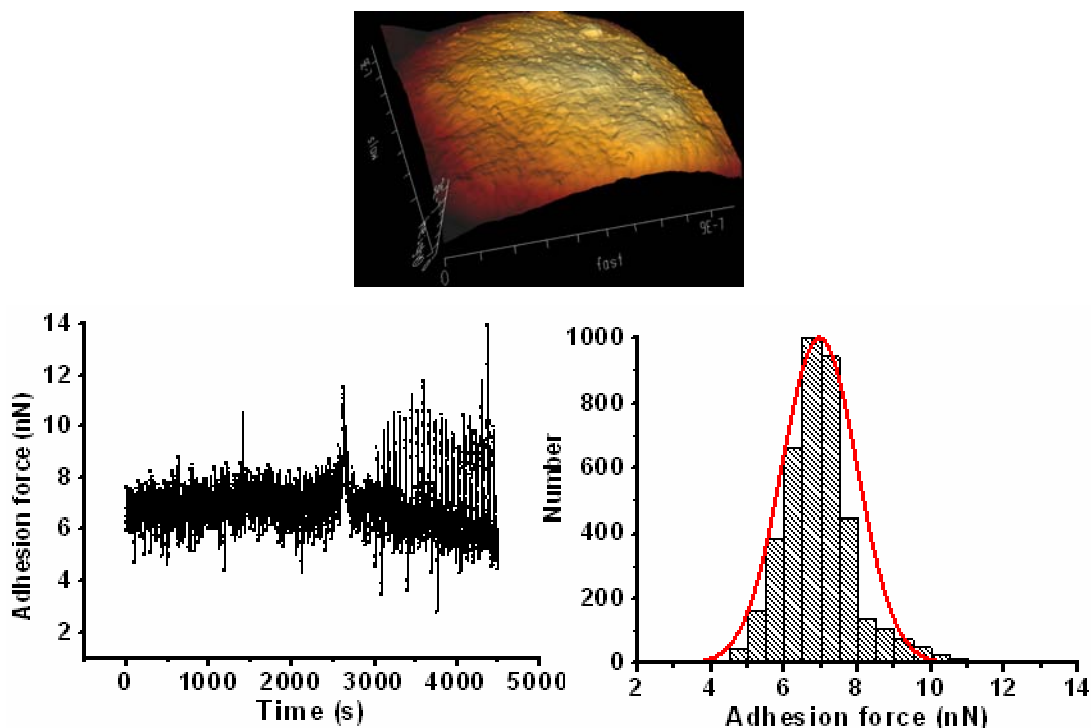

Fig.4.10 Top: AFM image of the surface of an iron particle (scan size 500nm $\times$500 nm). Bottom left: Adhesion force measured versus time. Bottom right: Adhesion force distribution.

4.1.4. Adhesion force on rough surfaces and adhesion map

The effect of roughness on adhesion force and distribution of adhesion force has been studied under different ambient conditions and different surfaces with AFM [32], [182]. Rabinovich *et al.* [34] found that the asperity radius is not sufficient to describe the adhesion force on technically rough surfaces. I measured adhesion force on roughness surface and results are shown in the following section.

a) Silicon wafer surface

Silicon wafers are usually very smooth surface and results of my experiments showed that distribution of adhesion forces could be fitted by a narrow Gaussian curve. I want study effect of surface roughness on distribution of

adhesion force under ambient humidity. I used silicon wafer modification with KOH (Fig.4.11). Load force was about 30 nN, temperature was 25°C, and humidity was 40-45%. The result shows (Fig.4.12) that distribution of adhesion force became wider than for surfaces smooth surfaces. In one experiment, mean adhesion force was 7.9 nN and standard deviation for 1024 (32×32) force curves was 2.8 nN corresponding to a width of distribution of 36.5%. One series experiment shows that width of distribution of adhesion forces were between 30% and 45%. This effect arises when during force measurement tip and surface have different contact area then changed surface forces.

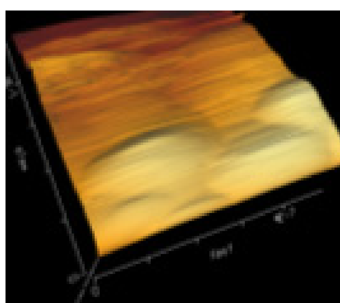

Fig.4.11 Image of silicon wafer after etching with KOH (RMS of 18.4 nm on an area of 500 nm × 500 nm)

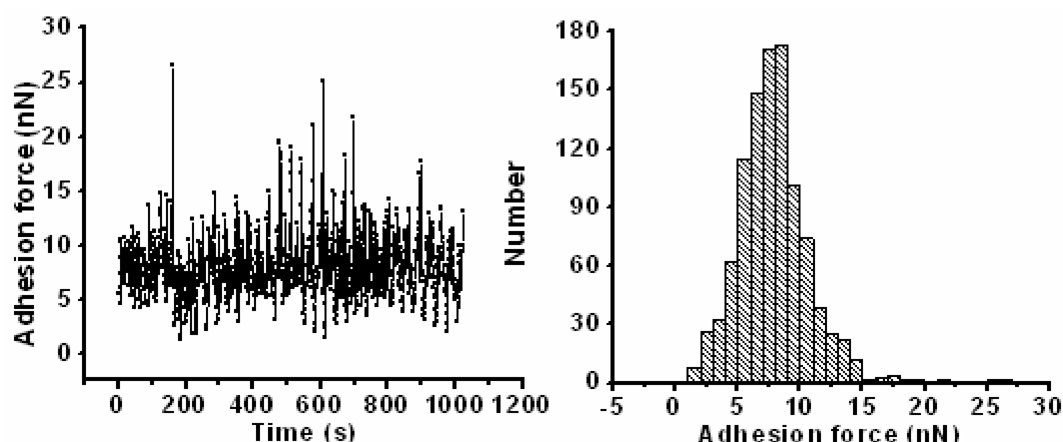

Fig.4.12 Left: Adhesion force measured versus time (s). Right: distribution of adhesion force on a silicon wafer after etching with KOH. The histogram shows a relative width of 36.5%.

b) Titanium oxide particles on silicon wafer

I used regular structure and inhomogeneous patterns of TiO_2 nanoparticles on silicon wafer (Fig.4.13). I measured adhesion force on this sample in two kinds of area, first was large and second was very small area. To demonstrate

that roughness can cause an increased width of the adhesion histogram, I measured adhesion value on a silicon wafer with TiO_2 nanoparticles. The results of force-volume on large area (64×64 on a area 1 μm$\times$1 μm) shows that since the mean distance between TiO_2 particles is about 55 nm and each particle has a typical radius of 6-10 nm most of the surface is not covered by titanium particles.

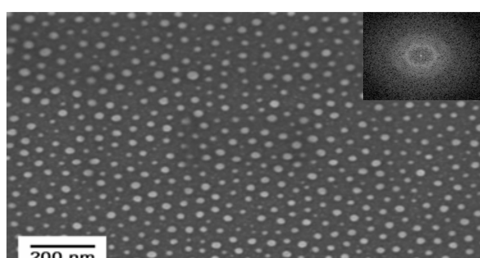

Fig.4.13 SEM image of a calcinated silicon wafer with TiO_2 nanoparticles on a silicon wafer surface. The inset is the corresponding fast Fourier transform (FFT) pattern. It shows a typical spacing between nanoparticles of 55 nm (RMS of 23.7 nm on an area of 160 nm × 160 nm).

The histogram of adhesion forces showed a wide, asymmetric distribution with a maximum at 35 nN (Fig 4.14). The main peak is caused mainly by the interaction of the silicon tip with silicon surface because only less than 20% of the surface area is covered with TiO_2 particles. The tail of the distribution extending to higher adhesion values is probably caused by the relatively few cases where the tip interacts with TiO_2.

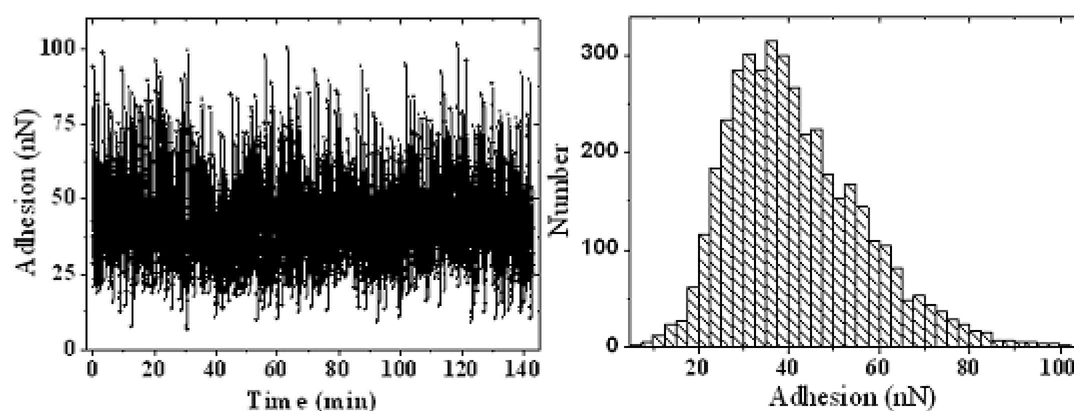

Fig. 4.14 Left: Adhesion force measured versus time (min). Right: Histogram of adhesion forces measured between a silicon tip and a silicon wafer surface covered with TiO_2 particles. The histogram shows a peak at a mean value of $\overline{F} = 41.5$ nN and a relative width of 34.6%.

To verify this I zoomed in on a small scan area (15 nm × 15 nm), which was half covered by TiO_2 and half by the silicon surface. Then indeed a distribution with two peaks was observed (Fig.4.15), one with low adhesion forces caused by interaction with the silicon wafer, another at higher forces caused by the interaction with TiO_2. This results agree with results of Ando on roughness surface [183]. The mean value of adhesion force between silicon tip and TiO_2 was two times the adhesion force between silicon tip and silicon wafer.

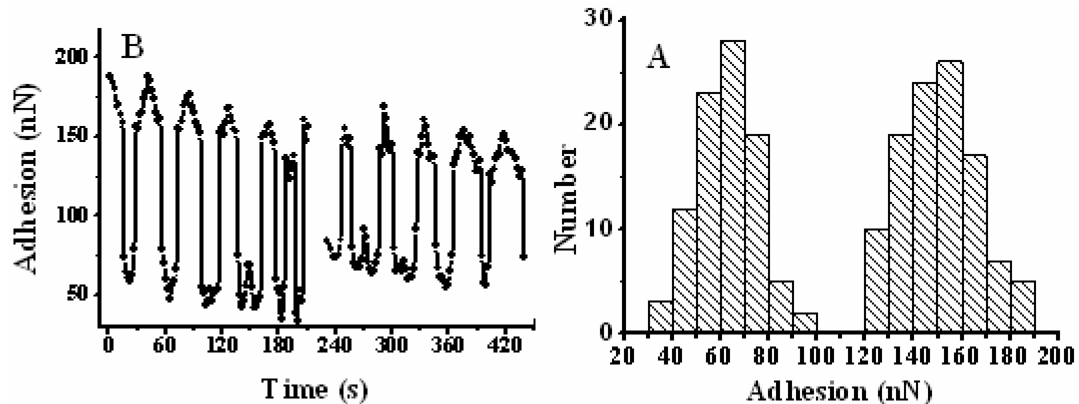

Fig.4.15 Left: Adhesion force measured versus time between silicon tip and a surface partly covered with TiO_2 cantilever (No.2). Right: Histogram of adhesion forces. Lower adhesion forces were caused by interaction with the silicon wafer, another at high force caused by the interaction with TiO_2 because surface energy of TiO_2 in higher than silicon.

Fig.4.16 shows adhesion map off area (15 nm × 15 nm) that half covered by TiO_2 and half by the silicon wafer.

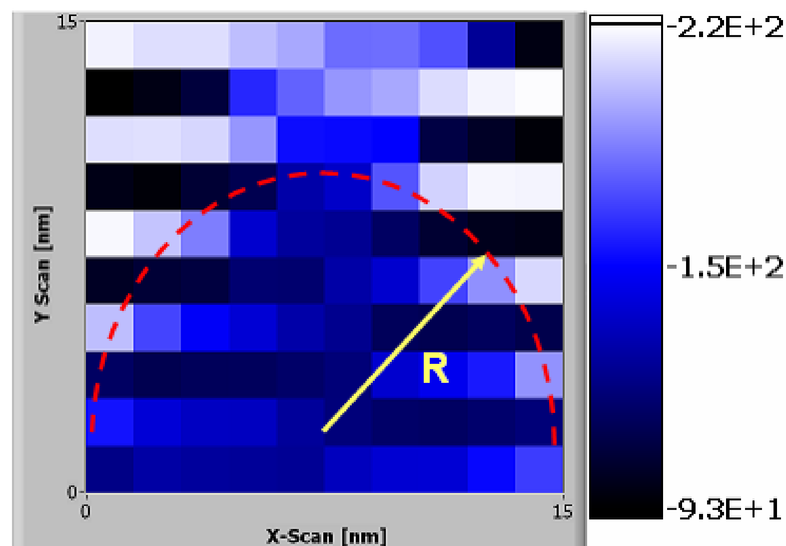

Fig4.16 Adhesion map (10 × 10 force curves) for interaction between TiO_2 particle and silicon tip (No. 2). The area of half circle with radius R covered by TiO_2 on silicon wafer.

A single force curve records the force felt by the tip as it approaches and retracts from a point on the sample surface. To measured the adhesion force and surface tension of surface at various location, FV imagines consisting of array of 32 × 32 or 64 × 64 force curves were recorded in parallel with topographic images on different samples [155][156-158]. For each force curve, the sample vertical displacement, *Z*, was controlled to obtain the same maximum vertical deflection, and thus the same maximum applied force.

C) Carbonyl Iron Particle (CIP)

I measured adhesion force between an AFM tip and heterogeneous surface (iron particle) with FV method. Comparison of the topographic image with adhesion map presented in Fig.4.17 confirms the direct relationship between the topographic features and the relative force of adhesion associated with each domain; the pits in the topography image correspond to areas of high adhesion. This results agree with results of Heinz *et al*. [156] and Eaton *et al*. [184].

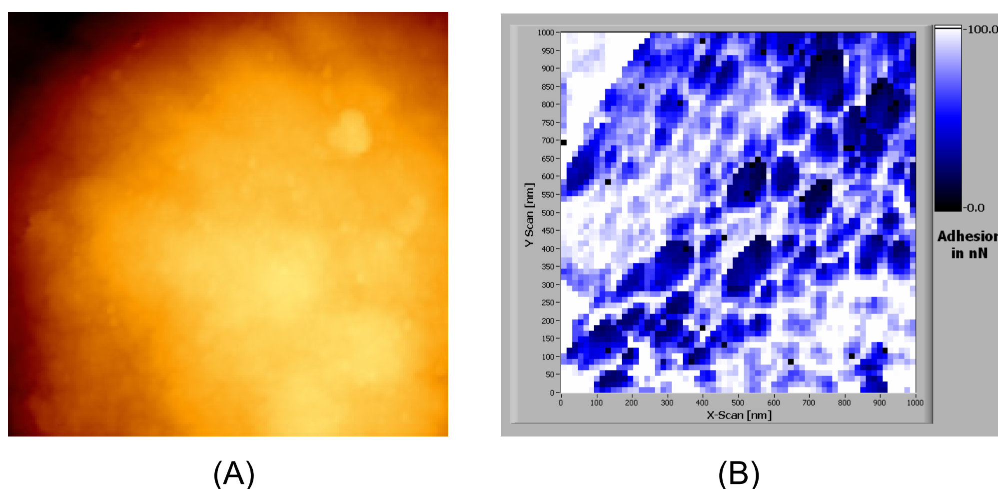

(A) (B)

Fig.4.17 Topography (A) and adhesion force map (B) images of an iron particle that surface is heterogeneous. Both images took same area and relative together. Each force curve took 1.0 s with an interval of 1.1 s between subsequent curves.

The adhesion force measured between a silicon tip (type 2) and iron particle of 1.9 μm diameter on an area of 500 nm × 500 nm areas at a load of 30 nN. The adhesion forces were measured on an even grid of 32 × 32 points.

Fig.4.18 shows surface image and adhesion force map of a freshly cleaved mica surface. The adhesion forces of mica took by FV mode in an array 32× 32, and on area of 500 nm × 500 nm.
Results of other measurement on mica surface shows that 1024 force curve are same and adhesion map is equal (Fig.4.18).

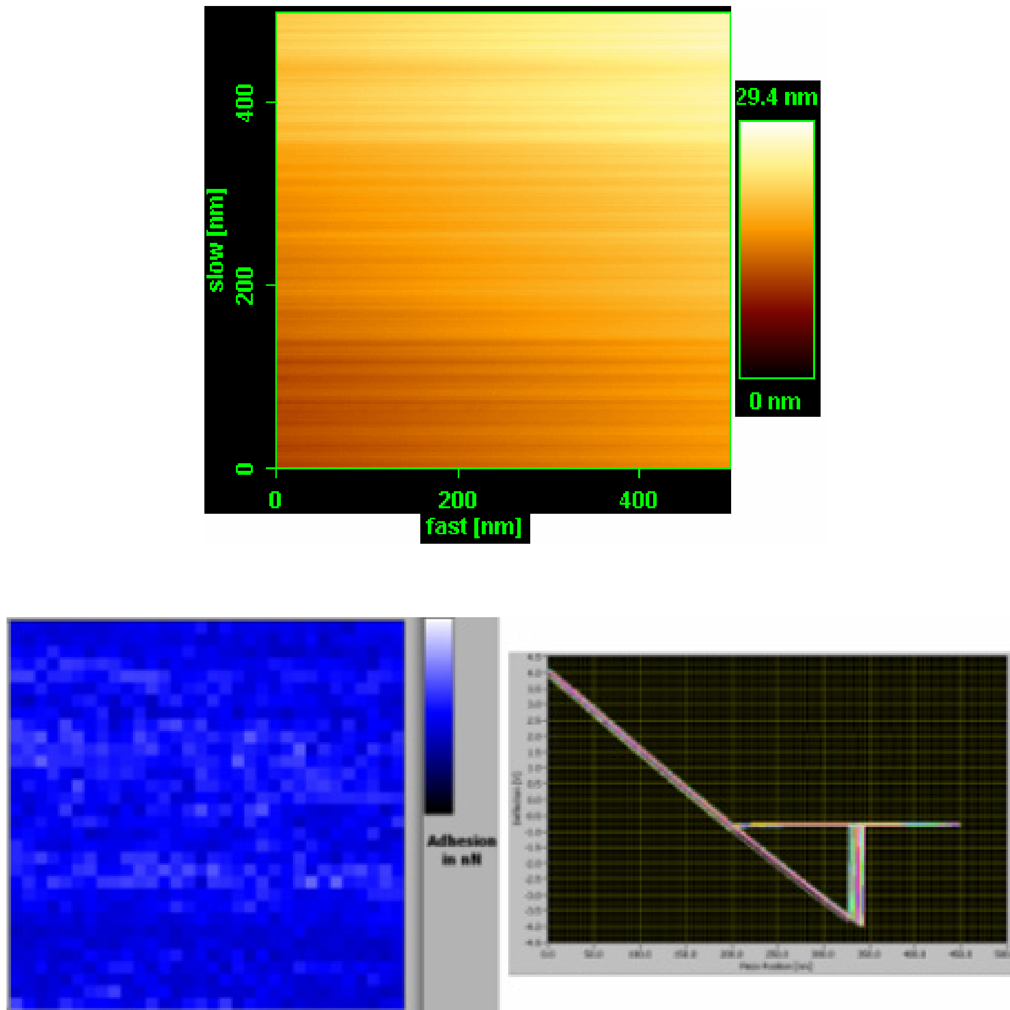

Fig.4.18 Up: AFM Surface image of mica (RMS of 1.8 nm on an area 500 nm × 500nm), Adhesion map (down left) and all force curves of adhesion force measured between mica surface and Silicon tip (down right).

4.2. EFFECT OF LOAD

To study the influence of load on the adhesion force a series of experiment was carried at different loading forces (20 – 80 nN). Here, adhesion forces were measured between a silicon tip (type 3) and silicon wafer (Table 2). The

results shown that adhesion force and force distribution did not change significantly with load.

Table 3

	Load force (nN)	Mean (nN)	Sd	$\frac{Sd}{Mean}$ %
1	20	21.91491	2.16282	9.869
2	20	20.66361	1.67988	8.129
3	40	20.17259	2.0821	13.425
4	40	16.69631	1.28547	7.699
5	60	15.9307	1.29864	8.151
6	80	16.88456	1.1592	7.297

Table 3: Six different load forces between silicon tip and silicon wafer surface and mean value of adhesion forces, Sd, and distribution width of adhesion forces.

4.3. FACTORS INFLUENCING THE DISTRIBUTION OF ADHESION FORCE

The result of a typical experiment is the histogram of adhesion forces as shown in Fig. 4.16A. The histogram of adhesion forces shows a peak at mean value of $\overline{F} = 6.9nN$ and relative width of 4.4& (Fig.4.19). When looking at the results of adhesion forces measured versus time and the corresponding distributions, one question is that why adhesion force was not a single value? Or in other words which factors influence the distribution of adhesion force? The force measured versus time plots show fluctuations. To analyze sources of these variations, it is instructive to plot the measured adhesion forces versus the number of the force curve (Fig 4.19B). The abscissa corresponds to a time scale because one force curve was taken at constant time interval of 2.1 s. This plot shows that I can distinguish at least two kinds of variations.
First, there is a random noise. The adhesion values vary from one force curve to the other in an uncorrelated way. Second, there are fluctuations on a slower time scale. These are obvious in the original plot, and they become clearer after smoothing. The red curve was obtained by a 32 point FFT (fast Fourier transform) smoothing of the original curve (Fig.4.19B). The resulting smoothed curve, which highlights these slower fluctuations, is shown in red. When subtracting the slower fluctuations (Fig.4.19C) and analyzing the

adhesion force distribution again a random noise of 3.5% remained. These variations were observed in all experiments: A random noise plus fluctuations on a slower time scale. With respect to changes of the adhesion force in time I used silicon and silicon nitride probes and mica, silicon wafer, and HOPG (highly oriented pyrolytic graphite). We know that these samples represent the smoothes, most homogeneous surfaces. For this reason variation in adhesion forces are expected to be minimal. In a series experiment, mean value of adhesion forces were 5-13 nN and variation of relative width of distribution for 1024 force curves (corresponding to 36 min time span) were 1.2% - 6%. I did not notice any systematic tendencies.

The lowest variations were observed for one experiment with a silicon tip on mica ($\frac{\Delta F}{\overline{\overline{F}}} =$ 1.5%) and one with a silicon nitride tip on silicon wafer ($\frac{\Delta F}{\overline{\overline{F}}} =$1.2%). To find the contribution of random noise I subtracted the slower fluctuations and analyzed the results again. A random noise of $\frac{\Delta F}{\overline{\overline{F}}} =$ 1.2% and $\frac{\Delta F}{\overline{\overline{F}}} =$1.1% remained, respectively.

When measuring adhesion force between colloidal probes (glass microsphere) and silicon wafers the mean adhesion; force values increased to 650 nN. Using Derjaguin-Muller-Toporov (DMT) theory [8] and relating the adhesion force to an effective surface energy of the solid $\gamma_s = \frac{F}{4\pi R}$, I get $\gamma_S = 0.04$ N/m. Usually, particles showed slightly higher variations than microfabricated tips. In one case, however, the variation was only $\frac{\Delta F}{\overline{\overline{F}}} =$1.9%, despite the fact that the adhesion force varied systematically over the (500 nm)^2 area (Fig 4.20) subtracting the slow fluctuations gave a random noise of $\frac{\Delta F}{\overline{\overline{F}}} =$1.2%.

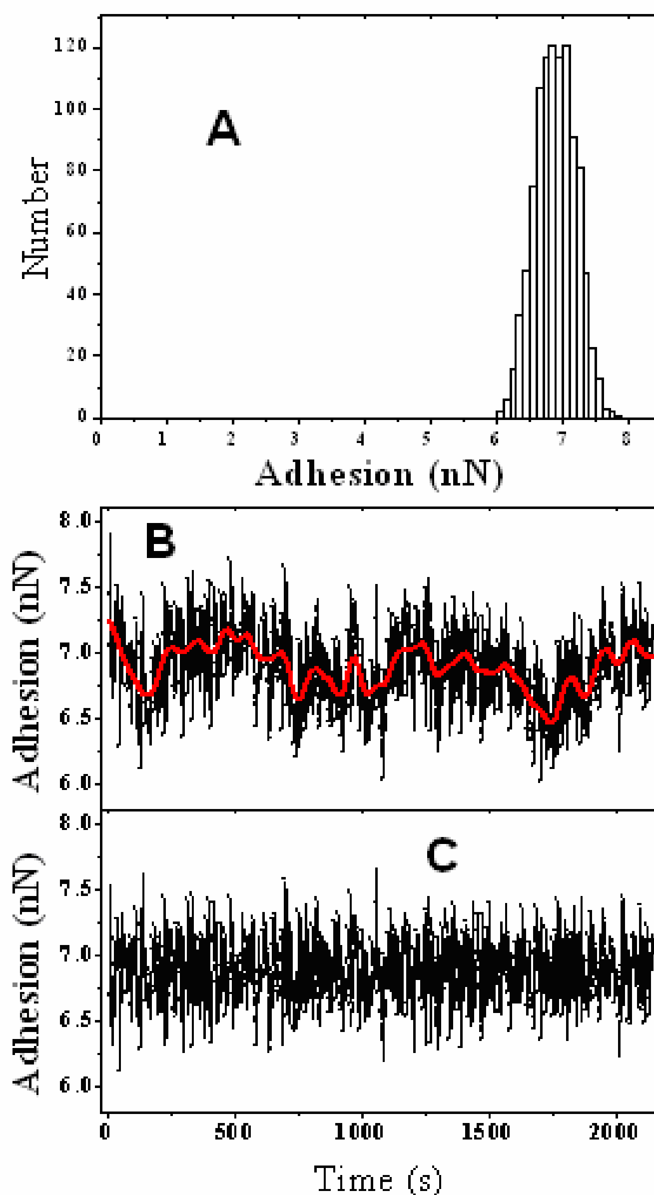

Fig.4.19 A: Typical Histogram of adhesion forces measured between a silicon nitride tip (type 1) and mica at one spot and at a load of 30 nN. Each force curve took 1.0 s with an interval of 1.1 s between subsequent curves. The whole series contains 1024 force curves and took 36 min. B: Adhesion force measured versus time. Dividing the time by 2.1 s gives the number of the force curve. The grey curve was obtained by a 32 point FFT (fast Fourier transform) smoothing of the original curve. Curve (C) was obtained by subtracting the smoothed curve from the original results and adding the mean adhesion force.

The slow fluctuations are not likely to be the result of variation in external factors such as temperature, humidity, etc. because those were kept constant. I believe that slow fluctuations are caused by structural changes in the tip due to the high stresses and gradients in contact. The observed fluctuations in the

adhesion force make it difficult to measure defined adhesion forces for a mechanical micro- or nanocontact. Even if two solid bodies are brought into contact under precisely the same conditions (same place, load, direction, etc.) the result of such a measurement might not be the same as the previous in a contact and it is not perfectly reproducible.

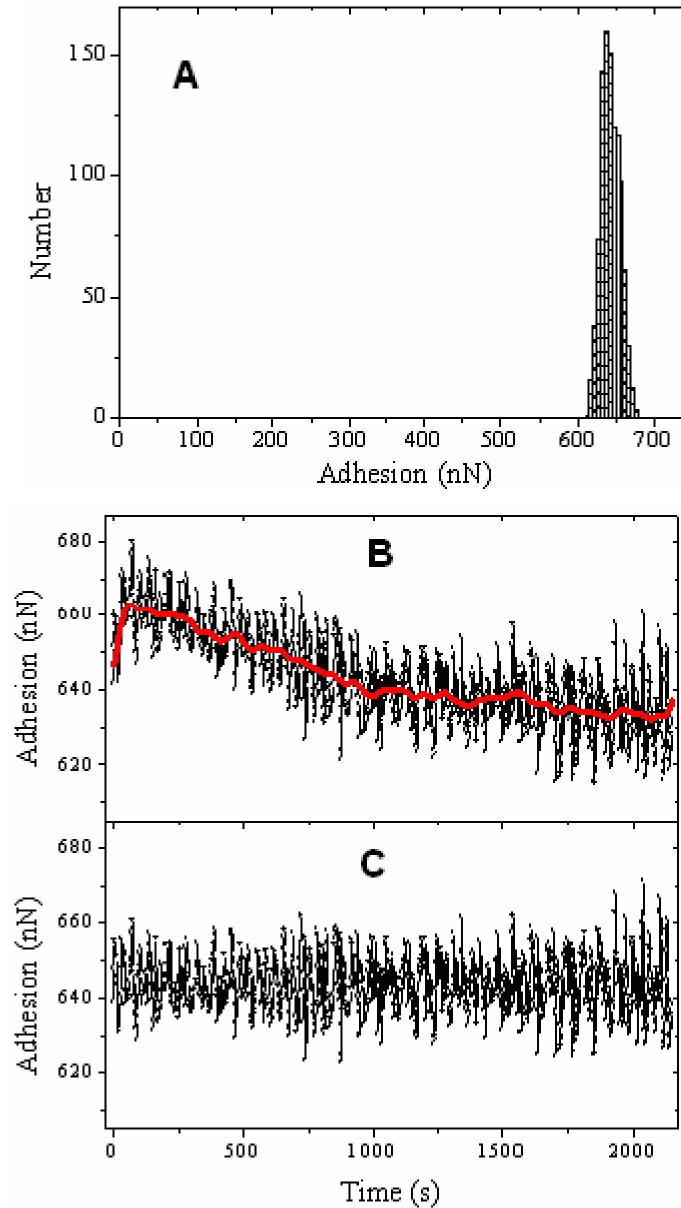

Fig.4.20 (A) Histogram of adhesion forces measured between a glass particle of 4.0 µm diameter and a silicon wafer on an area of 500 × 500 nm at a load of 40nN. (B) Adhesion force measured versus time. The red curve was obtained by a 32 point FFT smoothing of the original curve. (C) Was obtained by subtracting the smoothed curve from the original results and adding the mean adhesion force.

The measurement itself will induce structural changes in the contact region which can change the value for the next adhesion force measurement. Other reason of fluctuations must be within the AFM devices (electronic and optical noise). The error in determining the zero force line contains practically two contributions: A random noise of typically 10-15 pN, which is mainly caused by thermal fluctuations of the cantilever deflection.

Thermal noise of the cantilever using the optical lever detection is $\sqrt{\frac{4k_B T}{3k_c}}$.

Here, k_B and *T* are Boltzmann's constant and temperature. The resulting noise in force is $\sqrt{\frac{4k_B T}{3}}$. Thus, for different types of cantilevers I expect thermal noise of 140 pN (type 1), 30 pN (type 2), 300 pN (type 3), 40 pN (type 4 ad 5), and 100 pN (type 6). This agrees with what I observed. The true error caused by thermal noise is even lower because by fitting a straight line I average over all points. Assuming we have hundred points in the con-contact part of the force curve ad these points are independent, the error is reduced by a factor 10.

The second contribution present in many experiments is a sinusoidal zero force signal rather than a straight line. This is very likely caused by optical interference between light being reflected from the back of the cantilever ad light reflected from the sample surface.

The wavelength of this signal was typically of the order of the wavelength of the light. The amplitude varied strongly between different experiments, a typical value is 10 pN. I take 10-20 pN as an estimate of the error due to determination of the zero force line. The largest error, however, comes from determining the piezo-position of the jump-out point. This is caused by the digitization of the deflection signal. Per retracting force curves 256, 512, or 1024 points are taken. For example, in Fig. 4.21 one data point was taken for each 1 nm change in piezo displacement. This corresponds to a force change of 47 pN. Thus I estimate the total random error in measuring the adhesion force to be 0.05 - 0.1 nN. This corresponds to typically 1%. This is close to the minimal width of the adhesion distribution observed. Therefore I found no indication of an intrinsic statistical process.

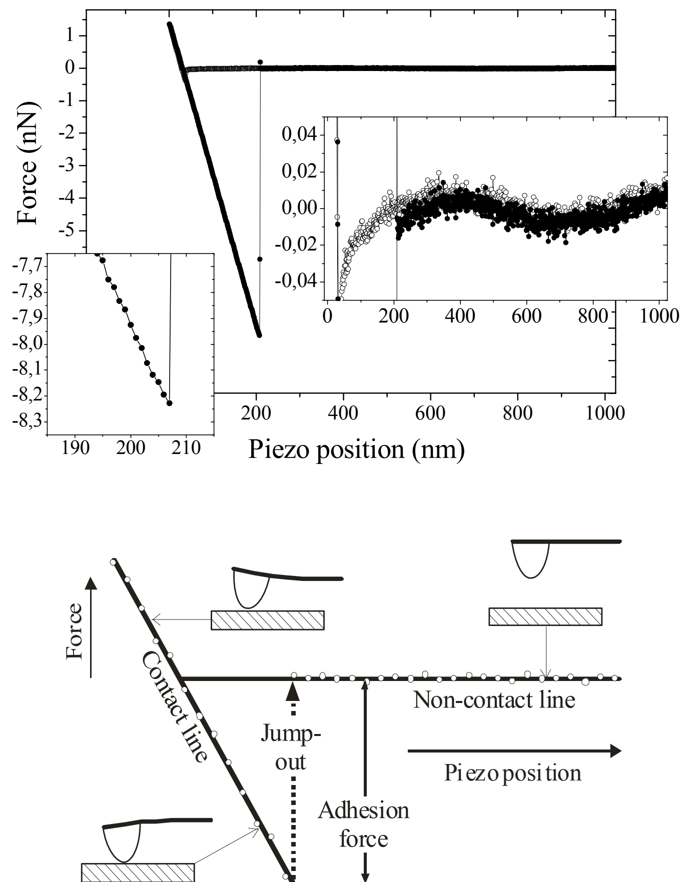

Fig.4.21 Top: Typical force-versus-piezo position curve measured on mica with a silicon nitride tip (type 1). The left bottom inset highlights the point where the tip is released from the surface. The right insert shows the zero-force trace at high force resolution. Down: Schematic force-versus-piezo displacement curve with straight lines fitted to the contact and non-contact parts and the jump-out.

4.4. INFLUENCE OF HUMIDITY ON ADHESION

The influence of relative humidity (RH) on adhesion force is discussed by Harriman and Simkins [185] and Bracken [42, 44, 46, 48, 186-188]. The significance of air humidity in powder processing is stressed by Harnby *et al.* [189]. They comment that small changes in RH can produce a drastic change in powder cohesion, leading to loss of process control in industrial applications. One reason is certainly the meniscus force. Water condenses into the gap at the contact region between hydrophilic particles. This is

described by the Kelvin equation, which relates the relative vapor pressure to the curvature of the condensed liquid surface. The reduced Laplace pressure in the meniscus and surface tension of the liquid cause an attractive force [53]. Capillary force results from condensation of water vapor between the surface and nanoscale AFM tip during contact. When condensation occurs, capillary bridge forms between the tip and surface. Capillary condensation tends to occur on hydrophilic surfaces. The equilibrium radius of the capillary bridge meniscus has long been described by Kelvin equation [51][52]. Several researchers have investigated the influence of humidity on adhesion force with AFM [69, 119, 190-198]. Many experiments showed a significant dependency of the adhesion force on the relative humidity [40, 52, 54, 56, 57, 183]. A continuous increase humidity was, for example, observed for the interaction of a silicon nitride tip with mica [194], between silica particles [199], a silica particle and a silicon wafer [200], or between a silicon nitride tip and molybdenum trioxide [201]. The adhesion force between particles or particle surface by using AFM colloidal probe technique depending on relative humidity [190, 202, 203]. Jones *et al.* study of adhesion between flat surfaces of glass or silicon and silicon AFM tip or glass microspheres [204].

In other case, adhesion force versus humidity curves showed a maximum [42, 58, 205] or a step like increase [69], even on similar surfaces. In cleavage experiments of mica, a decrease in the cleavage force with increasing humidity was observed [70]. Sugawara *et al.* [191] used an AFM to measure the adhesion force between a standard Si_3N_4 probe tip and mica surface for different humidity. The capillary adhesion forces between an AFM tip of a particle and a flat surface was calculated by numerical solution of equations which are developed by an approximate analytical equation which is by Marmur [206], [197].

Next part of my study was influence of humidity on the adhesion force for single nanocontacts.

Adhesion force-versus-humidity curves were measured for several combinations of surfaces and AFM tips. The surfaces were:

1) Freshly cleaved muscovite mica.

2) Silicon wafers cleaned with the RCA method and in this way made hydrophilic (contact angle with water $<5^{\circ}$).

3) Freshly cleaved HOPG, which is hydrophobic and has an advancing contact angle of 80°-87° with water.
4) Cleaned Teflon, which is hydrophobic and has contact angle>90° with water.
5) Iron particles, which were glued to a substrate
As probes silicon nitride tips (type 1), silicon tips (type 2), and silica particles attached to the end of tipless cantilever (type 3) were used. Result of first preliminary experiment showed that the shape of adhesion force-versus-humidity curves often changed from experiment to experiment. Within one experiment adhesion forces changed with time and often different results were obtained when increasing and decreasing humidity (hysteresis). For this reason, I used a special setup, which allowed a fast change of the humidity to minimize time effects and hysteresis. A whole experiment starting at low humidity to high humidity and reducing again to low humidity lasted typically 15 minutes.

4.4.1. Meniscus force on hydrophilic surfaces

To study the influence of humidity on adhesion, I measured adhesion force on clean and freshly cleaved mica, silicon wafers cleaned with RCA method, and in this way, mage hydrophilic that contact angle with water is very small (θ<5°). The adhesion force taken with silicon tip (type 2), silicon nitride tip (type 1), and silica or iron particles attached to the end of tipless cantilever (type 3). In preliminary experiments, I observed that the shape of adhesion force versus humidity curves often changed from experiment to experiment. Within one experiment, adhesion forces changed with time, and often different results were obtained when increasing and decreasing humidity (hysteresis). The adhesion force-versus-humidity curves on silicon wafer surface is as a function of the humidity and noticed that there are three distinct force regimes (Fig.4.22) [42, 207-209]. First, at low humidity ($RH \prec 40\%$) adhesion forces are almost constant. Second, adhesion forces increase with increasing humidity ($40\% \prec RH \prec 70\%$). Third; adhesion forces decrease with increasing humidity ($RH \succ 70\%$).

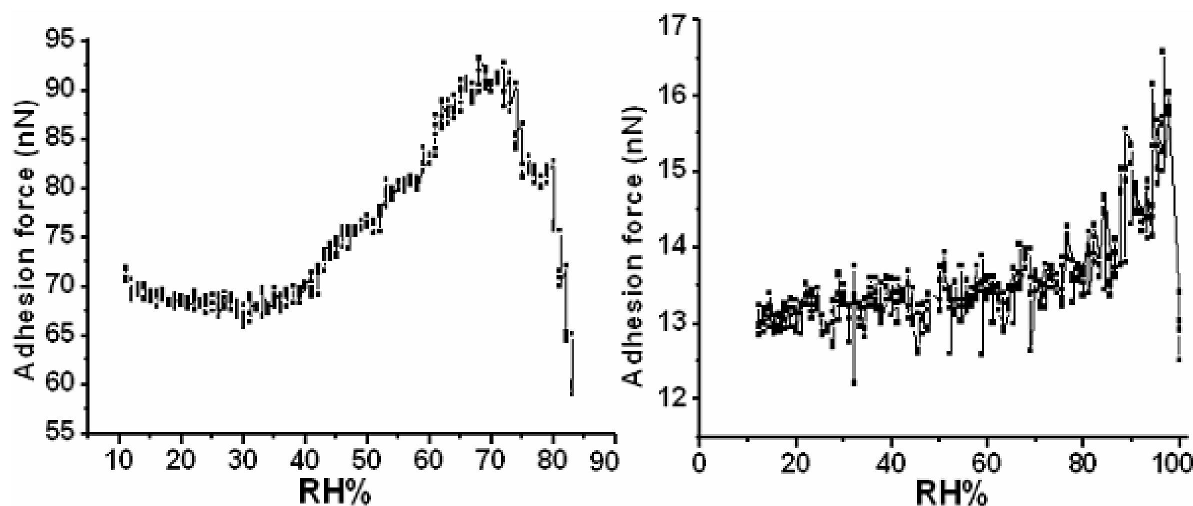

Fig.4.22 Adhesion force versus humidity for two typical measured with silicon nitride tip (cantilever 1) on silicon wafer (left). A silicon tip (cantilever 2) on silicon wafer (right).

The independence of adhesion on humidity at relatively dry conditions can be understood if one assumes that the formation of the capillary neck requires a minimum height of the water film. No capillary neck forms between two surfaces until the water film thickness reaches this minimum thickness. For RH $\leq$ 40% the adhesion force on silicon wafer is restricted to van der Waals interaction between tip and the sample surface. The water film thickness was found to increase with the increase of RH [210], the thickness of the water film on the silicon surface is too thin to form a capillary neck with the probing tip for RH less than 40%. When the water film thickness reaches the minimum thickness requirement at 40% RH; a water bridge forms between the tip and the substrate surfaces, leading to a sudden increase of the meniscus force (Fig.4.23). In the high RH regime ($RH \succ 70\%$) adhesion force decreases with increasing RH for a hydrophilic tip and sample. Mate and Binggeli [119] discussed the decrease as the interplay between capillary forces and the forces related to the chemical bonding between molecules of the liquid in the gap such as water molecules. I divided the force-humidity spectra with hydrophilic interfaces into three regimes; ($RH \prec 40\%$) a van der Waals regime at low RH, in next regime ($40\% \prec RH \prec 70\%$) a capillary force dominated, and at high humidity ($RH \succ 70\%$). To better understand the influence of humidity on adhesion force on freshly cleaved mica, I measured force versus humidity as for the silicon wafer. Results show a maximum in the adhesion force on

mica as a function of relative humidity but not on the silicon waver sample (Fig.4.23). Here, surface energy of sample is important to the nature of the humidity relative. While others have observed a similar transition point (maximum of adhesion) on mica [69, 211]. Thundat *et al*. [194], observed a flat response in force at relative humidity less than 20%, followed by a pronounced increase which did not level off at humidity up to 80%. Salmeron and *et al*. found a virtually flat response in adhesion force on mica at relative humidity less than 20%, an increase near 20%, and a maximum at 25-30%, followed by a gradual decrease and found that the structure and height of the water layer on mica as a function of relative humidity [68].

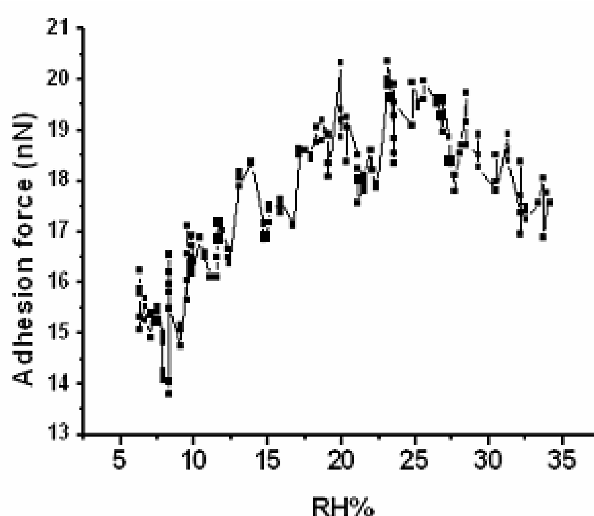

Fig.4.23 Adhesion force versus humidity measured between a fresh mica surface and silicon nitride tip (type 1) when increasing humidity.

Results of some our experiments showed that the maximum point of force move to high humidity with time. If we used the same surface for a second or third measurement the maximum point of force moved to higher humidity. Fig.4.24 shows this phenomenon for a mica surface but this is was also observed on a silicon wafer. Fig.4.24A shows that maximum forces occur at about 30% of humidity but in Fig.4.24.B the maximum was observed at about 70%. This indicates changes within the time span of one hour for the originally freshly cleaved mica surface.

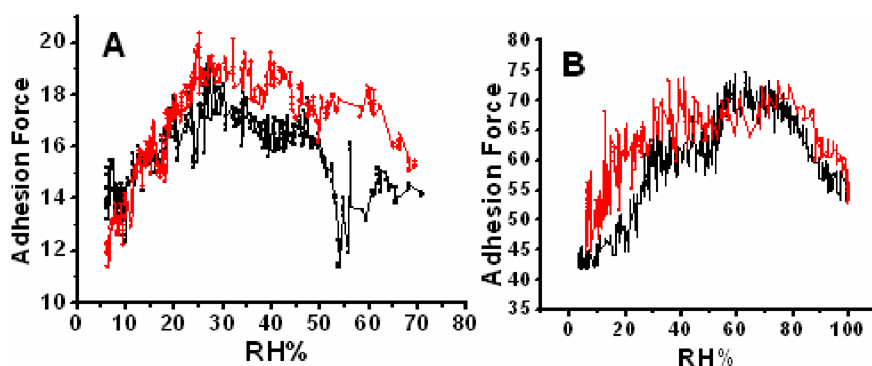

Fig.4.24 Adhesion force versus humidity measured between mica surface and silicon tip (type 2) when increasing and deceasing humidity. A is first and B is second experiment. The maximum force is shifted to higher humidity in second experiment.

I measured adhesion force versus humidity between a silicon wafer cleaned with RCA method and a silica particle with a radius of $R = 2.5$ μm (Fig.4.25). For humidity above 80% adhesion force between silica particle and silicon surface is not stable and showed large fluctuations. For decreasing humidity I had to start the experiment below 70% of humidity.

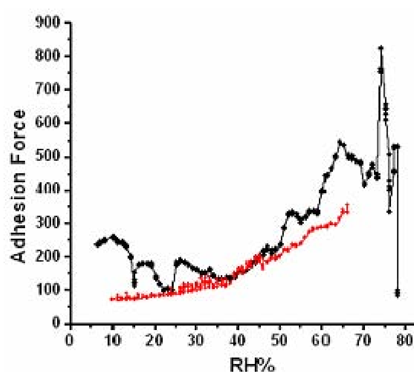

Fig.4.25 Adhesion force versus humidity measured between clean silicon wafer surface and silica particle attached on tipless cantilever (type 3) when increasing (black symbol) and decreasing (red symbol) humidity. Load force was 600nN.

4.4.2. Meniscus force on hydrophobic surface

a) HOPG surface

HOPG is useful in atomic force microscopy measurement because it has hexagonal periodicity which can be used for calibration of the system. In this study, HOPG provides an atomically smooth surface for making force measurements with AFM tips. Following my experiments were influence of humidity on adhesion force on hydrophobic surfaces such as HOPG and

Teflon. No significant dependence of the adhesion force on humidity was observed on HOPG (Fig.4.26). This agrees with previous results, where a significant influence of humidity was observed only for the adhesion between hydrophilic surfaces, while forces on hydrophobic surfaces showed no dependency [42, 58, 190].

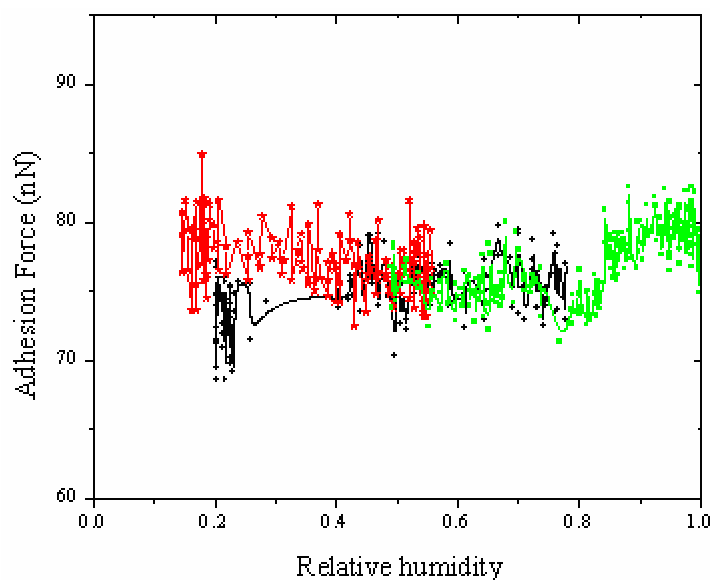

Fig.4.26 Adhesion force-versus-humidity measured with a silicon tip (type 2) on HOPG. Results of three different runs with the same tip are shown.

Influence humidity effect on hydrophilic and hydrophobic surface are different, I show both results in Fig.4.27. The silicon wafer was freshly and cleaned with RCA method.

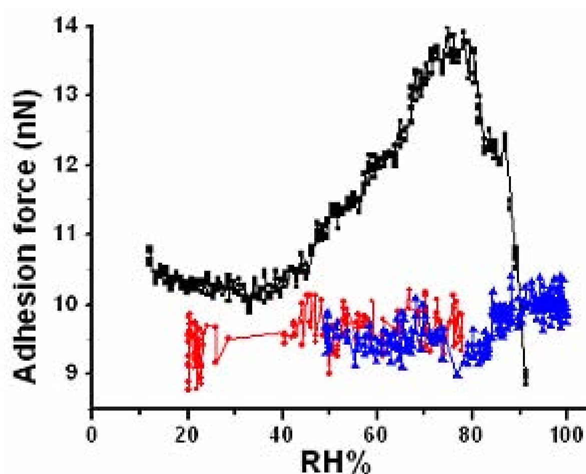

Fig.4.27 Adhesion force versus humidity measured on the freshly cleaved HOPG surface and silicon wafer that was cleaned with RCA method. Black symbols show results measured

when increasing the humidity for the silicon wafer surface. Results for HOPG are marked by red (increasing humidity) and blue symbols for decreasing humidity.

b) Teflon surface

As a second hydrophobic sample, I used Teflon. The Teflon sample was cleaned before measurement with ethanol in an ultrasonic bath for 3 minutes and rinse with pure water 3 times. No significant dependence of the adhesion force on humidity was observed on Teflon (Fig.4.28).

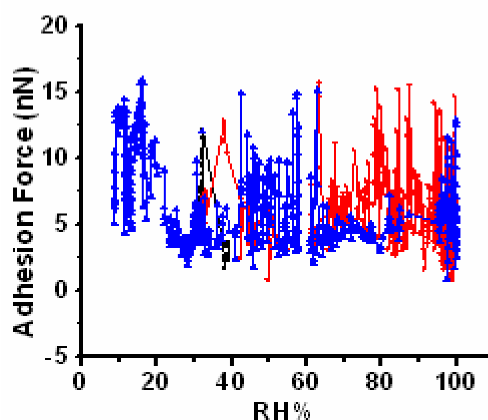

Fig.4.28 Adhesion force-versus-humidity measured with a silicon nitride tip (type 5) on Teflon surface. Results of three different runs with the same tip are shown.

4.5. SIMULATION OF EXPERIMENTAL RESULTS WITH THE TWO-SPHERE-MODEL

The influence of humidity was studied on fresh and clean samples such as hydrophilic and hydrophobic surfaces. Some typical adhesion force versus humidity curves are shown in Fig 4.28. These curves represent three main types observed on hydrophilic surfaces: a maximum at relatively low humidity of 30-50% (Fig 4.28A), a maximum at higher humidity (Fig 4.28B), and a continuous increase (Fig 4.28C). I did not observe systematic differences between results obtained with silicon nitride (type 1) and silicon (type 1) tips. In the following, I attempt to reproduce experimental adhesion force versus humidity curves by model calculation. All types of adhesion force versus humidity curves measured could be reproduced with the two-sphere model within experimental accuracy.

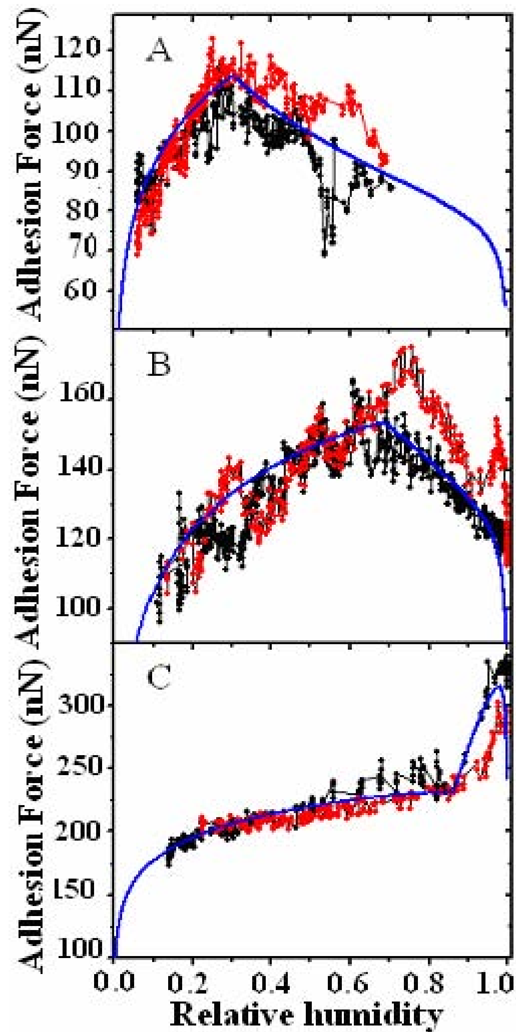

Fig.4.28 Adhesion force versus humidity for three typical cases measured with a silicon tip (type 1) on mica (A), a silicon nitride tip on a silicon wafer (B), and a silicon tip on an iron particle (C) in a nitrogen atmosphere. Black symbols show results measured when increasing the humidity, red symbols represent results obtained when decreasing humidity. The blue lines show the results of calculations with the two-sphere model (section 2.6.4). The parameters were $R_1 = 160nm$, $R_2 = 90nm$, $H = 0.17nm$, $a = 14.5nm$, in A; $R_1 = 190nm$, $R_2 = 150nm$, $H = 0.18nm$, $a = 30nm$ in B; and $R_1 = 260nm$, $R_2 = 400nm$, $H = 0.165$, $a = 56nm$ in C. The contact angle was assumed to be 10°. For the Hamaker constants, I assumed $A_H^g = 6.5 \times 10^{-20}$ J, and $A_H^l = 10^{-20}$ J for silicon nitride interacting with mica (A) and silicon nitride interacting with silicon oxide (B), respectively. In the case of silicon nitride interacting with iron (C) I used higher values of $A_H^g = 20 \times 10^{-20}$ J and $A_H^l = 5 \times 10^{-20}$ J.

The first typical experimental results (Fig. 4.28A) -a maximum at relatively low

humidity- could be simulated with a blunt tip using $R_1 = 160$ nm, $R_2 = 90$ nm, $a = 14.5$ nm, and an asperity, which effectively introduces a minimal spacing of $H = 0.17$ nm. Three features and three parameters (H, R_1, R_2) characterize the adhesion force versus humidity curve at different length scale. For low humidity, the asperity determines the increase because it basically prevents condensation and reduces the meniscus force between the sphere and the plane due to the additional spacing. The spherical shape of object causes the meniscus force to increase. At $\frac{P}{P_0} = 0.302$, the water meniscus has reached a radius of $a = 14.5$nm. From this point on, sphere 2 dominates the adhesion forces. Since R_2 is smaller than R_1, the meniscus forces decreases with increasing humidity, and the curve shows a distinct maximum. Van der Waals forces do not play a significant role, because of the minimal distance caused by the asperity; they are between 14 nN at $\frac{P}{P_0} \to o$ and 3.6 nN at $\frac{P}{P_0} \to 1$.

I would like to point out that the shape of the adhesion force versus humidity curve agrees with the results of a computer simulation of the meniscus force between a hydrophilic planar surface and hydrophilic tip [197]. In Figure 3.31B the experimental results show a maximum around 70% humidity, and the absolute adhesion forces are slightly higher than those in figure 4.28A. To calculate corresponding curves, I chose $R_1 = 190$ nm, and $R_1 = 150$ nm. To shift the maximum to higher humidity, the radius a was increased to $a = 30$ nm. With these parameters, the meniscus force is dominated by sphere 1 up to a humidity of 0.687. At higher humidity, the meniscus extends to sphere 2 ($l \succ a$), and sphere 2 determines the meniscus force. The last typical case is a continuous increase in the adhesion force with increasing humidity (Fig 4.28C). For humidity up to 0.861, the curve is well describe by $R_1 = 260$ nm with an asperity, which prevents the tip from getting closer than $H = 0.165$ nm. At 0.861 humidity, the meniscus reaches an extension of $l = a = 56$ nm. The increase of adhesion is particularly strong at a humidity above 0.861. Such a strong increase can be described by sphere 2 with $R_2 = 400$ nm. In this case, sphere 2 is larger than sphere 1. In the analysis, I used a 5 times

higher Hamaker constant of 5×10^{-20} J in water and 3×10^{-19} J in air to take into account the fact that the Hamaker constant on iron is higher than it is on silicon oxide or mica. Still, only at low humidity the van der Waals force contribute significantly to the total force; it is 72nN for $\frac{P}{P_0} \rightarrow 0$. At high humidity, it decreases to 18nN.

I would like to point out that the theoretical results are only fitted by trial and error. Since the meniscus force versus humidity curve cannot be expressed as an analytical function, a fit with standard programs was not possible. Fitting the experimental adhesion force versus humidity curves with the model of a conical tip with a spherical end was less successful. The curves could not be reproduced with reasonable values for the radius of curvature R and the opening angle φ.

4.6. TIP WEAR

In some experiments show a pronounced hysteresis of adhesion force versus humidity curves was observed (e.g. Fig 4.29). SEM images of tips before and after force measurement indicates that changes in the tip structure can occur when being in contact with another solid surface. This agrees with results reported by various research groups who observed tip wear by SEM [212-216]. Tip wear was studied at different humilities by scanning an area of 5×5 μm^2 for 5, 10, and 30 min on a silicon wafer or mica with different cantilevers (type 2 and 6).

Five tendencies were observed. The first is expected (e.g., ref [214]): tip wear increased with scanning time. Second, tip wear also increased with humidity (Fig.3.30.C and E). This agree with Nakahara *et al.* [217] who observed that wear of $NaNO_3$ in air increased with humidity. Third, on mica I observed significantly less wear than on silicon wafers (Fig.4.30F). This is probably caused by the lower interaction with the inert mica surface. Fourth, silicon tips exhibited stronger wear when scanned on a silicon surface than silicon nitride tips under the same condition. Fifth, tip wear increased with the spring constants used, even at similar loads. I have no explanation for the last effect.

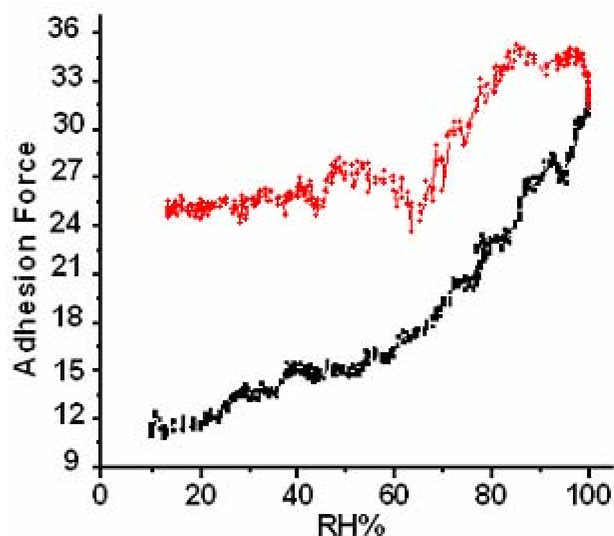

Fig.4.29 Adhesion force versus humidity measured with silicon tip (cantilever No. 2) on silicon wafer surface. Red symbols and black symbols showed increasing and decreasing of humidity. A pronounced hysteresis is observed, indicating structural changes of the AFM tip.

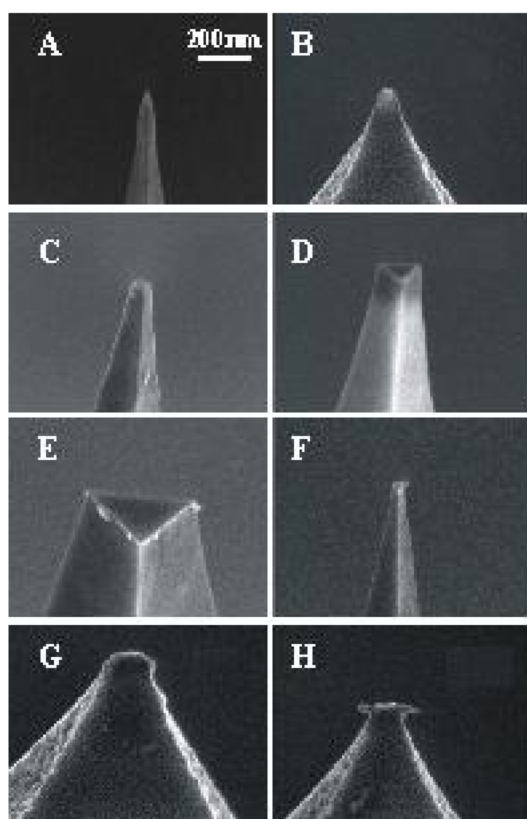

Fig.4.30 Images of AFM tips: (A-B) silicon tip (type 6) and Silicon nitride tip (type 5) before use; (C-E) typical silicon tips (type 6) after scanning an area of (25 µm)2 on a silicon wafer for 30 min at a load 30 nN and 55, 85, and 90% humidity, respectively; (F) silicon tip (type 5) after scanning on mica at 85% humidity for 5 min; (G-H) two typical silicon nitride tips (type 5) after scanning a silicon wafer at 85% humidity.

4.7. CONCLUSIONS

The adhesions of fine particles play a significant role in the performance of particulate processes and in the quality of particulate products. In this investigation first I measured the adhesion force between AFM tips or particles attached to AFM cantilevers and different solid surfaces by FV mode. When measuring the adhesion force-versus-time at the same contact area two kinds of variation were observed: first, random noise and slower fluctuations. Random noise is due to thermal vibrations and noise in the detection system. No intrinsically process is required to explain it. The slower fluctuations are probably caused by plastic deformation and structural changes in the material at the nanocontact. On homogeneous and smooth surfaces such as silicon wafer and mica, distribution of adhesion force measured between nanocontacts can be as narrow 1.1%. We estimated the error of electronic, optical lever deflection and zero force line which has most effect in wide of force distribution and why we can not measured single value of adhesion force.

Roughness and in homogeneity can cause a significant change in the contact area which increase width of adhesion histogram by a factor of two to ten times.

Under ambient conditions, a water meniscus generally forms between a nanoscale atomic force microscope tip and hydrophilic surface. This nanoscale meniscus produces a capillary force between AFM tip and surface. In the second part of this study I investigate influence of humidity on the adhesion force on nanocontacts. Force curves were measured on silicon wafer, mica, HOPG, and Teflon surfaces at humidity levels varying from below 5% RH to 100%. Adhesion force-versus-humidity curves measured between hydrophilic surfaces can be interpreted by assuming capillary condensation of water into the contact region which causes a meniscus force. The result shows that adhesion force as a function of humidity for silicon and mica surfaces against an AFM SiO_2 and Si_3N_4 tips and silica particle depends on tip shape and the hydrophilic property of surfaces. Due to strong capillary condensation, we observed three different regimes of the force-humidity curves: first, van der Waals force at low humidity, second, increasing

adhesion force at intermediate humidity, and third, decreasing adhesion force at high humidity. Maximum of adhesion force of freshly and cleaned silicon wafer is at 70% ~ 90% and on fresh and cleaved mica at 30% ~ 45% RH. Different adhesion behavior and changes depend on the surface termination, thickness of the adsorbed water layer, and on the pressure within the meniscus between AFM tip and sample surface. The adhesion force on hydrophobic surfaces such as HOPG and Teflon did not change whit humidity. We calculated meniscus force between different shape of particles and surfaces using a two sphere model with a single asperity to take surface roughness into account. The model calculation fitted well our experimental results.

The time dependence of the adhesion force and the hysteresis observed in adhesion force-versus-humidity experiments indicates that the structure of the tip changes when being in contact with another solid surface. We observed that tip wear increased with times scanning, humidity, and on mica significantly less than on silicon wafer.

ACKNOWLEDGMENTS

At the end I would like to acknowledge all those people who made the thesis possible.

I wish to express my candid gratitude to Prof. Dr. Hans-Jürgen Butt for his willingness to support and guide my PhD research. In particular, I would like to thank him for the many insightful suggestions and the implicit knowledge which can not be obtained through course work. Furthermore I would like to thank him for the support and help for my family and me to overcome the difficulties in living abroad in the last 4 years.

I would like especially thank Dr. Michael Kappl for many helpful discussions regarding my research and writing some of the code used for analyzing the data.

I would also like to thank Dr. K. H. Graf and Dr. E. Bonancorso, and Dr. L. O. Heim for many helpful discussions and their friendship in the last 4 years.

I would also like to thank Gunnar Glasser and Maren Müller for taking SEM images of my samples.

I am grateful for the friendly atmosphere and good feeling of the group in both Siegen and the MPIP; I should especially thank Dr. S. Rathgeber, Dr. R. Berger, Dr. K. Büscher, Dr. M. Wolkenhauer, Dr. G. Gillies, Rüdiger Stark, Uwe Rietzler, Andreas Best, Ann-Katrin Awizio, Regina de Hoogh, Annelie Schäfer, Brigitte Niesenhaus, Hanne Christian, Peter Rickert, and all other members of the AK-Butt group.

I express my gratitude to the DFG (Deutsche Forschungsgemeinschaft), which supported this study.

I would also like to thank Dr. D. Habibi, Dr. M. Gholami, Dr. N. Shams, and Dr. Danesh that helped me to come to Germany and all other family friends in Siegen and Giessen.

Finally, I would like to thank all of my family for their support during this study. In particular I would like to acknowledge my wife for her support and encouragement. She has taken on tremendous sacrifices and I will always be indebted to her for the unwearyingly commitment to our relationship through these difficult times.

This thesis is dedicated to my family (my parents, my wife and my children) in partial compensation for taking so much of my time away from them.

تمامی این کوشش ها را

به والدین عزیزم

همسر صبور، مهربان و همراهم

و فرزندان فداکارم

تقدیم می کنم هر چند سختی دوری طولانی روحی و جسمی ما را هیچگاه جبران نمی کند.

Nomenclature

a	contact radius (m)
A	area (m^2)
A_H	Hamaker constant (J)
A_H^g	Hamaker constant of gas-solid
A_H^l	Hamaker constant of liquid-solid
C	speed of light in vacuum (2.998×10^8 m/s)
d_a	distance between asperities
D	distance; tip–sample distance (m)
e	unit charge (1.602×10^{-19} C)
E	Young's modulus (Pa)
F	force (N)
F_{ad}	adhesion force (N)
F_{cap}	capillary force (N)
F_{Disj}	disjoining force
F_M	meniscus force
F_S	surface force
F_{vdW}	van der Waals force
h	Planck's constant (6.626×10^{-34} J s)
H	height of tip (m); distance of closest approach; height of the asperity
k_B	Boltzmann constant (1.381×10^{-23} J/K)
k_c	spring constant of cantilever (N/m)
k_{LS}	spring constant of large-scale cantilever
k_{Test}	spring constant of AFM cantilever
l	radial distance of the liquid meniscus
L	length of cantilever (m)

m_c	mass of the cantilever (g)
m_e	effective mass of the cantilever (g)
n_i	refractive index
P	pressure (N/m^2)
Q_f	quality factor of fundamental mode of the cantilever in fluid
r	distance between molecules (1-1); tip radius or radius of microsphere (m)
r_c	capillary radius
R	particle radius
R_e	Reynolds number
R_G	gas constant
t_c	thickness of the cantilever (m)
T	temperature (K)
U_s	surface energy
V_m	molar volume of a liquid
W	width of cantilevers (m)
$W_{Mol/Plane}$	interaction between molecule and infinite planar surface
W	work of adhesion at contact per unit area (J/m^2); potential energy between two molecules
W_{ad}	work of adhesion at contact (J)
X	distance in gap between two planar,
X	horizontal coordinate originating at the base of the cantilever (m)
z	coordinate normal to a surface (m)
Z	cantilever deflection (m) at a certain horizontal coordinate
$\hat{z}^2$	represents the mean square deflection of the cantilever

Greek letters

α	maximum angle between tip and rough surface;
β	position of the contact line of the liquid on the sphere
γ	half opening angle
Θ	contact angle of the liquid on the sphere and plane
θ	contact angle of the liquid on surface

Nomenclature

λ	Maugis parameter
φ	half opening angle
ε_0	dielectric constant of vacuum; vacuum permittivity
ε_i	dielectric constant of different medium
$\varepsilon(iv)$	value of ε at imaginary frequencies
σ	deformation of particle
σ_0	adhesion stress
δ_{LS}	displacement of large-scale cantilever
δ_{Test}	deflection of AFM cantilever
ρ	particle density
ρ_c	density of the cantilever
ρ_f	density of the fluid
ν	Poisson ratio
γ	surface tension
γ_{sv}	solid-vapor interfacial tensions
γ_{sl}	solid-liquid interfacial tensions
ω_{vac}	vacuum resonant frequency of the cantilever
ω_f	resonant frequency in fluid
η	viscosity of the surrounding fluid
Γ	hydrodynamic function
Γ_f	real components of the hydrodynamic function
Γ_i	imaginary components of the hydrodynamic function

Reference:

(1) Richard, P.; Nicodemi, M.; Delannay, R.; Ribiere, P.; Bideau, D. *Natu. Mater.* **2005,** 4, 121.
(2) Batra, A. P., S.; Khilar, K. C. *AIChE* **2001,** 47, (11), 2557-2565.
(3) Arulanandan, K. L., P.; Krone, R. B. *J. Geotechnol. Eng. Div. Am. Soc. Eng,* **1975,** 101, (1), 51-56.
(4) Venkitaraman, A. R., P. M.; Sharma, M. M. *SPE* **1995**, 27388.
(5) Lopez Trosell, A. I. **2005**.
(6) Hertz, H. *J. Reine Angewandte Mathematik* **1882,** 92, 156-171.
(7) Johnson, K. L.; Kendall, K.; Roberts, A. D. *Proc. Roy. Soc. London A* **1971,** 324, 301-313.
(8) Derjaguin, B. V. M., V.M.; Toporov, Yu. P. *J. Colloid Interface. Sci.* **1975,** 53, 314-325.
(9) Müller, V. M.; Yushchenko, V. S.; Derjaguin, B. V. *j. Colloid and interface Sci.* **1980,** 77, 91-101.
(10) Müller, V. M.; Derjaguin, B. V.; Toporov, Y. P. *Colloids Surf.* **1983,** 7, 251-259.
(11) Derjaguin, B. V.; Muller, V. M.; Toporov, Y. P. *J. Colloid Interf. Sci.* **1975,** 53, 314-325.
(12) Maugis, D. *J. Colloid Interf. Sci.* **1992,** 150, 243-269.
(13) Carpick, R. W.; Ogletree, D. F.; Salmeron, M. *J. Colloid Interface Sci.* **1999,** 211, 395-400.
(14) Johnson, K. L. G., J. A. *J. Colloids interface. Sci.* **1997,** 192, 326.
(15) Larsen, R. I. *Am. Ind. Hyg. Assoc. J.* **1958,** 19, 265-270.
(16) Podczeck, F.; Newton, J. M. *J. Pharm. Sci.* **1995,** 84, 1067-1071.
(17) Polke, R. K., H.; Rumpf, H., Einflüsse auf die Adhäsion von Feststoffteilchen. In *Chemie, physikalische Chemie und Anwendungstechnik der grenzflächenaktiven Stoffe*, ed.; 1973; 'Vol.
(18) Newton, J. M.; Lam, K. K. *Powder Technol* **1992,** 73, 267.
(19) Podczeck, F.; Newton, J. M.; James, M. B. *Powder Technol.* **1995,** 83, 201-209.
(20) Rennie, P. R.; Chen, X. D.; Mackereth, A. R. *Powder Technol* **1998,** 97, 191.
(21) Binnig, G.; Quate, C. F.; Gerber, C. *Phys. Rev. Lett.* **1986,** 56, 930-933.
(22) Heim, L. O.; Blum, J.; Preuss, M.; Butt, H.-J. *Phys. Rev. Lett.* **1999,** 83, 3328-3331.
(23) Drelich, J. T., G. W.; Beach, E. R. *J. colloid and interface Sci.* **2004,** 280, 484-479.
(24) Tormoen, G. E.; Drelich, J. *J. of Adhesion Science and technology* **2005,** 19, (3-5), 181-198.
(25) Cassie, A. B. D. *Discuss. Faraday Soc.* **1948,** 3, 11-16.
(26) Drelich, J. *Colloids Surf. A* **1996,** 116, 43-54.
(27) Krupp, H.; Schnabel, W.; Walter, G. *J. Colloid Interf. Sci.* **1972,** 39, 421-423.
(28) Schubert, H.; Sommer, H.; Rumpf, H. *Chem.-Ing.-Techol.* **1976,** 48, (6), 716.
(29) Polke, R. *Bull. Soc. Special Chim. France* **1969,** A3241, 51-54.

(30) Heim, L. O.; Blum, J.; Preuss, M.; Butt, H. J. *Powder Technol* **2002,** 83, 201-209.
(31) Rumpf, H. *Chemie-Ing.-Techn.* **1974,** 46, (1), 1-11.
(32) Götzinger, M.; Peukert, W. *Langmuir* **2004,** 20, 5298-5303.
(33) Cooper, K.; Gupta, A.; Beaudoin, S. *J. Colloid Interf. Sci.* **2001,** 234, 284-292.
(34) Rabinovich, Y. I.; Adler, J. J.; Ata, A.; Moudgil, B. M. *J. Colloid Interf. Sci.* **2000,** 232, 17-24.
(35) Rabinovich, Y. I. A., J. J.; Ata, A.; Moudgil, B. M. *J. Colloid Interface Sci.* **2000,** 232, (10-16), 10-17.
(36) Peukert, W.; Mehler, C.; Götzinger, M. *Appl. Sci* **2002,** 196, 30-40.
(37) Li, Y. Q.; Tao, N. J.; Pan, J.; Garcia, A. A.; Lindsay, S. M. *Langmuir* **1993,** 9, 637-641.
(38) Ata, A.; Rbinovich, Y. I.; Singh, R. K. *J.Adhesion Sci. Technol* **2002,** 16, (4), 337-346.
(39) Bocquet, L. C., E.; Ciliberto, S.; Crassous, J. *J.Nature* **1998,** 396, (24/31), 735-737.
(40) Rabinovich, Y. I.; Adler, J. J.; Esayanur, M. S.; Ata, A.; Singh, R. K.; Moudgil, B. M. *Adv. Colloid interface Sci.* **2002,** 96, 213-230.
(41) Sirghi, L.; Nakagiri, N.; Sugisaki, K.; Sugimura, H.; Takei, T. *Langmuri* **2000,** 16, 7796-7800.
(42) He, M.; Blum, A. S.; Aston, D. E.; Buenviaje, C.; Overney, R. M. *J. Chem. Phys.* **2001,** 114, (3), 1355-1360.
(43) Cappella, B.; Dietler, G. *Surf. Sci. Rep.* **1999,** 34, 1-104.
(44) Corn, M., Adhesion of particles. In *Aerosol Sci.*, ed.; Academic Press: New York, 1966; 'Vol. 359-392.
(45) Hermann, W.; Poleke, R. *Chem.-Ing.-Tech* **1971,** 43, 764-768.
(46) Schubert, H. *Chem.-Ing.-Tech.* **1973,** 45, (6), 396-401.
(47) Podczeck, F.; Newton, J. M.; James, M. B. *J. Colloid Interf. Sci.* **1997,** 187, 484-491.
(48) Cleaver, J. A. S. T., J. W. G. *J. KONA.* **2004,** 22, 9-22.
(49) Schaefer, D. M. C., M.; Reifenberger, R.; Demejo, L. P.; Rimai, D. S. *J. Adhes. Sci. Technol.* **1994,** 8, 197- 210.
(50) Biggs, S. S., G. *J. Adhesion Sci. Technology* **1998,** 12, 461-478.
(51) Israelachvili, J. **1991**.
(52) Fisher, L. R.; Israelachivili, J. N. *J. Colloids and Surface* **1981,** 3, 303-319.
(53) Derjaguin, B. *Kolloid Zeitschrift* **1934,** 69, 155-164.
(54) Christenson, H. K.; Claesson, P. M. *Science* **1988,** 235, (390-392).
(55) Ando, Y.; Ino, J. *Wear* **1998,** 216, 115-122.
(56) Bhushan, B.; Dandavate, C. *J. Appl. Phys.* **2000,** 87, 1201-1210.
(57) Yoon, E. S.; Yang, S. H.; Han, H. G.; Kong, H. *Wear* **2003,** 254, 974-980.
(58) Xiao, X.; Qian, L. *Langmuir* **2000,** 16, 8153-8158.
(59) Berger, C. E. H. v. d. W., K. O., Kooyman, R. P. H., de Grooth, B. G., Greve, J. *Langmuir* **1995,** 11, 4188-4196.
(60) Rozhok, S. S., P.; Piner, R.; Lieberman, M.; Mirkin, C. A. *J. Phys. Chem. B* **2004,** 108, 7814-7819.
(61) Coelho, M. C.; Harnby, N. *Powder Technol* **1978,** 20, 197-200.

(62) Thundat, T.; Sales, B. C.; Chakoumakos, B. C.; Boatner, L. A.; Allison, D. P.; Warmack, R. J. *J. Surface Science Letters* **1993,** 293, L863-L869.
(63) Fuji, M.; Machida, K.; Takei, T.; Watanabe, T.; Chikazawa, M. *J.Pjysi Chem. B* **1998,** 102, 8782-8787.
(64) Biggs, S.; Cain, R. G.; Dagastine, R. R.; Page, N. W. *J.Adhesion Sci. Technol* **2002,** 16, 869.
(65) Gulbinski, W.; Pailharey, D.; Suszko, T.; Mathey, Y. *Surf. Sci.* **2001,** 475, 149-158.
(66) Price, R.; Young, P. M.; Edge, S.; Stanifort, J. N. *J. Pharm.* **2002,** 246, 47-59.
(67) Farshchi Tabrizi, M.; Kappl, M.; Cheng, Y.; Gutmann, J.; Butt, H. J. *Langmuir* **2006,** 22, 2171-2184.
(68) Xu, L. L.; A; Hu, J.; Ogletree, D. F.; Salmeron, M. *J. Phys. Chem. B* **1998,** 102, 540-548.
(69) Sedin, D. L.; Rowlen, K. L. *Anal. Chem.* **2000,** 72, 2183-2189.
(70) Wan, K. T. L., B. R. *J. Acta. Metall. Mater.* **1990,** 38, (11), 2073-2083.
(71) Bergström, L. *Adv. Colloid Interface Sci.* **1997,** 70, 125-169.
(72) Landau, L. D.; Lifshitz, E. M. **1984.**
(73) Hunter, R. J. **2001**.
(74) Israelachvili, J. N., *Intermolecular and Surface Forces*. 2 ed.; Academic Press: London, 1992; 'Vol.' p.
(75) Butt, H.-J.; Graf, K. K., M., *Physics and Chemistry of Interfaces*. ed.; Wiley-VCH: Berlin, 2003; 'Vol.' p 361.
(76) Larson, I.; Drummond, C. J.; Chan, D. Y. C.; Grieser, F. *J. Am. Chem. Soc.* **1993,** 115, 11885-11890.
(77) Ishino, T. H., H.; Tanaka, K.; Gemma, N. *J. Appl. Phys.* **1994,** 33, 4718-4722.
(78) Drummond, C. J.; Senden, T. J. *Colloids Surf. A* **1994,** 87, 217-234.
(79) Maugis, D. *J. Colloid Interface Sci.* **1992,** 150, 243-269.
(80) Abdel-Aal, H. A. *Wear* **2003,** 255, 348-364.
(81) Quintanilla, M. A. S.; Castellanos, A.; Valverde, J. M. *Phys. Rev.* **2001**, E 6403.
(82) Christenson, H. K. *J. Phys. Chem.* **1986,** 90, 4-6.
(83) Parker, J. L.; Claesson, P. M.; Attard, P. *J. Phys. Chem.* **1994,** 98, 8468-8480.
(84) Fuller, K. N. G.; Tabor, D. *Proc. Roy. Soc. London A* **1975,** 345, 327-342.
(85) Rumpf, H., *Particle Technology*. ed.; Chapman and Hall: London, 1990; 'Vol.' p.
(86) Butt, H. J.; Cappella, B.; Kappl, M. *J. Surface Science Report* **2005,** 59, 1-152.
(87) Greenwood, J. A.; Tripp, J. H. *J. of Applied Mechanics ASME* **1967,** 34, (259), 153-159.
(88) schwarz, U. S.; Safran, S. A.; Komura, S. *Mater. Res. Soc. Symp. Proc.* **2001,** 651, T5.3.1-T5.3.6.
(89) Cheng, W.; Dunn, P. F.; Brach, R. M. *Journal of adhesion* **2003,** 79, 749-776.
(90) Zhou, H. B.; Gotzinger, M.; Peukert, W. *J. Powder Techbology* **2003,** 135, 2635.
(91) Kendall, K.; Alford, N. M.; Birchall, J. D. *Nature* **1987,** 325, 794-796.

(92) Cahn, J. M.; Hilliard, J. E. *J. chem. Phys.* **1958,** 28, 258-266.
(93) Young, T. *phil.Trans.* **1805**, (95), 56-78.
(94) de Laplace, P. S. *Suppl. au X. Livre* **1805**.
(95) Kwok, Y.; Neumann, A. W. *J. Colloids inter. Sci.* **1999,** 81, 167-249.
(96) Zisman, W. A. *Advances chemistry* **1964,** 43.
(97) Fowkes, F. M. *Ind. Eng. Chem.* **1964,** 12, 40.
(98) Driedger, O.; Neumann, A. W.; Sell, P. J. *Kolloid-Z.Z.Polym* **1965,** 201, 52.
(99) Van Oss, C. J. C., M.K.; Good, R.J. *Chem. Rev.* **1988,** 88, 927-941.
(100) Derjaguin, B. V.; Müller, V. M.; Toporov, Y. P. *J. Colloids inter. Sci.* **1980,** 73, 293.
(101) Muller, V. M.; Yushchenko, V. S.; Derjaguin, B. V. *J. Colloid Interface Sci.* **1983,** 92, 92-101.
(102) Fogden, A.; White, L. R. *J. Colloid and interface Sci.* **1990,** 138, 414.
(103) Pashley, R. M.; McGuiggan, P. M.; Horn, R. G.; Ninham, B. W. *J. Colloids inter. Sci.* **1988,** 126, 569.
(104) Claesson, P. M.; Blom, C. E.; Herder, P. C.; Ninham, B. W. *J. Colloid Interf. Sci.* **1986,** 114, (1), 234-242.
(105) Pashley, P. M.; McGuiggan, P. M.; Pashley, R. M. *J. Colloid and interface Sci.* **1987,** 27, 1088.
(106) Pashley, R. M.; McGuiggan, P. M.; Ninham, B. W.; Evans, D. F. *Science* **1985,** 229, 1088-1089.
(107) Hamaker, H. C. *Physica* **1937,** 4, 1058.
(108) Israelachvili, J. N.; Tabor, D. *Proc. Roy. Soc. London A* **1972,** 331, 19-38.
(109) Van Giessen, A. E.; Bukman, D. J.; Widom, B. *J. Colloid and interface Sci.* **1997,** 192, 257.
(110) Grundke, K.; Bogumil, T.; Gietzelt, T.; Jacobasch, H.-J.; Kwok, D. Y.; Neumann, A. W. *J.Colloid Polym. Sci* **1996,** 101, 58.
(111) Preuss, M.; Butt, H.-J. *J. Colloid and Interface Sci.* **1998,** 208, 468-477.
(112) Bartell, F. E.; Jennings, H. Y. *J. Phys. Chem.* **1934,** 38, 495.
(113) Bruil, H. G.; van Aartsen, J. *Colloid Polym. Sci.* **1974,** 252, 3238.
(114) Siebold, A.; Walliser, A.; Nardin, M.; Oppliger, M.; Schultz, J. *J. Colloid Interf. Sci.* **1997,** 186, 60-70.
(115) Varadaraj, R.; Bock, J.; Brons, N.; Zushma, S. *J.Colloid Polym. Sci* **1994,** 167, 207.
(116) Tiberg, F., Cazabat, A. M. *Langmuir* **1994,** 10, 2301-2310.
(117) Brzoka, J. B. **1993**.
(118) Gao, C.; Dai, P.; Homola, A.; Weiss, J. *Journal of tribology* **1998,** 120, 358-368.
(119) Binggeli, M.; Mate, C. M. *J. Appl. Phys. Lett* **1994,** 65, (4), 415-417.
(120) Fisher, R. A. **1926**, 493-505.
(121) Christenson, H. K. *J. Physical Rev. Lett.* **1994,** 26, 1921-1925.
(122) Christenson, H. K. *Chem. Phys. Lett.* **1985,** 118, 455-458.
(123) Crossous, J.; Chaelaix, E.; Loubet, J.-L. *J. Physical Rev. Lett.* **1997,** 78, (12), 2425-2428.
(124) Weisenhorn, A. L.; Hansma, P. K.; Albrecht, T. R.; Quate, C. F. *Appl. Phys. Lett.* **1989,** 54, 2651-2653.
(125) Ljunggren, S.; Eriksson, J. C. *Colloids Surf. A* **1997,** 129-130, 151-155.
(126) Kohonen, M.; Christenson, H. K. *Langmuir* **2000,** 16, 7285-7288.

(127) bocquet, L.; Charlaix, E.; Cilliberto, S.; Crassous, J. *J: Nature* **1998,** 396, (24/31), 735-737.
(128) Riedo, E.; Levy, F.; Brune, H. *Phys. Rev. Lett.* **2002,** 88, 185505.
(129) Binder, K. *Ann. Rev. Phys. Chem.* **1992,** 43, 33-59.
(130) Mehrotra, V. P.; Sastry, V. S. *Powder Technology* **1980,** 25, 203-214.
(131) Tselishchev, Y. G.; Val'tsifer, V. A. *Colloidal Journal* **2003,** 65, (3), 385-389.
(132) Hains, W. B. J. *J. Agric. Sci* **1925,** 15, 529-543.
(133) Iinoya, K.; Asakawa, S.; Hotta, K.; Burson, J. H. *J. Powder Technology* **1967,** 1, 28-32.
(134) Melrose, J. C.; Wallick, G. C. *J.Phys. Chem.* **1967,** 71, (1), 3676-3678.
(135) Clark, W. C.; Haynes, J. M.; Mason, G. *Chen. Eng. Sci.* **1968,** 23, 810-812.
(136) Heady, R. B.; Cahn, J. M. *Met. Trans.*
1970, 1, 185-189.
(137) Orr, F. M.; Scriven, L. E.; Rivas, A. P. *J. Fluid Mech* **1975,** 67, (4), 723-742.
(138) Hotta, K.; Takeda, K.; Iinoya, K. *Powder Technology* **1974,** 10, 231-242.
(139) Lian, G.; Thornaton, C.; Adams, M. J. *Colloid and Interface Sci.* **1993,** 161, 138-147.
(140) Melrose, J. C. *Am. Inst. Chem. Eng.* **1966,** 12, 986-994.
(141) Princen, H. M. *J. Colloid and interface Sci.* **1968,** 26, 249-253.
(142) De Bisschop, F. R. E.; Rigole, W. J. L. *J. colloid and Interface Sci.* **1982,** 88, (1).
(143) Pietsch, W.; Rumpf, H. *Chemie-Ing.-Techn.* **1967,** 39, 885-893.
(144) Smolej, V.; Pejovnik, S. *Z. Metallkde* **1976,** 67, 603-605.
(145) Cross, N. L.; Picknett, R. G. **1963**, 383-390.
(146) Schiller, P.; Wahab, M.; Mögel, H. *Langmuir* **2004,** 20, 2227-2232.
(147) Wan, K.-T.; Smith, D. T.; Lawn, B. R. *J. Am. Cream. Soc* **1992,** 75, (3), 667-676.
(148) Tselishchev, Y. G.; Val'tsifer, V. A. *Colloid J.* **2003,** 65, (3), 385-389.
(149) Curry, J. E.; Christenson, H. K. *Langmuir* **1996,** 12, 5729-5735.
(150) Binnig, G.; Rohrer, H.; Gerber, C.; Weibel, E. *Phys. Rev. Lett.* **1982,** 49, (1), 57-61.
(151) Binnig, G.; Rohrer, H.; Gerber, C.; Weibel, E. *Phys. Rev. Lett.* **1983,** 50, 120-123.
(152) Claesson, P. M.; Ederth, T.; Bergeron, V.; Rutland, M. W. *Adv. Colloid Interf. Sci* **1996,** 67, 119-183.
(153) Kappl, M.; Butt, H.-J. *Part. Part. Syst. Charact.* **2002,** 19, 129-143.
(154) Parsegian, V. A.; Rand, R. P.; Fuller, N. L.; Rau, D. C. *Methods of Enzymology* **1986,** 127, 400-416.
(155) Grandbois, M., Dettmann, W., Benoit, M., Gaub, H. E. *The Jornal of Histochemistry & Cytochemistry* **2000,** 48, (5), 719-724.
(156) Heinz, W. F.; Hoh, J. H. *Nanotechnology* **1999,** 17, 143-150.
(157) McKendry, R., M.-E. Theoclitou, T. Rayment, C. Abell. *Nature* **1988,** 391, 566-568.
(158) A-Hassan, E., Heinz, W. F., Antonik, M. D., D'Costa, N: P., Nageswaran, S., Schoenenberger, C-A., hoh, J. H. *Biophysical Journal* **1998,** 74, 1564-1578.

(159) Khan, A.; Philip, J.; Hess, P. *J. Appl. Phys.* **2004,** 95, (4), 1667-1672.
(160) Albrecht, T. R.; Akamine, S.; Carver, T. E.; Quate, C. F. *J. Vac. Sci. Technol. A* **1990,** 8, (4), 3386-3390.
(161) Butt, H.-J.; Siedle, P.; Seifert, K.; Fendler, K.; Seeger, T.; Bamberg, E.; Weisenhorn, A. L.; Goldie, K.; Engel, A. *J. Microscopy* **1993,** 169, 75-84.
(162) Neumeister, J. M.; Ducker, W. A. *Rev. Sci. Instrum.* **1994,** 65, 2527-2531.
(163) Stock, F. **1989**.
(164) Sader, J. E.; White, L. *J. Appl. Phys.* **1993,** 74, (1), 1-9.
(165) Timoshenko, S. **1932**, 245-259.
(166) Butt, H.-J.; Jaschke, M. *Nanotechnology* **1995,** 6, 1-7.
(167) Torii, A.; Sasaki, M.; Hane, K.; Shigeru, O. *Meas. Sci. Technol.* **1996,** 7, 179-184.
(168) Shimada, Y.; Yonezada, Y.; Hsunada, H.; Nonaka, R.; Katuoa, K.; Morishita, H. *J. KONA.*
2002, 20, 223-230.
(169) Newton, J. M. L., K. K. *J. Powder Technology.* **1992,** 73, 267.
(170) Newton, J. M.; Lam, K. K. *J. Powder Technology* **1992,** 73, 117-125.
(171) Podczeck, F.; Newton, J. M.; James, M. B. *J.Adhesion Sci. Technolgy* **1994,** 8, 1459-1472.
(172) Podczeck, F. N., J.M.; James, M.B. *J. Powder Technology* **1995,** 83, 201-209.
(173) Newton, J. M.; Lam, K. K. *J. Powder Technology* **1993,** 76, 149-154.
(174) Ducker, W. A.; Senden, T. J.; Pashley, R. M. *Nature* **1991,** 353, 239-241.
(175) Butt, H.-J. *J. Colloid Interf. Sci.* **1994,** 166, 109-117.
(176) Sun, G.; Butt, H.-J. *Macromolecules* **2004,** 37, 6086-6089.
(177) GUISEPPI-Elie. *ABTECH Scientific, Inc.* **1996**, 1-5.
(178) Kern, W. **1993**.
(179) Heyns, M. M. B., T; Cornrlissen, I.; De Gendt, S.; Degraeve, R.; Groeseneken,G.; Kenens, C.; Knotter, D. M. *IBM research* **1999,** 43, (3), 339-350.
(180) Kern, W. P., D. *Solid state technology* **1970,** 31, 187.
(181) Baum, T.; Schiffrin, D. J. *J.Micromach. Microeng.* **1997,** 7, 338-342.
(182) Tormoen, G. W.; Drelich, J. *J. Adhesion Sci. Technol.* **2005,** 19, (3-5), 215-234.
(183) Ando, Y. *Wear* **2000,** 238, 12-19.
(184) Eaton, P. J., Graham, P., Smith, J. R., Smart, J. D., Nevell, T. G., Tsibouklis, J. *Langmuir* **2000,** 16, 7887-7890.
(185) Harriman, L., Simkins, D. *Chem. Engng.* **1997**, 80-87.
(186) Brachken, E. *Sensor Rev.* **1997,** 17, (4), 283-290.
(187) Hermann, W.; Poleke, R. *Chem.-Ing.-Technology* **1971,** 43, 764-768.
(188) Podczeck, F.; Newton, J. M.; James, M. B. *J. Colloid and Interface Sci.* **1997,** 187, 484-491.
(189) Harnby, N., Hawkins, A. E., Opalinski, I. *Chem. Engng. Res.* **1996,** 74, (A6), 605-615.
(190) Fuji, M. M., K.; Takei, T.; Watanabe, T.; Chikazawa, M. *Langmuir* **1999,** 15, 4584-4589.
(191) Sugawara, Y.; Ohta, M.; Konishi, T.; Morita, S.; Suzuki, M.; Enomoto, Y. *Wear* **1993,** 168, 13-16.

(192) Eastman, T.; Zhu, D.-M. *Langmuir* **1996,** 12, 2859-2862.
(193) Thundat, T.; Warmack, R. J.; Chen, G. Y.; Allison, D. P. *Appl. Phys. Lett.* **1994,** 64, 2894-2896.
(194) Thundat, T.; Zheng, G. Y.; Chen, G. Y.; Warmack, R. J. *J. Surface Science Letters* **1993,** 294, L939-L943.
(195) Fujihira, M. A., D.; Okabe, Y.; Takano, H.; Hokari, H.; Frommer, J.; Nagatani, Y.; Sakai, F. *Chem.Lett.* **1996,** 7, 499-500.
(196) Piner, R. M., C.A. *Langmuir* **1997,** 13, 6864-6868.
(197) Jang, J.; Schatz, G. C.; Ratner, M. A. *j. chem. Phys.* **2004,** 120, (3), 1157-1160.
(198) Garcia, R.; Calleja, M. *Journal of Appl. Phys.* **1999,** 86, (4), 1898-1903.
(199) Fuji, M.; Machida, K.; Takei, T.; Watanabe, T.; Chikazawa, M. *J.Phys. Chem. B* **1998,** 102, 8782-8787.
(200) Biggs, S.; Cain, R. G.; Dagastine, R. R.; Page, N. W. *J.Adhesion Sci. Technol* **2002,** 16, 869.
(201) Gulbinski, W.; Pailharey, D.; Suszko, T.; Mathey, Y. *Surf. Sci.* **2001,** 475, 149-158.
(202) Price, R.; Young, P. M.; Edge, S.; Stanifort, J. N. *J. Pharm.* **2002,** 246, 47-59.
(203) Tangg, J. W., C.; Liu, M.; Su, M.; Bai, C. *Chinese Sci. Bull* **2001,** 46, (11), 912-914.
(204) Jones, R. P., H. U.; Cleaver, J. A. S. *Langmuir* **2002,** 18, 8045-8055.
(205) Xu, L.; Lio, A.; Hu, J.; Ogletree, D. F.; Salmeron, M. *J.Phys. Chem. B* **1998,** 102, 540-548.
(206) Marmur, A. **1993**.
(207) Hu, J.; Xiao, X. D.; Salmeron, M. *Appl. Phys. Lett.* **1995,** 67, 476-478.
(208) Thundat, T.; Zheng, X. Y.; Chen, G. Y.; Warmack, R. J. *Surf. Sci.* **1993,** 294, L939-L943.
(209) Yang, G. L. V., J. P.;Bustamante, C. J. *J. Scanning* **1996,** 18, 344.
(210) Ata, A.; Rabinovich, Y. I.; Singh, R. K. *J.Adhesion Sci. Technol* **2002,** 16, (4), 337-346.
(211) Beaglehole, D.; Wilson, P. *J. Phys. Chem.* **1994,** 98, 8096-8100.
(212) Khurshudov, A. G.; Kato, K.; Koide, H. *J.Tribiology Leterrs* **1996,** 2, 345-354.
(213) Lantz, M. A.; O'Shea, S. J.; Welland, M. E. *Rev. Sci. Instrum.* **1998,** 69, (4), 1757-1764.
(214) Bloo, M. H.; Haitjema, H.; Pril, W. O. *J. Measurment* **1999,** 25, 203-211.
(215) Prioli, R.; Regada, D. C.; Freire, F. L. *J.Appl. Phys.* **2000,** 87, (3), 1118-1122.
(216) Chung, K. H.; Lee, Y. H.; Kim, D. E. *Ultramicroscopy* **2005,** 102, 161-171.
(217) Nakahara, S.; Langford, S. C.; Dickinson, J. T. *J. Tribology Letters* **1995,** 1, 277-300.